EVALUATION OF NICKEL FOR USE AS AN INTERCONNECT IN SOLID OXIDE FUEL CELLS

by

Richard Wesley Jackson III

BS, University of Pittsburgh, 2004

Submitted to the Graduate Faculty of
School of Engineering in partial fulfillment
of the requirements for the degree of
Master of Science

University of Pittsburgh

2007

UNIVERSITY OF PITTSBURGH

SCHOOL OF ENGINEERING

This thesis was presented

by

Richard Wesley Jackson

It was defended on

May 18, 2007

and approved by

N. G. Eror, Professor Emeritus, Mechanical Engineering and Materials Science Department

J. P. Leonard, Assistant Professor, Mechanical Engineering and Materials Science Department

Thesis Advisor: F.S. Pettit, Professor Emeritus, Mechanical Engineering and Materials Science Department

Thesis Advisor: G. H. Meier, Professor, Mechanical Engineering and Materials Science Department

EVALUATION OF NICKEL FOR USE AS AN INTERCONNECT IN SOLID OXIDE FUEL CELLS

Richard Wesley Jackson III, MS

University of Pittsburgh, 2007

Solid oxide fuel cells are devices that have the potential to efficiently produce electricity while creating little pollution. The development of a suitable interconnect is one of the primary technological hurdles that is holding back their commercial viability. An interconnect has two primary functions in a planar solid oxide fuel cell stack. First, the interconnect must separate the anode gas of one cell from the cathode gas of the adjacent cell and second, the interconnect must provide an electrical connection between adjoining cells. During operation, the ability of the interconnect to perform both of these functions can be compromised.

An interconnect is simultaneously exposed to an anode gas of hydrogen, or hydrogen-hydrocarbon mixtures, and a cathode gas of air. Degradation can occur as a result of this dual atmospheric exposure because both hydrogen and oxygen can dissolve in high concentrations making the interconnect susceptible to a phenomenon known as chemically driven cavity growth (CDCG) which can compromise the mechanical properties of the interconnect. Nickel, silver and nickel-silver composites were studied under dual atmospheric conditions for times up to 600 hours in order to study their mechanical stability. The microstructural evolution was studied using SEM, and a model was developed to predict under what conditions CDCG would occur and what the rate of degradation would be.

The electrical properties of pure nickel, a Ni-5wt%Cu alloy, and both Ni, and Ni-5Cu coated with CeO_2 were measured using a direct current four-point probe. These tests, in conjunction with thermogravimetric analysis, were used to determine the rate of degradation with time. The best electrical properties were observed in the CeO_2 coated nickel system.

In addition, a simple theoretical model which describes the electrical degradation of nickel as a function of time was developed and showed good agreement with the experimental results. This model could be used to estimate how the electrical properties of new candidate interconnect materials will degrade during fuel cell operation.

TABLE OF CONTENTS

LIST OF TABLES

LIST OF FIGURES

PREFACE

This work would not have been possible without the assistance of a number of individuals. First, and foremost I would to thank my advisors Prof. Meier and Prof. Pettit for their guidance and advice throughout my project. Working with them has been inspiring and I am privileged to have studied under them.

I also want to thank members of the Materials Science and Engineering department, particularly my committee members, Profs. Leonard and Eror. I have learned a great deal from them in the class room and the laboratory and am grateful for their contributions. I also want to thank Al Stewart for his technical assistance patience and knowledge and the graduate students who I have worked with, particularly; Matt Stiger, Scot Laney, Kee Young Jung, and Andreas Kulovits. Their assistance with experiments and the many discussions I have had with them were invaluable.

Finally I would like to thank my family; my parents and my sister Nancy for the constant support and encouragement, and my wife Erika. She has been my colleague, editor, and best friend and I am thankful for everything she has done for me.

This research was made possible by support for the United States Department of Energy through the SECA program

1.0 INTRODUCTION

Fuel cells are devices that generate electrical energy from the chemical energy of reaction between a fuel and an oxidant. This is an attractive function because energy can be produced efficiently while producing little pollution. The concept of producing electricity from a chemical reaction was first developed in 1839 by William Grove[1]. Since then, NASA has put these ideas to use in the 1960's in the Apollo program and more recently in the space shuttles and other niche uses have been developed, but widespread use of fuel cells has never occurred.

Over the years, many different types of fuel cells have been developed, but this work will focus on solid oxide fuel cells (SOFCs). As their name implies, these cells use solid oxide electrolytes which allows operation at high temperatures, typically between 600-1000°C. The elevated operating temperature produces rapid reaction kinetics and as result, a wide range of fuels can be used. This is the most noteworthy advantage that SOFCs have over other fuel cells.

While the elevated operating temperature allows a wider variety of fuel choices, it also creates a demanding environment for the cell components. The primary obstacle in the commercialization of SOFC's is the development of adequate materials.

The interconnect, or current collector is a cell component that must fulfill stringent requirements in an aggressive environment. The role of the interconnect is to provide an electrical connection between adjacent cells while separating the anode and cathode gases. In this configuration, the interconnect is simultaneously exposed to a fuel composed of hydrogen, and possibly hydrocarbon from the anode gas and oxidizing conditions from the cathode gas, while at elevated temperatures. Under these conditions, the interconnect must maintain electrical conductivity, provide mechanical strength, and maintain compliance while thermally cycled. In addition, the interconnect must be easily fabricated and inexpensive, in order to make the cell commercially viable.

Metals are the class of materials that should fulfill these requirements. However, in the presence of an oxidizing gas such as air, most metals oxidize. If the corrosion product does not adhere to the alloy separating the alloy and the gas phase, then the reaction can proceed rapidly. Under these conditions rapid material loss can occur, and the interconnect will not have long term mechanical durability. On the other hand, when the oxide is adherent, the electrical resistance that the interconnect will introduce into the fuel cell circuit can be very high due to the high resistivity of oxide scales. The electrical resistance is proportional to the thickness and electrical resistivity of the oxide scale, and electrical properties of the interconnect can be optimized by minimizing the product of the scale thickness and resistivity.

Figure 1 plots the oxide growth rates and electrical resistivities of oxides that grow by outward diffusion at high temperatures. In the absence of microstructural effects, the growth rate of the oxide is proportional to the point defect concentration. These defects are compensated by electronic defects so that charge neutrality can be maintained. The concentration of electronic defects controls electrical transport through the semiconducting oxides and, as a result, the electronic resistivity of an oxide will increase as scale growth rate decreases. This relationship makes it difficult for an alloy to produce an oxide scale that will not introduce a large resistance into the fuel cell circuit.

Alloys that form alumina and silica scales are used in many high temperature power generation applications due to their slow growth rates. However, these scales have very high electrical resistivities. CoO, and FeO, oxides that grow on cobalt and iron at high temperatures have very low resistivies but grow so fast the product of scale thickness and resistivity is not much lower than slower growing scales. In addition, these oxides grow so rapidly that durability of an iron or cobalt interconnect would be unacceptable due to the rate at which metal would be consumed. The oxides whose properties are a compromise between high resistivity and rapid growth rates are Cr_2O_3, and NiO.

To date, chromia forming ferritic stainless steels have received most of the attention as candidate interconnect materials. Certain ferritic alloys have been found to fulfill many of the requirements placed on the interconnect due to their low cost and good electrical properties. However, the chromia scales formed on these alloys are known to release volatile oxides in the form of CrO_3 and in the presence of water vapor $CrO_2(OH)_2$, at SOFC's operating temperatures. These vapor species have been found to react with other components in the cell and decreasing efficiency. Steps have been taken to limit emission of these oxides from the chromia scales, but no robust solution has been developed.

In light of the above considerations, NiO forming alloys were studied. These materials avoid the contamination problem associated with chromia, while balancing the pitfalls of poor electrical properties displayed by slower growing oxides such as alumina, and the poor mechanical properties associated with rapidly oxidizing materials like iron or cobalt.

Finally, silver-nickel composites will be studied with the goal of circumventing the resistivity of oxide scales altogether. Precious metals such as silver, gold, palladium, and platinum do not form oxides at high temperature, and therefore would display good electrical properties in an SOFC environment. However, these materials are much too expensive for commercial use. A silver-nickel composite was developed in which only a small amount of silver could be used to create a high conductivity pathway through the interconnect, while minimizing the total cost.

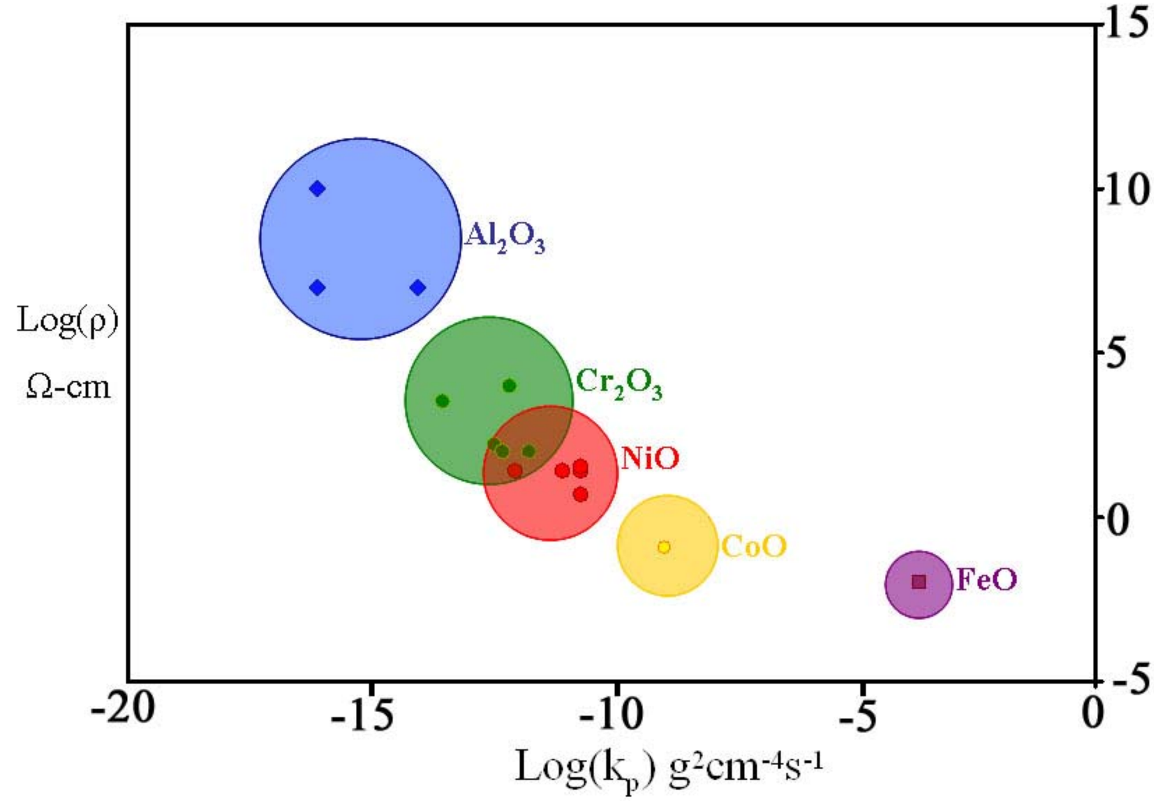

Figure 1. Plot of the resistivity of bulk oxides versus the growth rate of oxide scales at 800°C

2.0 BACKGROUND

2.1 GENERAL MATERIALS DESCRIPTION

2.1.1 Nickel

Nickel is a face centered cubic metal with good ductility and toughness. Commercially pure nickel is commonly used in applications where low temperature corrosion resistance is required. Table 1 lists some relevant properties of nickel.[2-4]

Table 1. Physical Properties of Nickel

Property		Units
Melting Point	1455	°C
CTE at 800°C	17.7×10^{-6}	K^{-1}
Density	8.93	g/cm^3
Yield Stress at 800°C	55	MPa

2.1.2 Nickel Alloys

Nickel alloys are more widely used then pure nickel. The alloy systems that are most popular are Ni-Cu alloys, such as Monels, used for low temperature corrosion resistance, Ni-Cr alloys such as Inconel used for high temperature oxidation resistance, and nickel based superalloys used in applications where strength at high temperatures is required.[3] Nickel and copper form a complete range of solid solutions and the nickel copper phase diagram is shown in Figure 2.

Unlike copper, silver and nickel are nearly immiscible in the solid and liquid state. The Ni-Ag phase diagram is shown in Figure 3. These metals behave more like a composite then an alloy when joined together.

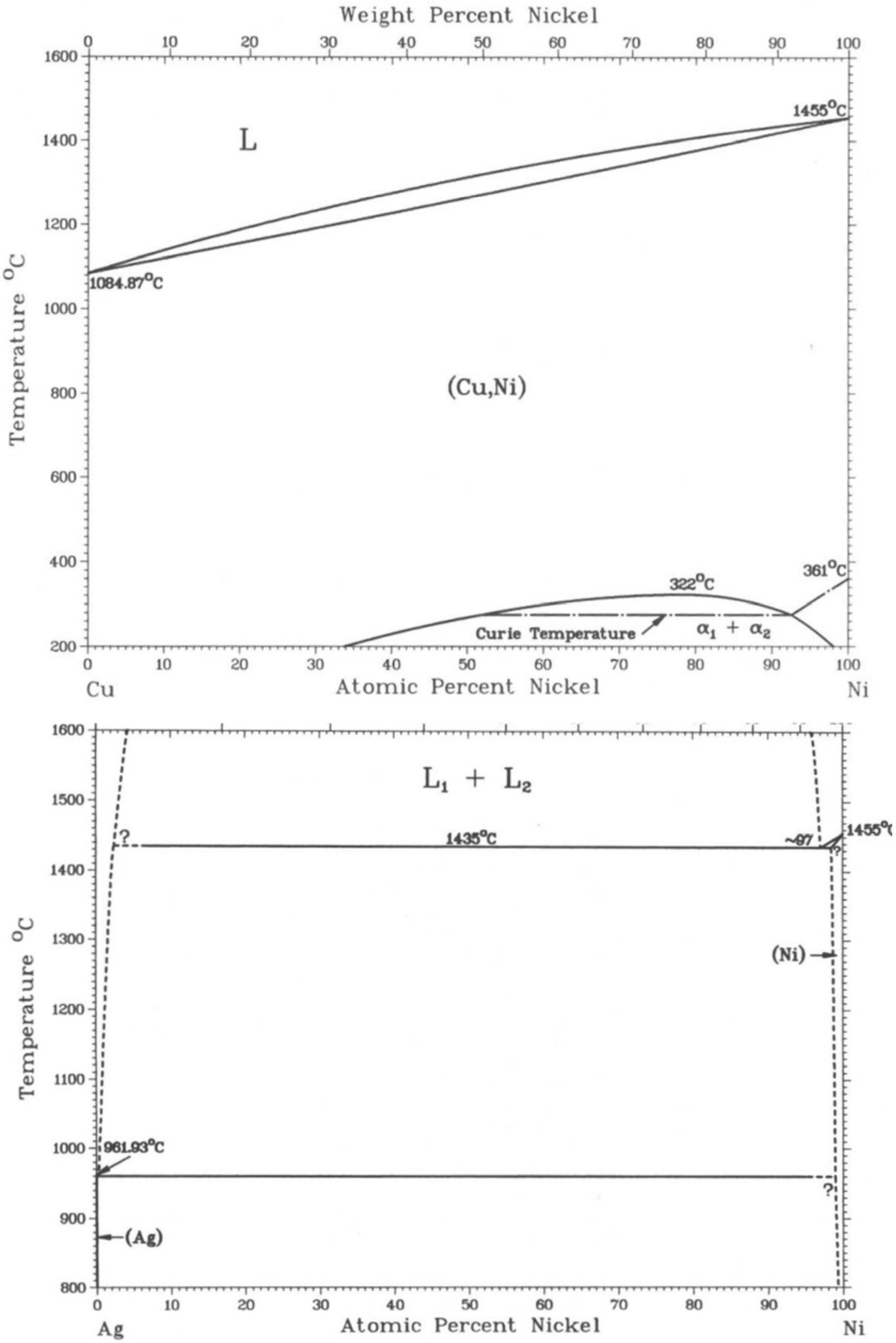

Figure 2. (a) Ni-Cu phase diagram (b) Ni-Ag phase diagram[5]

2.1.3 Silver

This study has focused on limiting the resistive degradation that results from the oxidation of a metallic interconnect. This process can be avoided by using an interconnect composed of a metal that does not oxidize in a fuel cell environment. The only metals that fall into this category are platinum, gold, palladium, and silver. These metals are expensive with respect to the metals typically used in engineering applications. The least expensive of these is silver, which makes it the most realistic choice.

Silver has a low melting point 961°C, therefore, the operating temperature of a fuel cell is between 75-85% of the melting point. As a result, silver is susceptible to creep, and further mechanical degradation can result from the dissolution of gaseous species. In addition, silver will volatilize at a significant partial pressure which can result in substantial material loss during long exposures. However, these drawbacks should not exclude silver from use as an interconnect.

Singh et al.[6,7] have investigated silver under a simulated fuel cell environment. In their investigation, two parallel silver tubes were exposed in a reaction chamber to air, simulating the cathode gas. The inside of one of the tubes was exposed to the same environment and the other was exposed to a simulated anode gas of hydrogen 3% water vapor. The tubes were held at 700°C for 24 hours. The tube which was exposed to air on both sides did not show any substantial degradation. On the other hand the tube exposed to the dual environment underwent mechanical failure resulting from extensive porosity. The proposed cause of the porosity was the nucleation and growth of water vapor bubbles. Oxygen dissolved into silver on the outside of the tube from the cathode gas and hydrogen dissolved into the inner wall of the tube from the anode gas. The concentration of each of these species was great enough to nucleate water vapor bubbles in the silver tube.

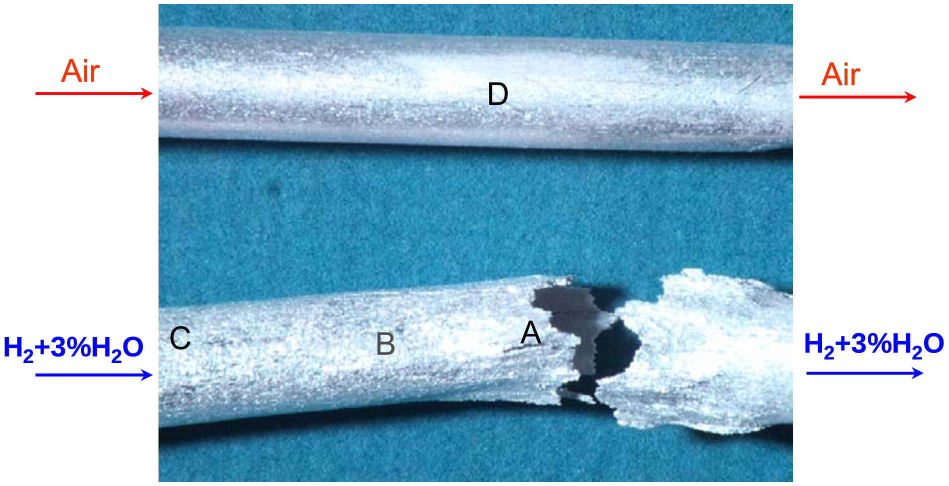

Figure 3. Tubular dual atmospheric test. (Top) Ag tube exposed to air on the inside and outside (Bottom) Ag tube exposed to air on the outside and H_2-3%H_2O on the inside.[6]

Alternative interconnect geometries have been developed to create high electrical conductivity pathways using silver while minimizing the amount of silver needed, reducing the cost, and alleviating some of the mechanical problems of silver. Meulenberg et al.[8] investigated a Fecralloy alloy with silver pegs extending through the length of the metal. No dual atmospheric exposures were performed. Other investigators have examined silver cermets. Neither of these design alternatives can prevent continuous pores from being developed through silver that would result from water vapor bubble nucleation.

2.2 OXIDATION THEORY

2.2.1 Thermodynamics

When evaluating how a material will behave in an environment, it is important to understand which chemical reactions are possible. This evaluation can be made using the second law of thermodynamics. Under conditions of constant temperature and pressure, it is most convenient to use the Gibbs free energy of the system *G’ (J)*,

$$G' = H' - TS' \quad (1)$$

where *H’,(J)* is the enthalpy of the system, *T (K)* is the absolute temperature and *S’(J/K)* is the entropy of the system. At constant temperature and pressure, changes in the Gibbs free energy can be divided into three categories.

$$\Delta G' < 0 \text{ spontaneous reaction expected}$$

$$\Delta G' = 0 \text{ equilibrium}$$

$$\Delta G' > 0 \text{ thermodynamically impossible process}$$

For a generic chemical reaction,

$$aA + bB = cC + dD \quad (2)$$

the change in the Gibbs free energy ΔG*’* can be expressed

$$\Delta G' = \Delta G^{\circ} + RT \ln\left(\frac{a_C^c a_D^d}{a_A^a a_B^b}\right) (3)$$

where a is the activity and ΔG° is the change in Gibbs free energy when all of the components are in their standard states. Further, the activity is defined as

$$a_i = \frac{p_i}{p_i^{\circ}} \ (4)$$

where p_i is the vapor pressure of a substance *i* and p_i° is the vapor pressure of a pure component *i*.

In the case of metals (M) in environments containing oxygen (O), the general chemical reaction can be written,

$$xM + \tfrac{y}{2} O_2 = M_x O_y \,(5)$$

where x and y are stoichiometric coefficients.

The change in Gibbs free energy for this reaction can be written

$$\Delta G' = \Delta G^\circ + RT \ln\left(\frac{a_{M_x O_y}}{a_M^x \, p_{O2}^{y/2}} \right)(6).$$

This expression can be used to determine if a metal will oxidize at a given temperature and oxygen partial pressure. In addition, the oxygen pressure at which the metal and oxide are in equilibrium can be determined by letting $\Delta G'$=0 and rearranging the expression.

$$p_{O_2}^{M/M_x O_y} = \left(\frac{a_{M_x O_y}}{a_m^x} \right)^{2/y} \exp\left(\frac{2\Delta G^\circ}{yRT} \right) \;(7)$$

In the case of the oxidation of nickel,

$$Ni + \tfrac{1}{2} O_2 = NiO \,(8)$$

the Gibbs' free energy of formation for the reactions is given

$$\Delta G^\circ = RT \ln\left(\frac{a_{NiO}}{a_{Ni} \, p_{O_2}^{1/2}} \right)(9)$$

and the dissociation oxygen pressure is expressed as equation (10) when Ni, and NiO are at unit activity.

$$p_{O_2}^{Ni/NiO} = \exp\left(\frac{\Delta G^\circ}{2RT} \right)(10)$$

Plots of standard free energy of formation versus temperature, Figure 4, commonly known as Ellingham diagrams are convenient tools for the comparison of the relative stabilities of oxides. These diagrams are particularly useful in determining which oxide is the most stable when an alloy is exposed to a particular environment.

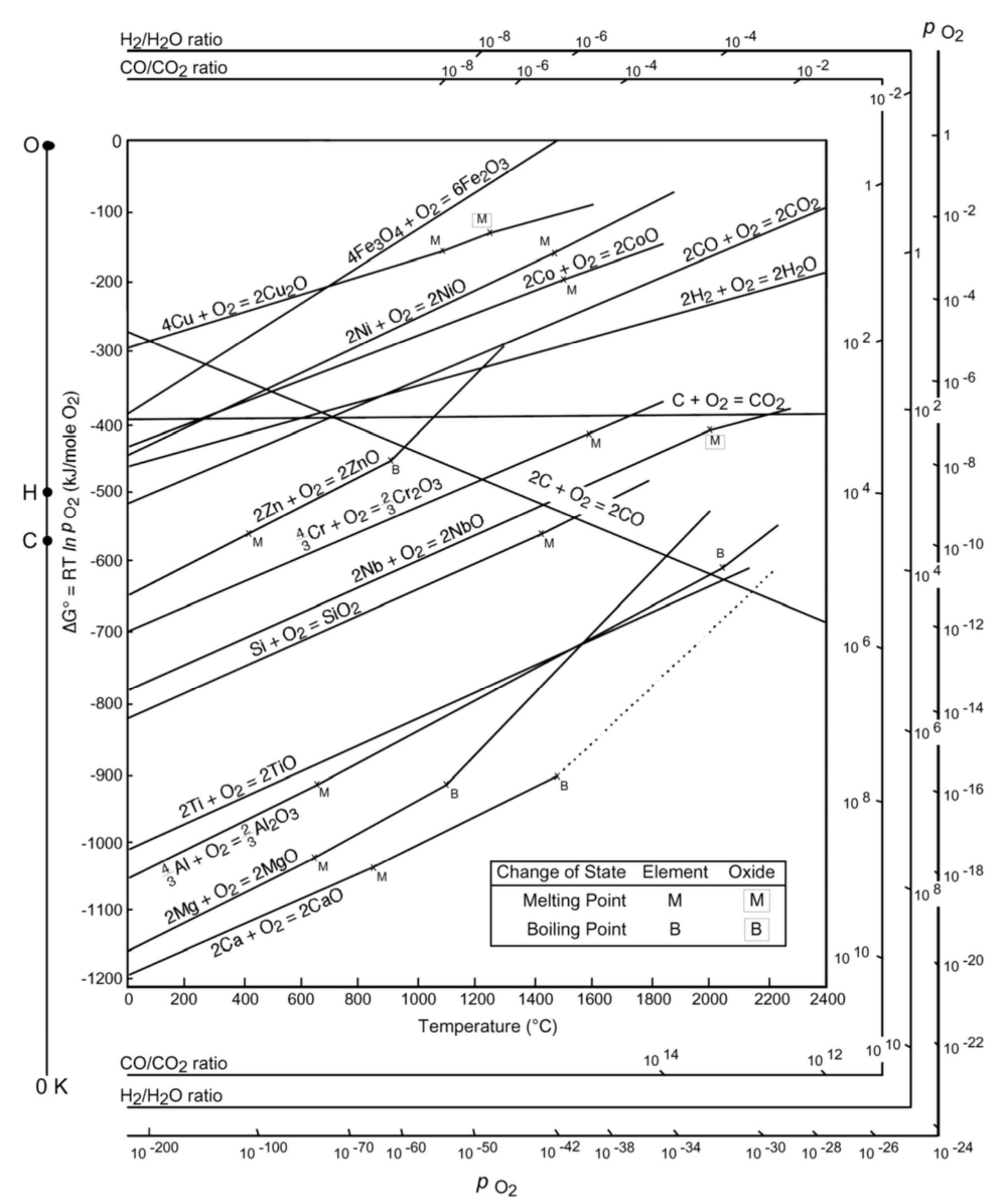

Figure 4. Ellingham diagram for oxides[9]

2.2.2 Reaction Product

Upon exposure to an oxidizing gas, the free surface of a metal or alloy will react to form an oxidation product M_xO_y, under the thermodynamic requirements stated above. This reaction product can be gaseous; as in the case of CO_2, PtO, or CrO_3, liquid; as in the case of V_2O_5, but is most commonly solid, as is in the case of NiO, FeO, Al_2O_3 or TiO_2. In a SOFC, it is desired that the rate of reaction between the gas and the metal be minimized. This is generally achieved by the creation of a reaction product that will separate the two reactants: oxygen and metal. If such a layer is formed, the rate of reaction is usually determined by the rate of transport through the scale[9].

In most high temperature applications where loss of mechanical properties constitutes failure, the desire to decrease the rate of oxidation stems from the need to minimize metal loss during exposure. To this end, the composition of materials must be tailored to produce slowly growing scales that remain adherent, limiting reaction during the life of the material. In the case of the interconnect in the SOFC, mechanical stability is required, however, failure will occur due to the degradation of electrical properties associated with highly resistive oxide scales before their mechanical stability will be compromised.

The bulk of solid reaction products are ionic crystalline oxides. Most ceramic materials crystallize into structures in which oxygen forms a closed packed lattice with cations sitting in interstitial sites in the lattice. An important structure is rocksalt, a face centered cubic close packed anion sub-lattice with cations sitting in octahedral intersitices, Figure. 5. Examples of this structure are NaCl, NiO, and CoO.

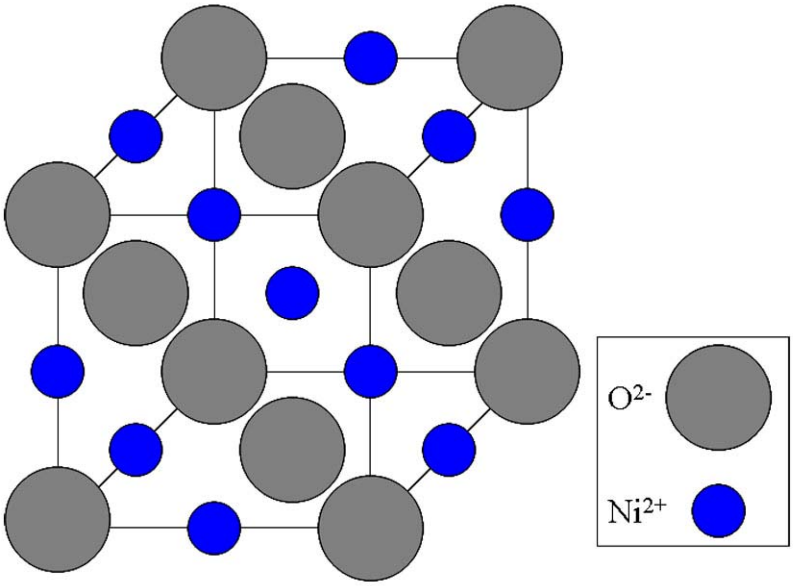

Figure 5. NiO crystal structure

.

2.2.3 Defects

All materials, including ceramics contain deviations from the perfect lattice described above. Many properties of ceramics such as electrical conductivity and diffusivity are greatly influenced by the defect structure of a compound[10]. It is important to understand the nature of the defects that occur in a given material and how the concentration of defects will be affected by the environment.

Defects can be subcategorized by their dimensionality with point defects being zero dimensional, dislocations one dimensional, and grain boundaries, interphase interfaces and surfaces being two dimensional. All of these defects can be important under given circumstances, but point defects can create the greatest changes in diffusional and conduction properties.

Unlike metals, defects in ionic crystals can be electrically charged. Deviations from the perfect lattice, such as vacancies, substitutional solutes and interstitials are known as ionic defects. Deviations from the electronic ground state are electronic defects in which electrons are excited into higher energy states. These electrons can be in the conduction band of the crystal. Electrical neutrality is required and therefore charged defects either ionic or electronic must be compensated by oppositely charged defects.

Kroger[11] developed a nomenclature to describe ionic defects.

M_M - M atom on M site
X_X - X atom on X site
M_i - M atom on interstitial site
X_i - X atom on interstitial site
N_M - impurity N on M site
V_M - vacancy on M site
V_X - vacancy on X site
V_i - vacant interstitial site
e' - electron in conduction band
$h^{\cdot}$ - electron hole in valence band

In this notation, the capital letter represents the species, the subscript describes the site at which the species is located and the superscript describes the charge on the species with respect to the host species where $(^{\cdot})$ refers to a net positive charge and $(')$ refers to a net negative charge and $(^{x})$ refers to no net charge difference.

In oxide crystals, many different types of defects are present in various concentrations but in many cases, certain types of defects predominate[11]. Defects can be categorized as intrinsic defects or extrinsic defects, where the stoichiometry of the structure is maintained in the former and is not in the latter. It can be shown that intrinsic defects cannot be the predominant defect in a growing scale and, therefore, these defects will not be further explained[9]. Extrinsic crystals can be categorized as n-type or p-type where n-types materials are those who transfer charge by negative electron carriers, while p-type materials transfer charge with positive electron carriers. N-type oxides are either metal excess $M_{1+\delta}O$ in which interstitial cations predominate, or oxygen deficit $MO_{1-\delta}$ where oxygen vacancies are the dominant defect. Itinerate electrons are created to maintain charge neutrality.

$$MO = M_i^{\cdot\cdot} + 2e' + \tfrac{1}{2}O_2 \,(11)$$

Metal excess

$$MO = M_M^x + V_O^{\cdot\cdot} + 2e' + \tfrac{1}{2}O_2 \,(12)$$

Oxygen deficit

In p-type oxides, the predominant defect can be metal vacancies in the case of metal deficit, $M_{1-\delta}O$ type oxides, or oxygen excess $MO_{1+\delta}$ in which oxygen interstitials dominate. In these oxides electron holes in the valence band are formed alongside these defects to maintain charge neutrality.

$$MO + \tfrac{1}{2}O_2 = M_M^x + V_M'' + 2O_O^x + 2h^\cdot \,(13)$$

Metal deficit

$$MO + \tfrac{1}{2}O_2 = M_M^x + O_i'' + 2h^\cdot + O_O^x \,(14)$$

Oxygen excess

2.2.4 Doping

When aliovalent species dissolve into oxides, other defects must occur to maintain charge neutrality. Nickel oxide, NiO is a metal deficient oxide and the predominant defect reaction can be written

$$\tfrac{1}{2}O_2(g) = V_{Ni}'' + 2h^\cdot + O_O^x \,(15)$$

When a cation with a lower charge than Ni^{2+} such as Li^+ sits on a nickel site, the defect reaction can be written in two ways. First, it can be viewed as two lithium ions occupying nickel sites and an oxygen atom absorbed from the gas phase to sit on the anion site along with the creation of two electron holes.

$$Li_2O + \tfrac{1}{2}O_2(g) = 2Li_{Ni}' + 2h^\cdot + 2O_O^x \,(16)$$

On the other hand, the dissolved lithium can occupy a nickel vacancy

$$Li_2O + V_{Ni}'' = 2Li_{Ni}' + O_O^x \,(17).$$

As a result of this doping, the vacancy concentration is decreased and the electron hole concentration is increased.

If an ion with a higher valence than Ni^{2+} such as Cr^{3+} is added to NiO, the defect reaction can again be explained from two points of view. If Cr_2O_3 is added to NiO, the Cr^{3+} ions will occupy nickel sites and the extra oxygen will evolve into the gas phase at the expense of two electron holes.

$$Cr_2O_3 + 2h^{\cdot} = 2Cr_{Ni}^{\cdot} + 2O_O^x + \tfrac{1}{2}O_2 \, (18)$$

The dissolution of chromia can also be viewed as Cr^{3+} ions occupying nickel sites, the extra oxygen creating oxygen sites along with nickel vacancies so that the number of sites in the lattice is conserved.

$$Cr_2O_3 = 2Cr_{Ni}^{\cdot} + V_{Ni}'' + 3O_O^x \, (19)$$

As a result of the overall reaction, electron holes are destroyed and nickel vacancies are created.

2.2.5 Reaction Rates

Once a continuous scale has developed between the metal and the gas, Figure 6, three processes must occur in order for the reaction to continue.[12] Oxygen must be adsorbed to the surface of the scale and chemically bonded by gaining two electrons as stated by equation(20).

$$\tfrac{1}{2}O_2 + 2e^- = O^{2-} \quad (20)$$

Metal atoms must ionize at the scale-metal interface giving off electrons as stated by equation(21).

$$M = M^{2+} + 2e^- \, (21)$$

Electrons and ions must diffuse through the scale in such a manner that charge neutrality is maintained. Each of these three processes can control the overall reaction rate, however in most circumstances; diffusion through the scale is the rate controlling step. Wagner's theory of the high temperature oxidation of metals is able to describe this process under simplified conditions when diffusion through the scale will determine the overall rate of the reaction.

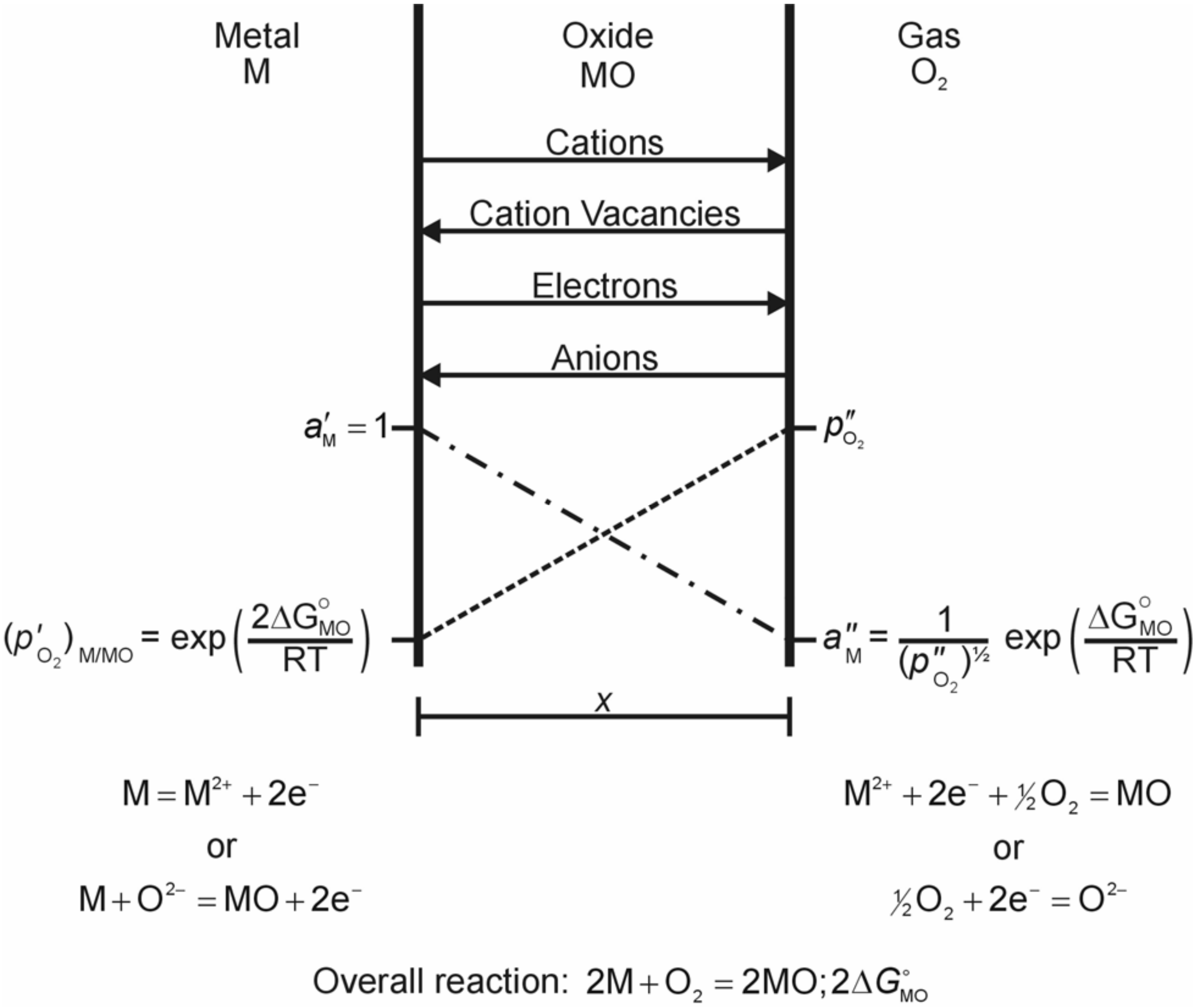

Figure 6. Schematic showing the processes taking place in the oxidation of a metal[9]

2.2.5.1 Wagner theory of oxidation

Assumptions [13]

1. The oxide scale is compact and perfectly adherent
2. The migration of ions or electrons through the scale will determine the overall rate of reaction.
3. Thermodynamic equilibrium is established at the metal-scale interface and the scale-gas interface.
4. Only small deviations from stoichiometry exist in the oxide scale.
5. Thermodynamic equilibrium is established locally throughout the scale.
6. The scale is thick with respect to the distance at which space charge effects occur.
7. The solubility of oxygen in the metal can be neglected.

Thermodynamic equilibrium established at the metal-scale and scale-gas interface creates activity gradients through the scale. These gradients will cause the migration of oxygen ions and metal ions across the scale in opposite directions. Due to the electric charge associated with the ions, an electric field will result from the motion of these particles through the scale, which will in turn cause the motion of electrons through the scale.

The electrochemical potential η defined as equation (22) will govern transport through the scale. In this expression, μ_i, is the chemical potential and φ_i is the electrical potential of a species i, F is Faraday's constant, and z_i is the electronic charge of the species i.

$$\eta_i = \mu_i + z_i F \phi_i \text{ (22)}$$

A gradient in the electrochemical potential will create a force f, acting on mobile species i, in the scale as given in equation (23).

$$f = -\frac{\partial \eta}{\partial x} = \frac{1}{N_A}\left(\frac{\partial \mu_i}{\partial x} + z_i F \frac{\partial \phi}{\partial x}\right) \text{joules particle}^{-1}\text{ cm}^{-1} \text{ (23)}$$

Under this force, the mobile species will be accelerated, which leads to a drift velocity v_i, which is proportional to the force, hence,

$$v_i = -\frac{B_i}{N_A}\left(\frac{\partial \mu_i}{\partial x} + z_i F \frac{\partial \phi}{\partial x}\right) \text{(24)}$$

where B_i is the mobility (average drift velocity per unit force). The negative sign in equation 24 results from the drift velocity taking place in the positive x direction for negative chemical potential and electrical gradients. This force on the species i at concentration c_i will create a flow j_i related to the force by proportionality constant. The flux can then be expressed in terms of concentration and velocity in equation (25) or in terms of the potential gradient in equations (26).

$$j_i = c_i v_i \quad (25)$$

$$j_i = \frac{c_i B}{N_A}\left(\frac{\partial \mu_i}{\partial x} + z_i F \frac{\partial \phi}{\partial x}\right) \text{ mols cm}^{-2}\text{s}^{-1} \quad (26)$$

The mobility of the species i can be related to the partial conductivity σ_i, and to the diffusivity D_i, by analyzing equations (25) and (26) under the limiting case where the electric potential gradient is zero. k_B is the Boltzmann constant..

$$kTB_i = D_i = \frac{RT\sigma_i}{C_i F^2 Z_i^2} \quad (27)$$

Relating equations (26) and (27) allows the flux of a species i to determined as a function of the partial conductivity of the species and the electrochemical potential gradient under which it is being acted upon.

$$j_i = -\frac{\sigma_i}{Z_i^2 F^2}\left(\frac{\partial \mu_i}{\partial x} + z_i F \frac{\partial \phi}{\partial x}\right) \quad (28)$$

This flux equation can describe the motion of electrons, metal ions or oxygen ions. The mobilities of each of these charged species are typically different; however movement at different rates would generate an electric field. The constraint of electrical neutrality requires the coordinated movement of each species.

In most ionic compounds, the mobility of one ion is generally greater than the other by several orders of magnitude. This makes it reasonable to analyze the net flux through the scale by ignoring the movement of the slower ion. If it is assumed that cations are the mobile species, then the relevant fluxes can be expressed as,

$$j_c = -\frac{\sigma_c}{Z_c^2 F^2}\left(\frac{\partial \mu_c}{\partial x} + z_c F \frac{\partial \phi}{\partial x}\right) \quad (29)$$

$$j_e = -\frac{\sigma_e}{Z_e^2 F^2}\left(\frac{\partial \mu_e}{\partial x} + z_e F \frac{\partial \phi}{\partial x}\right) \quad (30)$$

The electrical neutrality condition governing the movement of species through the scale is given in equation (31).

$$j_c z_c + j_e z_e = 0 \, (31)$$

Substitution of equations (30) into (31), allows the electrical potential gradient to be determined.

$$\frac{\partial \phi}{\partial x} = -\frac{1}{F(\sigma_C + \sigma_e)}\left[\frac{\sigma_C}{z_c}\frac{\partial \mu_c}{\partial x} + \frac{\sigma_e}{z_e}\frac{\partial \mu_e}{\partial x}\right] (32)$$

Upon substitution of equation (32) back into (30) and replacing z_e=-1

$$j_c = -\frac{\sigma_c \sigma_e}{z_c^2 F^2 (\sigma_C + \sigma_e)}\left[\frac{\partial \mu_c}{\partial x} - \frac{z_c}{z_e}\frac{\partial \mu_e}{\partial x}\right] (33)$$

Furthermore, the ionization of metal can be expressed by the reaction

$$M = M^{z_c} + Z_c e \;\; (34)$$

and at equilibrium

$$\mu_M = \mu_c + z_c \mu_e \;\; (35)$$

Combining equations (33) and (35)

$$j_c = -\frac{\sigma_c \sigma_e}{z_c^2 F^2 (\sigma_C + \sigma_e)}\frac{\partial \mu_M}{\partial x} (36)$$

This equation describes the localized cationic flux at any point in the scale.

The values of σ_c, σ_e and μ_M vary throughout the scale and it is therefore necessary to integrate equation (36) to obtain a total flux. The limits of integration are the chemical potential of the metal at the metal-scale interface $\mu_M^{'}$ and at the scale-gas interface $\mu_M^{''}$.

$$j_c \int_0^x dx = -\frac{1}{z_c^2 F^2}\int_{\mu_M^{'}}^{\mu_M^{''}} \frac{\sigma_c \sigma_e}{\sigma_c + \sigma_e} d\mu_M \text{ mol cm}^{-2} \text{ s}^{-1} \; (37)$$

$$j_c = \frac{1}{z_c^2 F^2 x}\int_{\mu_M^{''}}^{\mu_M^{'}} \frac{\sigma_c \sigma_e}{\sigma_c + \sigma_e} d\mu_M \;\; (38)$$

The cation flux is assumed to be independent of x, which means that there are small deviations from stoichiometry in the scale.

Alternatively, the cation flux can be expressed in terms of the concentration of the metal in the scale C_M mol cm^{-3} where x is the scale thickness.

$$j_c = C_M \frac{dx}{dt} \quad (39)$$

When the rate of reaction is controlled by diffusion, the reaction rate will decrease as the thickness in which diffusion must occur through is increased. This process can be described by the parabolic rate law.

$$\frac{dx}{dt} = \frac{k'}{x} \quad (40)$$

Upon integration, equation (40) becomes equation (41) where it can be observed that the scale thickness is proportional to the square root of time.

$$x^2 = 2k't \, (41)$$

The proportionality constant *k'* can be expressed in terms of the conductivity of diffusing species by related equation (38), (39) and (41).

$$k' = \frac{1}{C_M z_c^2 F^2} \int_{\mu_M''}^{\mu_M'} \frac{\sigma_c \sigma_e}{\sigma_c + \sigma_e} d\mu_M \ \mathrm{cm^2 s^{-1}} \, (42)$$

Assuming the oxide is an electrionic conductor where $\sigma_e >> \sigma_c$, then equation (42) can be simplified to equation (43).

$$k' = \frac{1}{C_M z_c^c F^2} \int_{\mu_M''}^{\mu_M'} \sigma_C d\mu_M \, (43)$$

This expression can be further simplified if the Nernst-Einstein relation, equation (44) is applied to equation (43), producing equation (45).

$$D_i = B_i kT = \frac{RT\sigma_i}{C_i z_i^2 F^2} \quad (44)$$

$$k' = \frac{1}{RT} \int_{\mu_M''}^{\mu_M'} D_M d\mu_M \ \mathrm{cm^2 s^{-1}} \, (45)$$

This rate constant *k'*, commonly known as the 'practical tarnishing constant' is not easily calculated because the activity and diffusion coefficient must be known across the scale. Furthermore it is difficult to directly measure because the scale thickness as a function of time must be known. Commonly the parabolic rate constant *k"* is measured where

$$\left(\frac{\Delta m}{A} \right)^2 = k''t \quad (46).$$

Here *k"* is in units of $g^2cm^{-4}s^{-1}$. This rate constant can be determined by continuously measuring the weight change of a metal of known surface area.

The two rate constants can be related through physical constants. For a scale composed of the compound M_xO_y , V_{MO} is the molar volume of the oxide M_xO_y, y is the stoichiometric coefficient of the anion, and M_O is the atomic mass of the anion.

$$k' = \frac{V^2 y^2}{2M_O^2} k'' \quad (47)$$

2.2.6 The Oxidation of Nickel

The nickel-oxygen system is viewed to be a model system to study the high temperature oxidation of metals because at normal pressures and temperatures, NiO is the only stable oxide.[9] Early experiments found that NiO is a metal deficit, p-type semiconductor that grows by outward diffusion of cations.[14] Such an oxide grows by metal ions and electrons migrating from the metal to the scale gas interface while metal vacancies and electron holes move toward the scale metal interface.

2.2.6.1 NiO Defect Structure

It is clear that the predominant defect in nickel oxide is the cation vacancy,[9, 14, 15], and numerous studies have been conducted to determine the concentration of these defect.[16, 17] Many other investigations have been conducted to determine the charge on this defect but there is still debate on this subject. The reaction in equation (48) describes the formation of doubly ionized nickel vacancies as a result of oxidation.

$$\tfrac{1}{2}O_2 = V_{Ni}'' + 2h^{\cdot} + O_O^x \quad (48)$$

The equilibrium constant for this reaction is given in equation (49).

$$K = \frac{[V_{Ni}'']p^2}{p_{O_2}^{1/2}} \quad (49)$$

Under the neutrality condition that $2\left[V_{Ni}''\right] = p$ the concentration of vacancies and electron holes will have the following dependence on the oxygen partial pressure.

$$2[V_{Ni}''] = p \propto p_{O_2}^{1/6} \, (50)$$

If the vacancies are singly ionized then the reaction in equation (51) will occur.

$$\tfrac{1}{2}O_2 = V_{Ni}^{'} + h^{\cdot} + O_O^x \, (51)$$

$$K = \frac{\left[V_{Ni}'\right]p}{p_{O_2}^{1/2}} \, (52)$$

In the case where singly ionized vacancies are predominant then the neutrality condition will be $\left[V_{Ni}'\right] = p$ and the vacancy and electron hole concentration will be proportional to the oxygen partial pressure raised to the 1/4th power.

$$[V_{Ni}'] = p \propto p_{O_2}^{1/4} \, (53)$$

The parabolic rate constant is governed by the diffusivity of nickel through nickel oxide, and therefore is proportional to the concentration of vacancies. Experimental observations have found that the parabolic rate constant is proportional to the *nth* root oxygen pressure with *n* varying between 3.5-6 in the temperature range 900-1400°C[14]. This result implies that the both singly and doubly ionized vacancies are present and that their concentration controls the growth kinetics of NiO.

The pressure dependence of vacancy and electron hole concentrations of bulk NiO have been calculated by a number of investigators and this concentration is proportional to the nth root of the oxygen partial pressure.

$$[V_{Ni}] \propto p \propto p_{O_2}^{1/n} \, (54)$$

Farhi and Petot-Ervas[18] have found the value of *n* to be between 4-5 in the temperature range 1000-1400°C at an oxygen partial pressure of 1 atm and to be between 4.5-6 at an oxygen partial pressure of $2x10^{-4}$. They find the fraction of doubly ionized vacancies to be in between 4.5% to 24.6% of the total number of vacancies at 1atm at 1000°C.

The equilibrium constant for both equations (49) and (52) increase with temperature and as a result, the concentration of vacancies increases with temperature and oxygen pressure. The degree of non-stoichiometry of $Ni_{1-x}O$ is small, between $x = 0.86x10^{-4}$ at 836°C and $x = 4.25x10^{-4}$ at 1000°C.[16] At this concentration, the vacancies can be considered randomly distributed behaving as a dilute solution. This allows the existence of defect clusters to be ignored. Tretyakov and Rapp[16] have determined the non-stoichiometry as a function of temperature using coulometric titration. The concentration of nickel vacancies as a function of temperature and pressure is given in equation (55).

$$\left[V_{Ni}^{"}\right] = 0.51 p_{O_2}^{1/6} \exp\left(\frac{-19{,}000}{RT}\right) (55)$$

The small degree of non-stoichiometry makes the purity of the nickel that is being oxidized important. As previously discussed, trivalent ions increase the defect concentration according to the equation (18). If the impurity concentration is on the order of the native defect concentration the growth kinetics will be affected.

2.2.6.2 Scale Morphology

NiO grown on high purity nickel forms a dense adherent scale. Platinum markers placed on the metal surface where found at the metal scale interface demonstrating outward growth. This scale is composed of columnar grains. Platinum markers placed on less pure nickel were found in the oxide scale between a dense outer layer and a porous inner layer.[19] This indicates that the outer layer grows by outward diffusion of nickel, while the inner layer grows by the inward transport of oxygen. During growth, the oxide tends to separate from the metal due to insufficient plasticity. When the scale loses contact with metal, the oxygen activity at the inner surface of the oxide increases. This causes the oxide to dissociate. The oxygen can then migrate as a gas through the created pore and oxidize the surface of the metal.

2.2.6.3 Growth Kinetics

A plot of the parabolic rate constant versus reciprocal temperature is shown in Figure 7. This graph can be broken down into two regions. At high temperatures, there is constant activation energy from 180-240 kJ/mol.[20] Calculations of the activation energy for the bulk diffusion of nickel in NiO are 154-254 kJ/mol.[20] This is a strong indication that bulk diffusion is the rate determining step in the growth of NiO. The concentration of cation vacancies is large enough that a small amount of impurities do not affect the overall kinetics in this temperature range. Wagner's theory of oxidation predicts that the parabolic rate constant is directly proportional to the diffusivity of Ni in NiO.

$$k_p^{"} = 6.4\left(D_{Ni}^{*}\right) \quad (56)$$

Diffusion data for Ni in NiO measured by Atkinson and Taylor[21, 22], and Volpe and Reddy[23], along with measured values of the parabolic rate constant show good agreement with equation (56) at high temperatures.

At lower temperatures, the growth of NiO is strongly affected by the presence of impurities and grain boundaries. As a result, over the temperature range 600-1000°C the data in the literature for the parabolic rate constant shows scatter.

The native defect concentration of NiO decreases with temperature. When the impurity concentration is similar to the native defect concentration, the total cation vacancy concentration will be measurably affected by the concentration of impurities. The most common impurities are either M^{2+} ions (Co^{2+},Mg^{2+}, Fe^{2+}) which do not effect the vacancy concentration or M^{3+}(Cr^{3+}, Al^{3+}) ions that increase the vacancy concentration when they substitute for Ni in the lattice. As a result, impure nickel tends to oxidize more rapidly than pure nickel.

The presence of short circuit diffusion paths such as grain boundaries and dislocations also become more important at lower temperatures. The activation energy for diffusion along grain boundaries is less than the activation energy for bulk diffusion and as temperatures decrease, the effective diffusivity along short circuit paths increases with respect to bulk diffusion.[20] The relationship of the parabolic rate constant and the lattice diffusion coefficient D_L, grain boundary diffusion coefficient D_{gb}, the grain boundary thickness δ, and the average oxide grain size is G_t.[24].

$$k_p^{"} = 6.4\left[D_L^* + \frac{2\left(D_{gb}\delta\right)}{G_t}\right] (57)$$

At temperatures lower then 600°C there is limited data on the parabolic rate constants for nickel and in that data there is substantial scatter. The native defect concentration is low enough at this temperature that specimen purity becomes a crucial factor.

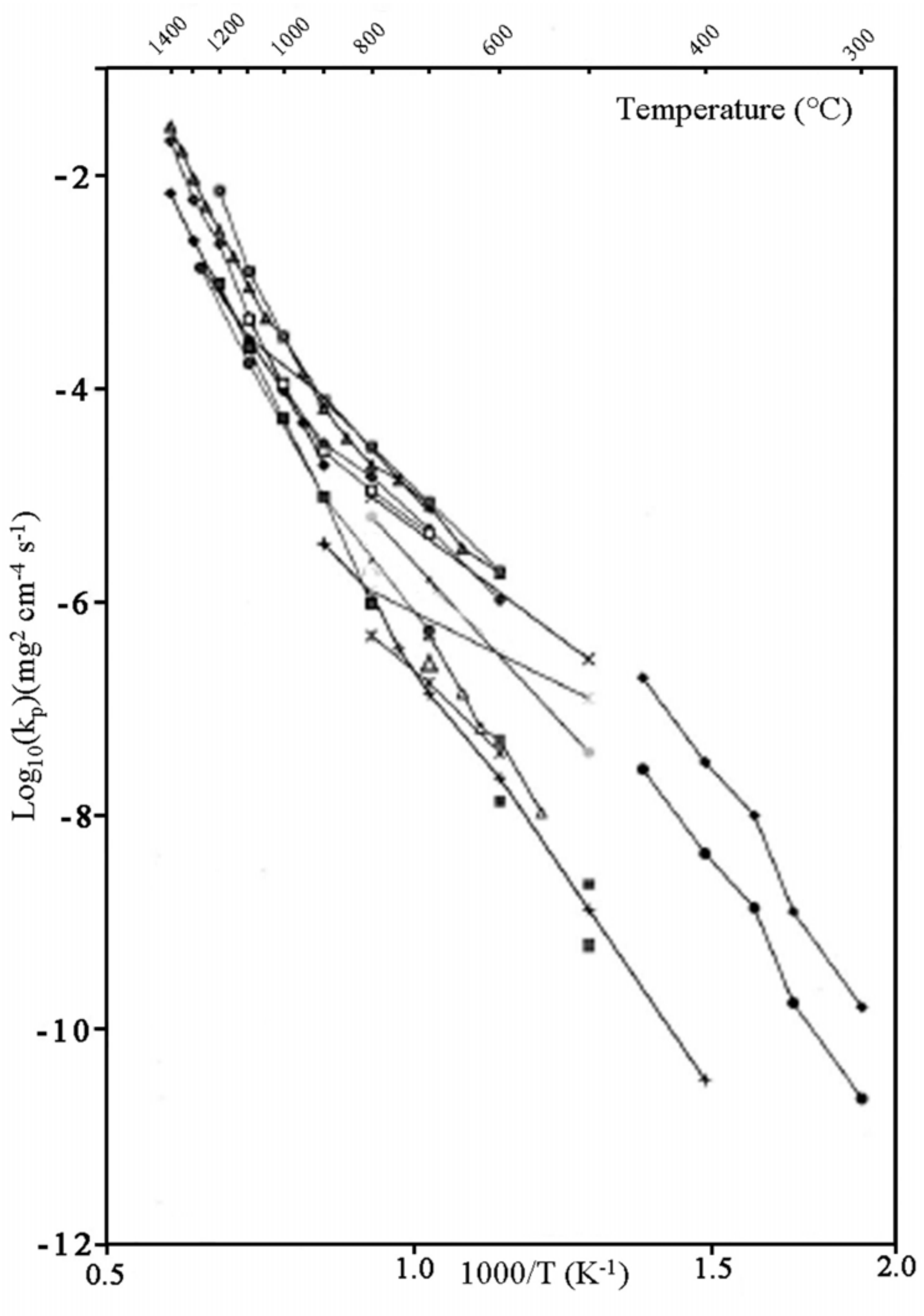

Figure 7. Arrhenius plot for the oxidation of nickel, after Peraldi et al.[18]

2.2.7 Reactive Element Effect

While developing Nichrome (Ni-20%Cr) heating elements in the late 1930's, Pfiel[25] found that additions of rare earth elements, that where initially acting as melt deoxidants, significantly increased the lifetimes to failure due to thermal cycling of the heating elements.[25, 26] The beneficial contributions became known as the 'rare earth effect' and it was utilized to improve the oxidation resistance of many alloys. Over the last 70 years, the rare earth, or reactive element effect (REE) has become an essential component in most high temperature alloys.

Additions elements with a high affinity for oxygen such as Y, Zr, Ce, Ca, Si, and Ba are known to improve the properties of different oxides in different ways. Many studies have investigated the REE on alumina forming alloys, but the details of these studies will be largely ignored here, and the focus will be placed on outward growing scales, as they receive the most attention as interconnect candidates.

When alloys that form outward growing oxides such Cr_2O_3, NiO, CoO, and FeO contain small additions of reactive elements, two beneficial effects have been found in these systems: improved oxide adherence, decreased growth rate.[26, 27] Most of the research examining the effect of reactive elements on outward growing scales has been conducted on chromia, but these effects are seen in other outward growing scales.[27] While it is well established that additions of reactive elements can improve the properties of an oxide scale, the mechanisms that cause this improvement are not as well understood.

2.2.7.1 Decreasing Scaling Kinetics

The two mechanisms that are proposed to explain the decrease in scale growth kinetics will be examined. The first of these mechanisms centers on short circuit diffusion while the second focuses on interface reactions.

A major contribution to the total growth of oxides at intermediate temperatures is by short circuit diffusion[12], via grain boundaries, dislocations and free surfaces. Both cations and anions are able to diffusion along grain boundaries in NiO[22, 28] and Cr_2O_3 while cation diffusion is predominant along dislocations[28]. One proposed mechanism for the reactive element effect is a decrease in dislocation density[26]. If the oxide grain size is small enough so the equilibrium dislocation spacing is smaller than the grain size, then the dislocation will not be stable. Under these circumstances the outward diffusion via dislocations is greatly decreased while the inward diffusion of oxygen along grain boundaries will be increased due to the smaller grain size and hence greater grain boundary density.

Another mechanism focuses on the segregation of reactive elements to grain boundaries[29]. Reactive elements have been found to segregate to boundaries and there are several reasons why this phenomenon could decrease grain boundary diffusion. In metals, it is well known that the large atoms reduce the grain boundary flux[30] where it is assumed that the solutes can block movement by filling the open space of the grain boundary. A similar mechanism could occur in oxides[29]. Another proposed mechanism is that the presence of reactive elements along grain boundaries decreases the concentration of solvent cations (Ni^{2+} in the case of NiO). If charge neutrality is preserved at grain boundaries, then the ratio of cations to oxygen ions is fixed by the charge of the cation. When large immobile reactive element ions are present at grain boundaries, there are fewer sites available for the solvent cations. This effect would decrease the cation flux without decreasing the inward oxygen flux. It is not clear if one of these mechanisms dominates or if it is a combination of all.

An alternative mechanism known as the poisoned interface model (PIM) has been proposed by Pieraggi and Rapp[31]. In the above description of the Wagner theory of oxidation, it was stated that three processes must occur in order for scale growth to occur: metal-scale interface reactions, solid state diffusion, and the scale-gas interface reactions. In the Wagner treatment, it is assumed that rate limiting step is diffusion through the scale and the other processes do not affect the kinetics. However, if the interface reactions are considered, then the weight change as a function of time can be expressed as equation (58) where w is weight gain, k_L is the linear rate constant in $gcm^{-2}s^{-1}$ and k_p is the parabolic rate constant $g^2cm^{-4}s^{-1}$ which was previously referred to as k''.

$$\frac{dw}{dt}=\left(\frac{1}{k_L}+\frac{2w}{k_p}\right)^{-1} \quad (58)$$

When only cationic diffusion or anionic diffusion is occurring, solutions to (58) will be in the form

$$t=\frac{w}{k_L}+\frac{w^2}{k_p} \quad (59).$$

If both anionic and cationic diffusion occur simultaneously, then equation (58) becomes equation (59).

$$\frac{dw}{dt}=\left(\frac{dw}{dt}\right)_C+\left(\frac{dw}{dt}\right)_A=\left(\frac{1}{k_{LC}}+\frac{2w}{k_{pC}}\right)^{-1}+\left(\frac{1}{k_{LA}}+\frac{2w}{k_{pA}}\right)^{-1} \quad (59)$$

The subscripts C and A refer to cationic and anion rate constants respectively. Equation (59) has solutions in the form

$$t = A\ln(1+Bw)+Cw+Dw^2 \quad (60)$$

But, the logarithmic term can be expanded to the first terms of Taylor series if B is assumed to be much less than one. Therefore, the net linear rate constant and the net parabolic rate constant can then be written as

$$\left(\bar{k}_L\right)^{-1}=\left(k_{LA}+k_{LC}\right)^{-1} \quad (61)$$

and

$$\left(\bar{k}_p\right)^{-1}=\left[\frac{k_{LA}^2}{k_{pA}}+\frac{k_{LC}^2}{k_{pC}}\right]\left(k_{LA}+k_{LC}\right)^{-2} \quad (62)$$

so that equation (60) becomes equation (63).

$$t=\frac{w}{\left(k_{LA}+k_{LC}\right)}+\frac{w^2}{\left[\frac{k_{LA}^2}{k_{pA}}+\frac{k_{LC}^2}{k_{pC}}\right]\left(k_{LA}+k_{LC}\right)^{-2}} \quad (63)$$

Equation (63) shows that if k_{LC} becomes large enough, then the value of k_{pC} no longer has an effect of on the total growth kinetics and the total weight change can be dominated by k_{pA}.

During oxidation, misfit dislocations are created at the metal-scale interface due to lattice mismatch. Climb of these dislocations allows metal ions to enter the scale and this reaction determines k_L. Under normal conditions, the dislocations can climb rapidly enough so as not to affect the total reaction rate. However, when a reactive element is added, the larger reactive elements diffuse to these sites and pin the dislocations inhibiting the surface reaction. This reaction becomes slow enough so that inward diffusion of oxygen along grains boundaries determines the reaction and as a result the growth direction changes from outward to inward and the total scaling kinetics are reduced.

2.2.7.2 REE in NiO forming alloys

The addition of reactive elements is known to significantly change the scaling behavior of NiO forming alloys. These reactive elements are often added as alloying additions, usually at concentrations of less then one atomic percent [32, 33]. Many other investigations use surface coatings to apply the reactive elements. The coatings can be deposited by a variety of methods including sputtering, evaporation[27], and sol-gel [34] dipping. The best results are obtained when the coating is continuous across the surface with a thickness on the order of 100nm. The most common reactive element additions used are Y_2O_3, CeO_2, and La_2O_3, but dramatic effects have been observed with CaO, SrO[27], and SiO_2[34].

When alloys with reactive element additions are exposed in the temperature range 600-1000°C, the parabolic rate constant decreases typically by one to two orders of magnitude. This is accompanied by a change in growth direction, from predominantly outward, to predominantly inward. The adherence of NiO is generally very good on nickel, and this does not change with the addition of reactive elements.

Moon [35] performed a study of Ni coated with CeO_2 that was applied using sol-gel deposition. When exposed at 900°C, the effectiveness of the coating in reducing the oxidation rate increases with coating thickness. However, additional coating beyond a thickness of approximately 2.5nm did not produced a further decrease in the growth rate. The surface morphology of oxidized Ni with a critical coating thickness produces a uniform microstructure. Coatings of thickness, 2-2.5nm produced a nodular surface structure. These coatings of intermediate thickness produced a substantial reduction in growth rate, with the growth kinetics being slightly greater than the thicker coated specimens.

Moon also performed transmission electron microscopy (TEM) on the oxide grown on nickel coated with CeO_2. The scale was composed of three layers. The outer layer consisted of columnar grains a few CeO_2 particles at grain boundaries. The middle layer was composed of fine grains and a high concentration of ceria. TEM-EDS analysis found cerium at grain boundaries in NiO at 10-30at% within the boundary width. The inner layer consisted of equiaxed grains with minimal ceria. Moon proposed that the middle layer with the high CeO_2 concentration limited the total growth of the oxide by retarding the rate at which nickel ions could reach the scale-gas interface.

2.3 THE SOLUBILITY OF GASES IN METALS

The gases that can be found in solution in metals, at measurable quantities are diatomic gases such as hydrogen, oxygen, and nitrogen. The dissolution of a diatomic gas X_2 in a metal can be expressed by the reaction.

$$\tfrac{1}{2}X_2 = X(dissolved.in.metal) \; (64)$$

The equilibrium constant *K*, for this reaction can be written as equation (65)

$$K = \frac{a_X}{p_{X_2}^{1/2}} \; (65)$$

where a_x is the activity of the gas dissolved in the metal and it is assumed that the activity of the gas is equal to the partial pressure of the gas. If a compound does not form between the solute gas atoms and the metal, then the activity of the solute will follow Henry's law, under most circumstances. In this case, the activity of the solute is proportional to its concentration over a limited range of compositions. The proportionality factor $\gamma_i°$ is known as the Henry's law constant and N_i is the concentration of solute.

$$a_i = \gamma°_i N_i \; (66)$$

Relating equations (65) and (66) produces

$$K = \frac{\gamma_x°N_x}{p_{X_2}^{1/2}} \; (67)$$

which can be rearranged into equation (68).

$$\frac{p_{X_2}^{1/2}K}{\gamma_x°} = N_X = Sp_{X_2}^{1/2} \; (68)$$

This equation is known as Sievert's law and *S* is the Sievert's law constant. Sievert's law shows that the concentration of a dissolved diatomic gas is proportional to the square root of the gas pressure with which the metal is in equilibrium.

2.3.1 The solubility of gases in nickel

The solubility of oxygen and hydrogen in nickel follow Sievert's Law. Park and Altstetter [36] determined the solubility of oxygen in nickel when NiO is in equilibrium with nickel as a function of temperature and the relation is shown in equation (69).

$$C_O^s = 8.3(+5.1/-3.5)\exp\left[\frac{-55 \pm 1.3}{RT} kJ/mole\right] \text{at.\%} \quad (69)$$

The solubility of oxygen at 800°C is $C_O^s = 0.0174$ at. % or 174 atomic ppm.

The solubility of hydrogen in nickel at 1 atm of hydrogen gas was determined as a function of temperature by Jones and Pehlke[37].

$$C_H^{Ni} = 5.87x10^{-5} \exp\left(3.767 - \frac{1889}{T}\right) \text{at\%.} (70)$$

At 800°C and 1atm $C_H^{Ni} = 0.0437 at\%$.

2.3.2 The solubility of gases in silver

Both hydrogen and oxygen dissolve into silver according to Sievert's law. The solubility of oxygen is expressed as a function of temperature in equation (80).[38]

$$C_O^{Ag} = 1.2x10^{-3} \exp\left(\frac{-38.6kJ/mol}{RT}\right) at\% \quad (71)$$

The amount of oxygen dissolved in silver is substantially higher then in nickel and other candidate interconnect materials.

The solubility of hydrogen in silver can be expressed as equation (72) at 800°C.

$$C_H^{Ag}(at\%) = \left(2.98x10^{-5}\right) p_{H_2}^{1/2} \quad (72)$$

2.4 ELECTRONIC PROPERTIES

2.4.1 The electronic structure of solids

2.4.1.1 Metals

The electronic structure of metals can be viewed as a first approximation as ion cores in an electron sea. This is known as the free electron model. The Pauli Exclusion Principle states that no two electrons with overlapping orbitals can have identical quantum numbers. As a result, an energy band develops centered around the energy levels of the individual atoms with the width of the band being a function of the number of overlapping orbitals. The top most filled energy level is known as the Fermi energy, E_F.[39]

$$E_F = \frac{\hbar^2}{2m}\left(\frac{3\pi^2 N}{V}\right)^{2/3} \quad (73)$$

In equation (73) m is the electron mass, N is the number of free electrons, V is the volume of the crystal and $\hbar$ is Plank's constant divided by 2π. The distribution of available electron energy levels in a solid, known as the density of states $D(E)$, given by equation (74).

$$D(E) = \frac{dN}{dE} = \frac{V}{2\pi^2}\left(\frac{2m}{\hbar^2}\right)^{3/2} E^{1/2} \quad (74)$$

At absolute zero, electrons are in their lowest energy states. As the temperature rises, the distribution of filled energy states is given by the Fermi-Dirac distribution.[39] This equation gives the probability of an electron orbital of energy E, being occupied at a given temperature.

$$f(E) = \frac{1}{\exp\left[\frac{E - E_F}{kT}\right] + 1} \quad (75)$$

The periodic structure of a crystal is known to produce Bragg reflections of waves propagating at specific energies. The Bragg reflection of electron waves in a crystal forbids electrons from having certain energies because Bragg reflected wavelike solutions of the Schrödinger equation do not exist.[39] These forbidden energy levels are known as the energy gap or band gap. The location and size of the band gap is a feature of a material that determines many of its electronic properties. An essential feature of a metal is that the Fermi energy is within an energy band.

2.4.1.2 Insulators and Semiconductors

Materials whose valence electrons exactly fill up a band are known as insulators or semiconductors. This commonly occurs in covalent and ionic compounds, and elemental semiconductors such as Si, and Ge. A completely full band or completely empty energy band cannot conduct electricity and therefore electrons must have sufficient energy to jump across the band gap in order to conduct. As a result, the size of the energy gap dictates the conductivity of a material and this is the distinction between semiconductors and insulators.

Many transition metal oxides such as NiO, CoO, and FeO, have filled energy bands along with unfilled 3d electron orbitals. For example a Ni^{2+} ion will have the electron configuration $[Ar]3d^8$. Band theory predicts that these materials should behave as metals due to their partially filled d-bands but experimentally[39], this is not the case. It is found that the d-orbitals of the cations have limited interaction with other cations.[40] As a result, the bandwidth of these compounds is very small and they behave as semiconductors.

2.4.2 Electrical Conductivity

When an electron is in the presence of an electric field ε, a force *f* is generated.

$$f = -e\varepsilon = m\frac{dv}{dt} \quad (76)$$

where *v* is velocity, *t* is time, *m* and *e* are the mass and charge on the electron, respectively. When an electron is accelerated by an electric field in a crystal, collisions occur between electrons and phonons, imperfections and impurities. If the time between collisions is τ, then the equation of motion for an electron in the presence of an electric field becomes equation (77)

$$m\left(\frac{dv}{dt}+\frac{v}{\tau}\right)=-e\varepsilon \quad (77)$$

As the electrons are accelerated, their velocity increases which decreases the time between scattering events. As a result of these opposite forces, a limiting velocity, or drift velocity of the electron is achieved. The electron velocity is constant under constant applied field, and the first term vanishes in equation (77) leaving equation (78).

$$v=\frac{-e\tau\varepsilon}{m} \quad (78)$$

The current density *J*, is the electron velocity multiplied by the electron concentration *n*, and the charge of the electron.

$$J=nev=\frac{-ne^2\tau\varepsilon}{m} \quad (79)$$

This is known as Ohm's law. Ohm's law is often stated as

$$J=\sigma\varepsilon \quad (80)$$

where the proportionality constant σ, is known as the conductivity.

$$\sigma=\frac{-ne^2\tau}{m} (81)$$

The mobility *B* relates the drift velocity of an electron to the applied field

$$B=\frac{v}{\varepsilon} (82)$$

and therefore the conductivity can be expressed as equations (83).

$$\sigma=neB \quad (83)$$

In the case when electron holes as well as electrons are mobile species

$$\sigma=neB_n+peB_p (84)$$

where *p* is the concentration of electron holes. The electrical resistivity ρ, is the reciprocal of the conductivity.

$$\rho=\frac{1}{\sigma}=\frac{m}{ne^2\tau} (85)$$

2.4.3 Sources of Electrical Resistivity

The conductivity of known materials varies over 30 orders of magnitude[10, 40]. In addition, a given material's conductivity can vary several orders of magnitude as a function of temperature and atmosphere[9]. To understand the wide variation, it is useful to look at the terms in equation (86).

$$\sigma = \frac{-ne^2\tau}{m} \quad (86)$$

The scattering time, effective mass, and number of charge carriers are the major factors that determine the conductivity but the importance of each factor is different for different materials

2.4.3.1 Scattering Time

The scattering time τ, is measure of time between scattering events of an electron traveling through a crystal. The primary scattering centers are the crystal lattice and impurities. Matthesien's rule[39] relates the total scattering time to the individual scattering events.

$$\frac{1}{\tau_{total}} = \frac{1}{\tau_{impurity}} + \frac{1}{\tau_{lattice}} \quad (87)$$

The impurity scattering is a function of purity, and is nearly constant with temperature. Above the Debye temperature, phonon energy increases in proportion to temperature[39]. The increased vibration of the lattice causes an increase in scattering. As a result the scattering time decreases with increased temperature, and all other factors being equal, the conductivity will decrease.

2.4.3.2 Carrier Density

Electrons gain energy when in the presence of an electric field as stated above. In a metal, the band holding the highest energy electrons is not filled and they can move into orbitals of higher energy in the presence of an electric field. As a result, metals have high carrier concentrations, on the order of 10^{22}cm^{-3}. The Fermi-Dirac equation describes the effect of temperature on electron energy and under most circumstances, the concentration of electrons that can act as charged carriers will not be significantly affected by temperature in metals.

The carrier density in semiconductors is an exponential function of temperature. At absolute zero, the valence band of the semiconductor is completely full, the conduction band is empty and there are no charge carriers. As the temperature is increased, the energy of the electrons increases according to the Fermi-Dirac distribution and there becomes a probability that electrons will gain sufficient energy to be excited across the band gap. The number of electrons in the conduction band is a function of temperature and band gap energy E_g.

$$n = \int_{E_C}^{\infty} D(E) f(E) dE = 2\left(\frac{m_e kT}{2\pi\hbar^2}\right)^{3/2} \exp\left[\frac{E_F - E_C}{kT}\right] \quad (88)$$

When an electron is excited from the valence band to the conduction band, an electron hole is left in the valance band. These electron holes can also carrier charge and the concentration if electron holes p, is given in equation (89).

$$p = \int_{-\infty}^{E_V} D(E) f(E) dE = 2\left(\frac{m_h kT}{2\pi\hbar^2}\right)^{3/2} \exp\left[\frac{E_V - E_F}{kT}\right] \quad (89)$$

In addition to thermally generated carriers, the presence of certain impurity atoms can drastically affect the carrier concentration. These impurities are known as dopants. If the valance of the dopant atom is greater than the host atoms of the crystal, then that atom will donate an electron. These atoms are known as donors. Similarly, if the valence of the dopant atom is less than the host atoms, then this atom will take an electron from the crystal creating an electron hole. These dopants are called acceptors.

The addition of dopant atoms creates new energy levels. When considering donors, the number of electrons added to the conduction band can be found by determining the number of donor electrons that will be ionized at a given temperature.

$$n = \left[n_D 2\left(\frac{m_e kT}{2\pi\hbar^2}\right)^{3/2}\right]^{1/2} \exp\left[\frac{E_C - E_D}{2kT}\right] \quad (90)$$

The carrier concentration of transition metal oxides can also be a function of the oxygen partial pressure in which the oxide is in equilibrium. For example, a decrease in oxygen partial pressure can create oxygen vacancies. In response to the net positive charge of the vacancy, free electrons are produced. Similarly, increases in oxygen pressure can cause oxygen to be absorbed into the crystal creating metal vacancies. Electron holes are produced to compensate for this defect.

2.4.3.3 Effective Mass

The mass of an electron in a vacuum is well known. Under an applied electrical force, the electron will be accelerated according to Newton's law. In a crystal, electrons are in the presence of an electric field due to the periodic arrangement of electrons and ions and as a result, the electron will not accelerate as if it has the mass of a free electron. These electrons are said to have an effective mass m*[39]. This is an important parameter in the conductivity of elemental semiconductors.

2.4.4 Polaron Conduction

At high temperatures, electron-phonon interactions become an important factor in the conduction of ionic materials. The presence of a conduction electron induces a strain field in an ionic crystal.[39] When the electron moves from one region of the crystal to another, it has to pull the heavy ion cores with it, increasing the effective mass. When conduction electrons are itinerant but affected by the electron-phonon interaction, they are known as large polarons. When the effect of the polarization is greater, electrons become trapped on a single ion. At elevated temperatures, the sufficient thermal energy allows the electron to hop from site to site. These particles are known as small polarons and they are the predominant charge carrier in many transition metal oxides[41].

Small polarons can be viewed as charged particles when they are trapped at an ion and therefore transport can be viewed as in reference to the diffusion of a charged particle. The

Nernst-Einstein relationship can be used to relate diffusivity of the small polaron to their conductivity σ to the diffusivity *D*.

$$\sigma = \frac{c_i z_i^2 F^2}{RT} D \, (91)$$

The temperature dependence of the diffusion coefficient is given in equation (92) and follows and Arrhenius relationship.

$$D = D_O \exp\left(\frac{-E_m}{RT}\right) (92)$$

Also, the concentration of electron holes also follows an Arrhenius relationship.

$$p = p_O \exp\left(\frac{-E_p}{RT}\right) (93)$$

Equations (91), (92), and (93) produce Equation (94).

$$\sigma T = \sigma_O \exp\left(-\frac{\left(E_p + E_m\right)}{RT}\right) (94)$$

where

$$\sigma_O = D_O p_O \frac{c_i z_i^2 F^2}{RT} \, (95)$$

The product of σ*T* has the same temperature dependence as the diffusion coefficient, and the concentration of electron holes. The determination if the activation energy of conduction can be found by plotting *ln(*σ*T)* vs. *1/T*.

2.5 FUEL CELLS

Fuel cells are electrochemical devices that efficiently convert the chemical energy of reaction into electrical energy while emitting low levels of pollution.[42] While there are many types of fuel cells, all cells contain the same building blocks of an anode (negative electrode) joined to an ionically conducting material known as the electrolyte which is in turn connected to the cathode (positive electrode). In this sense, the operation of a fuel cell is similar to a battery. The difference between the two is that in a battery, the total output is limited by that amount of reactants. In a fuel cell, the reactants are continuously fed into the cell and the cell can produce electricity as long as fuel is provided.

The different types of fuel cells can be most easily be categorized by the type of electrolyte they use. Table 2 shows the most commonly used types of fuel cells and lists some of their basic characteristics.

Table 2. Table listing the different types of fuel cells and some of their characteristics

	Proton Exchange Fuel Cell	**Alkaline Fuel Cell**	**Phosphoric Acid Fuel Cell**	**Molten Carbonate Fuel Cell**	**Solid Oxide Fuel Cell**
Electrolyte	Ion Exchange Membrane	Potassium Hydroxide	Liquid Phosphoric Acid	Molten Carbonate	Solid Oxide
Operating Temperature	80°C	65-220°C	205°C	650°C	600-1000°C
Charge Carrier	H^+	OH^-	H^+	$CO_3^=$	$O^=$

2.5.1 Solid Oxide Fuel Cells

SOFCs operate in the temperature range 600-1000°C.[42] The high temperature promotes rapid reaction kinetics which allows hydrocarbons to be used as fuel gases in addition to hydrogen, without the use of precious metal catalysts. However, the high operating temperature places stringent demands on materials selection. Developing materials that can withstand the aggressive environment of the SOFC is the key challenge holding back their commercial development.

2.5.1.1 Electrochemical reactions in SOFCs

The electrochemical reaction which allows the fuel cell to generate electricity occurs at the three-phase interfaces created between the electrode, electrolyte and the gas.

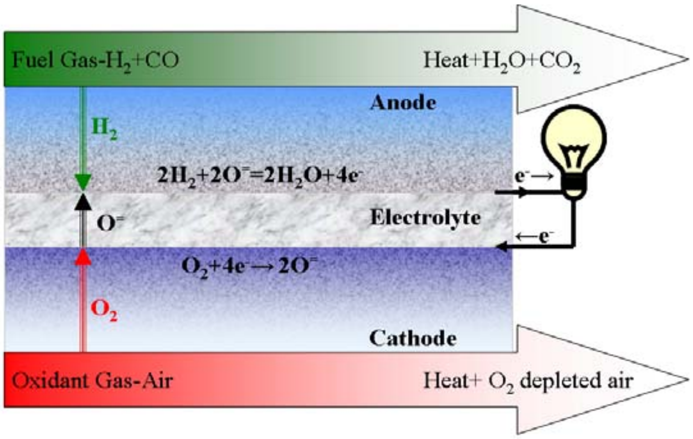

Figure 8. Schematic of a fuel cell

An oxidant gas, typically air is fed to the cathode. When the air reaches the cathode-electrolyte interface, the O_2 molecule dissociates, gains two electrons from cathode and enters the electrolyte.

$$\tfrac{1}{2}O_2 + 2e^- \rightarrow O^{2-} \quad (96)$$

The O^{2-} ion the travels through the electrolyte to the electrolyte-anode interface. Here, the fuel gas (assumed to be hydrogen) gives off electrons to the anode and the ionized hydrogen molecule reacts with the O^{2-} ion forming water.

$$H_2 + O^{2-} \rightarrow H_2O + 2e^- \quad (97)$$

If the two electrodes are connected by an electronic conductor, electrons will flow from the anode to the cathode and a circuit will be created. The total cell reaction is now

$$H_2 + \frac{1}{2}O_2 \rightarrow H_2O \quad (98)$$

The change in Gibbs free energy for a chemical reaction was given in equation (12), in section 2.1. Also, the Nernst equation relates the Gibbs free energy to the electric field ε,

$$\Delta G = -zF\varepsilon \, (99)$$

where z is the valence of the ions transported in the reaction, and F is Faradays constant.
Relating equations (12) and (99) creates equation (100).

$$\varepsilon = \varepsilon^{\circ} + \frac{RT}{nF}\ln\left(\frac{a_C^c a_D^d}{a_A^a a_B^b}\right)(100)$$

In a SOFC, ε° is 0.98 volts at 800°C, and the total cell voltage can be determined as a function of gas pressures.

$$\varepsilon = \varepsilon^{\circ} - \frac{RT}{2F}\ln\left(\frac{p_{H_2} p_{O_2}^{1/2}}{p_{H_2O}^{cathode}}\right)(101)$$

2.5.1.2 SOFC Components

The anode is typically a Ni-YSZ cermet. These materials are fabricated by mixing NiO, and YSZ powders. When this mixture is exposed to a reducing gas, NiO reduces to nickel metal creating a porous cermet. The high surface area, 5-20 m^2/g, and relative catalytic activity of nickel make the reaction kinetics at the anode rapid.

The choice cathode material is dependent on the temperature of operation, however most candidate materials are perovskites with low electrical resistivity. Lanthanum strontium manganites (LSM) and lanthanum calcium manganite (LCM) are commonly used in cells that operate at higher temperatures while lanthanum strontium ferrite (LSF) and lanthanum strontium cobalt ferrite (LSCF) are widely used at lower temperatures.

The role of the electrolyte is to allow fast ionic conduction with minimal electrical conduction and the material that is typically used is yttria stabilized zirconia (YSZ). YSZ conducts oxygen ions due to the large number of oxygen vacancies which form when ZrO_2 is doped with Y_2O_3. The electrolyte is also a physical barrier between the anode and cathode gases. The ionic flux is inversely proportional to the thickness of the electrolyte and thickness minimization is desired. As the thickness is decreased, the requirement for minimizing porosity is increased and processing becomes a key issue.

The voltage produced by an individual cell, less than 1 volt, is not large enough to be useful for most applications. As a result, cells are stacked in series to produce a larger voltage. To produce this stack, cells are connected by an electrically conducting plate, known as the interconnect, current collector, or bipolar plate. The interconnect is in a particularly aggressive environment because it is simultaneously exposed to the anode and cathode gases. The requirements that the interconnect must fulfill are:

- Mechanical stability
- Electrical conductivity
- Easy of Fabrication
- Low Cost
- CTE Match
- Chemical stability

When SOFC stacks were first constructed, platinum was used as an interconnect but due to the high cost of platinum this material could not be used in commercial devices and alternatives were sought after. In the 1970's $LaCrO_3$ was used. These perovskite ceramics are good conductors and are substantially less expensive than platinum. As new materials and new processing capabilities were developed that allowed the operating temperature of SOFC's to function below 1000°C, metallic interconnects became an attractive materials alternative that could reduce the overall cell cost. With respect to ceramic interconnects, metals have better mechanical properties, lower cost, are easier to fabricate, and have better electrical conductivity. However, under operating conditions most metals are oxidized and the exceptions are expensive noble metals. The oxide scales that form on metals are much more resistive than the metals themselves and a key parameter is the amount of resistance an oxide scale will produce throughout the life of the fuel cell.

Area specific resistivity (ASR), is the measure of the resistive contribution that the scale makes to the cell. The ASR is defined in equation (102),

$$ASR = RA = \rho L \quad (102)$$

where R is the resistance in Ohms, A is area, ρ is resistivity in Ohm-cm, and L is length, or thickness. As shown in equation (102), the two factors that determine the ASR are the resistivity and the scale thickness. The protective scales that grow the slowest on engineering alloys, therefore having the smallest L are alumina and silica. However, these materials have very high values of ρ as shown in table 3. On the other hand, the thermally grown scales that have relatively low resistivities, such as FeO, and CoO, have very high growth rates. Two oxides that are a compromise of these two properties are NiO and Cr_2O_3 with NiO having lower resistivity and Cr_2O_3 having a slower growth rate.

Table 3. Electrical resistivities of bulk oxides and growth rates of oxides at 800°C

Oxide	**Resistivity ρ Ω-cm**	**k_p' (cm^2/s)**	**scale thickness-1000Hr µm**	**ASR after 1000 Hrs Ω-cm^2**
Al_2O_3	10^7-10^{10}	$3x10^{-16}$-$3x10^{-14}$	0.5	400-5000
Cr_2O_3	33-1000	10^{-12}-10^{-13}	10-50	0.02-0.46
NiO	1-50	$2\text{-}7x10^{-12}$	40-60	0.01-0.21
CoO	0.1	$3x10^{-10}$	490	0.01
FeO	0.01	$7x10^{-5}$	230000	0.23

The majority of investigations of interconnect materials have been focused on chromia forming alloys, particularly, ferritic stainless steels. These materials have desirable electrical properties but they have the additional complication of oxide vaporization. In dry environments CrO_3, is the predominant vapor species, and in wet environments it is $CrO(OH)_2$. Both of these vapor species reduce the efficiency of the cell by reacting with the cathode.

2.6 MECHANICAL STABILITY

2.6.1 Chemically Driven Cavity Growth

There are many systems in which an element diffuses in the alloy and reacts with a constituent to form a molecule which precipitates as gas bubble. Shewmon has termed this phenomenon chemically driven cavity growth, CDCG.[43] One example of CDCG occurs when hydrogen pressure vessels are constructed of carbon steels.[44, 45] In these systems, hydrogen dissolves into the steel according to Sievert's law and then reacts with the dissolved carbon in the steel to form methane. If the pressure of the methane exceeds a threshold value, methane bubbles nucleate and grow, drastically reducing the ductility of the steel. Other examples of this phenomenon is the formation of water vapor in oxygen bearing copper[46] that is exposed to hydrogen and the formation carbon dioxide bubbles in carbon bearing nickel that is exposed to oxygen.[47]

Fuel cell interconnects are also susceptible to this phenomenon. An interconnect is simultaneously exposed to hydrogen from the fuel gas and oxygen from the oxidant gas. If sufficient concentrations of hydrogen and oxygen dissolve into the interconnect there is a strong chemical driving force for the formation of water vapor. If the pressure of water vapor is great enough, cavities will form.

In an interconnect, cavity formation is not limited by an initial amount of a species (i.e. the carbon concentration in steels limiting methane formation). Both reactants are supplied continuously and as a result, the maximum water vapor pressure is only a function of solubility of each species.

2.6.2 The Driving Force for Cavity Nucleation

In the analysis of what conditions are necessary to facilitate water vapor induced degradation in interconnect alloys, two factors must be considered: the driving force of water nucleation, and the rate determining process which governs the bubble growth.

The driving force for water vapor nucleation is the water vapor pressure. This value can be calculated by finding the free energy of formation for water at 800°C.

$$H_2 + \tfrac{1}{2}O_2 = H_2O \quad (103)$$

$$K = \exp\left(\frac{-\Delta G^\circ}{RT}\right) = \frac{a_{H_2O}}{a_{H_2} a_{O_2}^{1/2}} = \frac{f_{H_2O}}{p_{H_2} p_{O_2}^{1/2}} \quad (104)$$

The hydrogen and oxygen activity can be assumed to be equal to their respective partial pressures to a good approximation, due to their low concentrations. However, due to the large equilibrium constant, the activity of water vapor can be very large, and therefore the activity is more accurately defined as the fugacity, as opposed to the pressure. The fugacity of water vapor can be calculated throughout the interconnect using equation (105) where S_O and S_H are the Sievert's Law constants.

$$p_{H2} p_{O2}^{1/2} K = \left(\frac{[H]}{S_H}\right)^2 \frac{[O]}{S_O} K = f_{H_2O} \quad (105)$$

The water vapor pressure is the driving force for cavity nucleation and growth, and therefore the fugacity-pressure relationship must be determined. However, this relationship is not known under present conditions of high temperature and pressure. At low fugacities, the approximation that pressure is equal to the fugacity is reasonable, but at higher fugacities this is not the case.

Odette and Vagarali[48] have analyzed the fugacity-pressure relationship for methane formed in hydrogen attacked carbon steel using a statistical mechanical-based model. In this analysis, the methane pressure was found to be a fraction of the fugacity, with the fugacity-pressure ratio decreasing with increasing pressure. A similar approach could be applied to water under the given conditions but has not been performed due to the complexity of the analysis.

2.6.3 Nucleation

Once the driving force for nucleation has been determined, the manner in which nucleation occurs must be considered. Under conditions of high driving force or when a material with few defects is used, homogeneous nucleation will predominate. The rate of nucleation will be a function of the probability that a cavity with a critical radius can form and the frequency at which a vacancy will move across the critical cavity nucleus, causing growth. On the other hand, when the driving force for nucleation is small or the material contains defects, heterogeneous nucleation will occur Under this circumstances the number of nucleation sites is fixed by the defect density.

2.6.3.1 Homogeneous nucleation

The change in free energy associated with the growth of a water vapor bubble can be expressed as equation (106) with the assumption that the bubbles are spherical[44].

$$\Delta G = -\frac{4}{3}\pi r^3 P + 4\pi R^2 \gamma \text{ (106)}$$

The critical radius *r*, the radius at which any growth will decrease the total free energy can be found by evaluating $d\Delta G/dr=0$.

$$r = \frac{2\gamma}{P} \text{ (107)}$$

The free energy of nucleation ΔG*, which is the free energy change produced by nucleating a cavity with radius *r* is found by substituting equation (107) in to equation (106).

$$\Delta G^* = \frac{16\pi\gamma^3}{3P^2} \text{ (108)}$$

Next, the nucleation rate of cavities can be calculated. The nucleation rate is a function of the number of nucleation sites, the probability that nucleation will occur at that sites, and frequency that a vacancy will move to the critical nucleus.

The number of sites ρ_N must be estimated from the microstructure of the starting material. A nucleation site will be postulated to be a multigrain boundary intersection. The probability of critical nuclei formation can be calculated using the free energy of nuclei formation[44].

$$\xi = \exp\left(\frac{-\Delta G^*}{kT}\right) (109)$$

Finally, the frequency of vacancies moving to the critical nuclei Γ can be calculated in terms of the cavity's surface area $4\pi r^2$ and the frequency of atoms moving away from the surface D/Ω.

$$\dot{N} = \frac{\pi\gamma^2 D\rho_N}{\Omega P^2}\exp\left(\frac{-\Delta G^*}{kT}\right) = \frac{\pi\gamma^2 D\rho_N}{\Omega P^2}\exp\left(\frac{-16\pi\gamma^3}{3P^2kT}\right) (110)$$

2.6.3.2 Defect Induced Nucleation

If there are a large number of defects in the alloy, nucleation can occur heterogeneously at defects. It is assumed that number of critical defects is fixed and that subcritical defects do not grow into critical defects. As a result, the number of nucleation sites is fixed[44, 49].

2.6.4 Cavity Growth

Once the cavities have nucleated, certain processes must occur in order for growth to proceed. These processes are[44]:

I) Movement of H to the cavity
II) Movement of O to the cavity
III) $\underline{H}+\underline{O}\rightarrow H_2O$
IV) Movement of metal from the cavity

In most materials the diffusion of hydrogen and oxygen into the metal is much more rapid than the self diffusion of metal. Therefore, the rate of growth will be controlled by the diffusion of metal away from the cavity. In addition, the grain boundary diffusivity is generally substantially greater than the lattice diffusivity. This is not necessarily the case for silver, but can be used as an approximation.

If grain boundary diffusion is the rate controlling step, then the growth process will be similar to Coble creep, a process that is controlled by the rate at which atoms can rearrange themselves to accommodate stress by way of grain boundary diffusion.

Following Raj and Ashby[49] and Raj et al[50]., it is assumed that the bubble nucleation sites are uniformly distributed at distance 2*L* apart. The bubbles are also assumed to be spherical with an internal pressure *P*. In order to determine the rate at which the bubbles grow, the diffusion potential acting on the bubble must be calculated.

The excess chemical potential of the atoms in the boundary relative to the stress free state is

$$\Delta\mu = -P\Omega \quad (111)$$

where Ω is the atomic volume. The transport equation governing grain boundary diffusion under this potential gradient is then equation (112).

$$j_B = \frac{-D_B}{kT\Omega}\frac{\partial\Delta\mu}{\partial R} \quad (112)$$

Under steady state conditions, the grain boundary flux will be a constant, β which is equal to the number of atoms removed when the boundary has a thickness δ.

$$\frac{\partial j_B}{\partial R} = \beta \quad (113)$$

Combining equations (112) and (113) produces equation (114).

$$\frac{\partial^2\Delta\mu}{\partial R^2} = \frac{\beta kT\Omega}{D_B} \quad (114)$$

This equation can be solved using the boundary conditions. First, at the mid point between two bubbles *L*, the diffusion potential is at a minimum.

$$\frac{\partial\Delta\mu}{\partial r} = 0 \text{ at } R = L \quad (115)$$

Second, the diffusion potential at the cavity surface *r* is equal to the internal pressure minus the surface energy increase that results from the surface curvature.

$$\Delta\mu = \Omega\left(P - \frac{2\gamma}{r}\right) \text{ at } R=r \; (116)$$

Double integration of equation (114) produces an expression which describes the potential as a function distance R, $\Delta\mu(R)$.

$$\Delta\mu(R) = \frac{-\beta kT\Omega}{4D_B}\left(R^2 - r^2\right) - \frac{\beta kT\Omega L^2}{2D_B}\ln\left(\frac{r}{R}\right) + \Omega\left(P - \frac{2\gamma}{r}\right) (117)$$

In this expression, the constant β which is equal to the number of atoms removed when the boundary has a thickness δ is expressed as equation (118) where δ is the grain boundary width, and *dv/dt* is the rate of bubble growth.[45]

$$\beta = \frac{{}^{dv}\!/_{dt}}{\delta\pi\left(L^2 - R^2\right)} (118)$$

Further, mechanical equilibrium must be maintained such that the force produced by the internal pressure and the surface energy must be equal to force that pushes atoms out through the grain boundary.[50] This is expressed as equation (119).

$$\left(P - \frac{2\gamma}{r}\right)\pi r^2 = \int_r^L \frac{\Delta\mu}{\Omega} 2\pi R^2 dR \; (119)$$

The solution to equation (119) then becomes equation (120) which describes the rate of bubble growth where *X=R/L*.

$$\frac{dV}{dt} = \frac{2\pi D_b \delta\Omega}{kT}\left(P - \frac{2\gamma}{r}\right)\frac{\left(1 - X^2\right)^2}{X^2\left(1 - \frac{X^2}{4}\right) - \frac{3}{4} + \ln\frac{1}{X}} (120)$$

2.7 EXPERIMENTAL METHODS

2.7.1 The testing of interconnects under simulated Fuel Cell Conditions

It is important to test materials in a laboratory in a manner that will simulate the environment that they will be exposed to in service. To this end, interconnect materials are typically tested in three different atmospheres: simulated cathode gas (SCG), simulated anode gas (SAG), and under dual atmospheric conditions (DA). The cathode environment can be simulated by an exposure to air in the temperature range 700-900°C. This is accomplished by enclosing a specimen in a reaction chamber, flowing the desired gas mixture through the chamber and using a furnace to fix the desired temperature. The anode gas environment can be done in a similar fashion. Actual anode gases are typically, pure hydrogen, or mixtures of hydrogen with water vapor, methane, carbon monoxide or carbon dioxide. Due to the explosion risk that hydrogen poses, a simulated anode gas atmosphere of Ar-4%H_2-10%H_2O was used. The oxygen partial pressure of this gas mixture at 800°C is $p_{O_2} = 2.7x10^{-18}$ atm. An actual fuel cell may use a gas mixture of 97%H_2-3%H_2O. This gas mixture has an oxygen partial pressure of $p_{O_2} = 4.4x10^{-22}$ atm. In the third test condition, the dual atmospheric exposure, the interconnect is simultaneously exposed to a SCG on one side and a SAG on the other. It has been shown that some materials can behave differently when simultaneously exposed to both the SCG, and the SAG, as opposed to exposure to a single environment. Anomalous effects include the nucleation of water vapor bubbles[7] in the alloy and changes in the selective oxidation[6] on the cathode side.

2.7.2 Determination of Reaction Rates

Measuring the rate of reaction that occurs between the interconnect and its environment is an important tool that can be used to understand how the interconnect will deteriorate during operation. The primary cause of the deterioration of the electrical properties of the interconnect is the formation of oxide scales and, therefore, determining the oxidation rate is necessary in the understanding of the degradation of the interconnect.

The rate of oxidation can be found by measuring the change in mass of the interconnect due to the incorporation of oxygen. This is typically done by measuring the mass gain normalized with respect to surface area, as a function of time. As previously described, the change in mass can allow the parabolic rate constant, k'' $(g^2cm^4s^{-1})$ to be determined.

The parabolic rate constant, k'' can be determined by measuring the mass change continuously or discontinuously. Discontinuous measurement involves determining the surface area of the specimen and its weight before and after exposure. This is a rather simple test, and if multiple tests are performed, the rate constant can be determined by finding the slope of the $(\Delta m/A)^2$ *vs.* t plot. Continuous mass change measurements can be made using a method called thermogravimetric analysis (TGA). TGA is performed by suspending the specimen from a microbalance. The specimen is then brought into the hot zone of a furnace and the mass change that results from oxidation is recorded continuously. TGA is the preferred test because it shows if any mass loss occur during the test.

Error is generated from uncertainty in surface area, and this can be minimized using specimens that have large surface areas. In addition, most microbalances are only accurate to approximately $0.01mg$. By increasing the surface area, the total mass gain is increased which decreases the total error generated by the uncertainty of the balance.

2.7.3 Electrical Degradation: Area Specific Resistance

A popular method for determining the resistivity of materials is a test known as “the four-point probe”. In this technique, a known current is passed across one side of a specimen of known cross-sectional area. Wires on the other side of the specimen collect the current and the voltage difference between the two wires in measured. Using Ohm’s law, equation (121), the resistance R can be calculated.

$$V = IR \quad (121)$$

Another constant ρ, known as the resistivity is an intrinsic materials property and it can be determined when the resistance is known, using equation (122)

$$R = \frac{\rho L}{A} \quad (122)$$

where R is the resistance in Ohms (Ω), A is area (cm^2), ρ is resistivity (Ω-cm), and L is length (cm), or thickness. For many years, the two-point probe has been used to measure the resistivity of metals and ceramics, however, the electrical properties of thermally grown oxide scales were first investigated by Park and Natesen in 1990[51]. This is a useful test in the evaluation of interconnects and has since been used by many investigators. In the evaluating of interconnects, the electrical property of interest is the total resistance that the interconnect contributes to the system. This is found by normalizing the resistance measured using the two-point probe with respect to the cross-sectional area of the electrical contact. This value is the ASR, previously described.

$$ASR = RA = \rho L \quad (123)$$

This allows the ASR to be determined without knowledge of the resistivity of the oxide or its thickness.

Experimental error can occur in this test as a result of a number of factors. First, the ASR is directly proportional to the cross-sectional area. Electrodes such as platinum paste may cover a certain area that is easy to measure but it is difficult to determine what fraction of the pasted region makes electrical contact to the surface of the specimen. The surfaces of thermally grown oxides are often tortuous on a submicron scale and this may hinder uniform contact. Secondly, interfacial energy barriers exist at many interfaces. These barriers will increase the resistance in the circuit. Deviations from ohmic behavior are greatest at large currents, therefore, interfacial resistance can be minimized when small currents are applied.

3.0 PROBLEM STATEMENT

Due to the rapid degradation of cell performance that results when chromia evaporates from many leading candidate interconnect materials, there is desire to develop an interconnect with suitable properties, that does not contain chromium. The goal of this research is to evaluate the performance of nickel and nickel alloys as interconnect materials for solid oxide fuel cells. This evaluation will focus on three areas. First, the stability of the candidate materials under dual atmospheric conditions will be evaluated by simultaneous exposure to simulated anode and cathode gases. Second, the rate of oxidation will be measured using thermogravimetric analysis. Lastly, the electrical degradation of oxidized coupons will be measured using a two-point probe conductivity test. Thermogravimatric analysis along with the conductivity tests will allow the degree of degradation as a function of time to be determined. Comparisons of the investigated alloys with other candidate materials are made.

4.0 EXPERIMENTAL PROCEDURE

4.1 MATERIALS

4.1.1 Nickel

The baseline material of this investigation is high purity nickel (99.999% pure Goodfellow Ltd). This material was received as 1mm thick sheet and was cut into coupons of dimensions 10x15mm. In addition, Ni200 a lower purity grade of nickel was studied, in the form of tubes.

4.1.2 Nickel Copper Alloys

Two nickel copper alloys were studied; a fabricated Ni-5wt%Cu alloy, and a commercial grade Monel alloy. A 100g button of the Ni-5wt%Cu alloy was arc melted from high purity nickel and copper pieces. The arc melted alloy was annealed in Ar-4%H_2 gas mixture at 1000°C for 24 hours. Following the initial anneal, the alloy was cold rolled, and annealed for 5 hours at 1000°C in an Ar-4%H_2 atmosphere. The resulting microstructure consisted of equiaxed grains with an average diameter of 20μm. The second alloy, Monel, had a nominal composition of Ni-33wt%Cu-2wt%Fe, with a purity level of 99%. This alloy was received as a 2mm thick sheet.

4.1.3 Silver

Silver, (99.99% Goodfellow) was received as 1mm thick sheet and as a powder. The average grain size of the as-received sheet was roughly 100μm.

4.1.4 Silver-Nickel Composites

A nickel-silver composite was fabricated by drilling a hole in high purity nickel sheet 400μm in diameter and 500μm in depth. Silver powder was placed in the hole, partially filling the hole, and then heated to 975°C, approximately 15°C above the melting point of silver, in Ar-4%H_2. Next, more silver powder was added and the composite was reheated. This process was repeated until the hole was filled and the silver extended approximately 100μm above the surface.

4.1.5 Pulsed Laser Deposition of Ceria

Pulsed laser deposition (PLD) was used to deposit ceria onto nickel and Ni-5Cu. Prior to deposition, the alloys were ground with diamond polishing wheels to 1200 grit, and then fine polished at 9 and 3μm with a diamond suspension and then with a submicron colloidal silica suspension. The polished samples were ultrasonically cleaned in soapy water, water, acetone and isopropanol.

During deposition the specimen was held in a vacuum chamber at $1x10^{-9}$ atm. A KBr laser was used to at a frequency of 10Hz and energy density of .8-.1.5J/cm^2. The deposition rate under this condition is in the range of 1nm/s. Ceria was deposited for two minutes. Interference patterns produced by the coating indicated that the there a thickness gradient. To minimize the variation in thickness, the specimen was rotated 180° and then a second deposition was performed. The average thickness of the ceria coating was 100-200nm. A schematic of the experimental setup is shown in Figure 9.

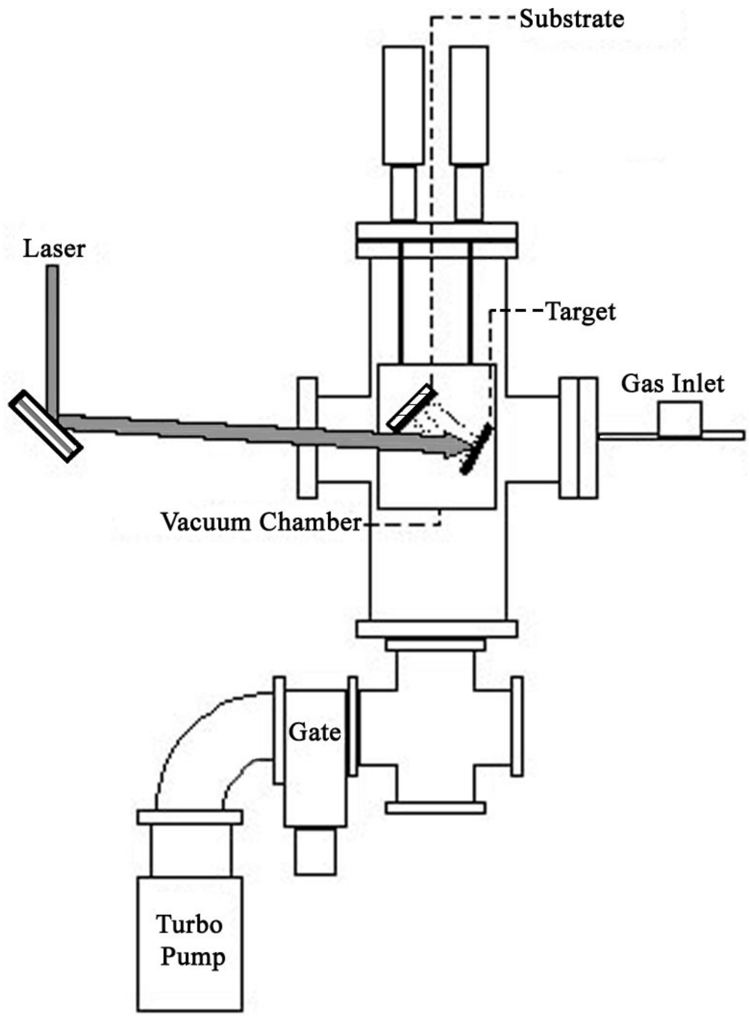

Figure 9. Schematic of PLD experimental setup

4.2 HIGH TEMPERATURE EXPOSURES

4.2.1 Simulated Cathode Gas Exposures

Materials tested in the SCG environment where cut into coupons with the nominal dimensions 15x10x1mm. The coupons were then polished to a 600 grit finish using SiC grinding papers. The ground samples were subsequently ultrasonically cleaned in soapy water, water, acetone and finally isopropanol. The exposure temperatures were fixed using resistance heated furnaces and were monitored by external thermocouples. Silica and mullite reaction chambers where used to enclose the experimental environment and bottled dry air was passed through these chambers to fix the gas composition. Specimens were suspended in the reaction chamber using platinum wires.

TGA tests where performed in a similar apparatus and a Cahn C-1000 microbalance was used to monitor the mass changes. Figure 10 shows the TGA experimental set up. TGA is a method of measuring continuous mass change as a function of time. The experimental apparatus consists of a furnace, a reaction chamber, a microbalance and a computer.

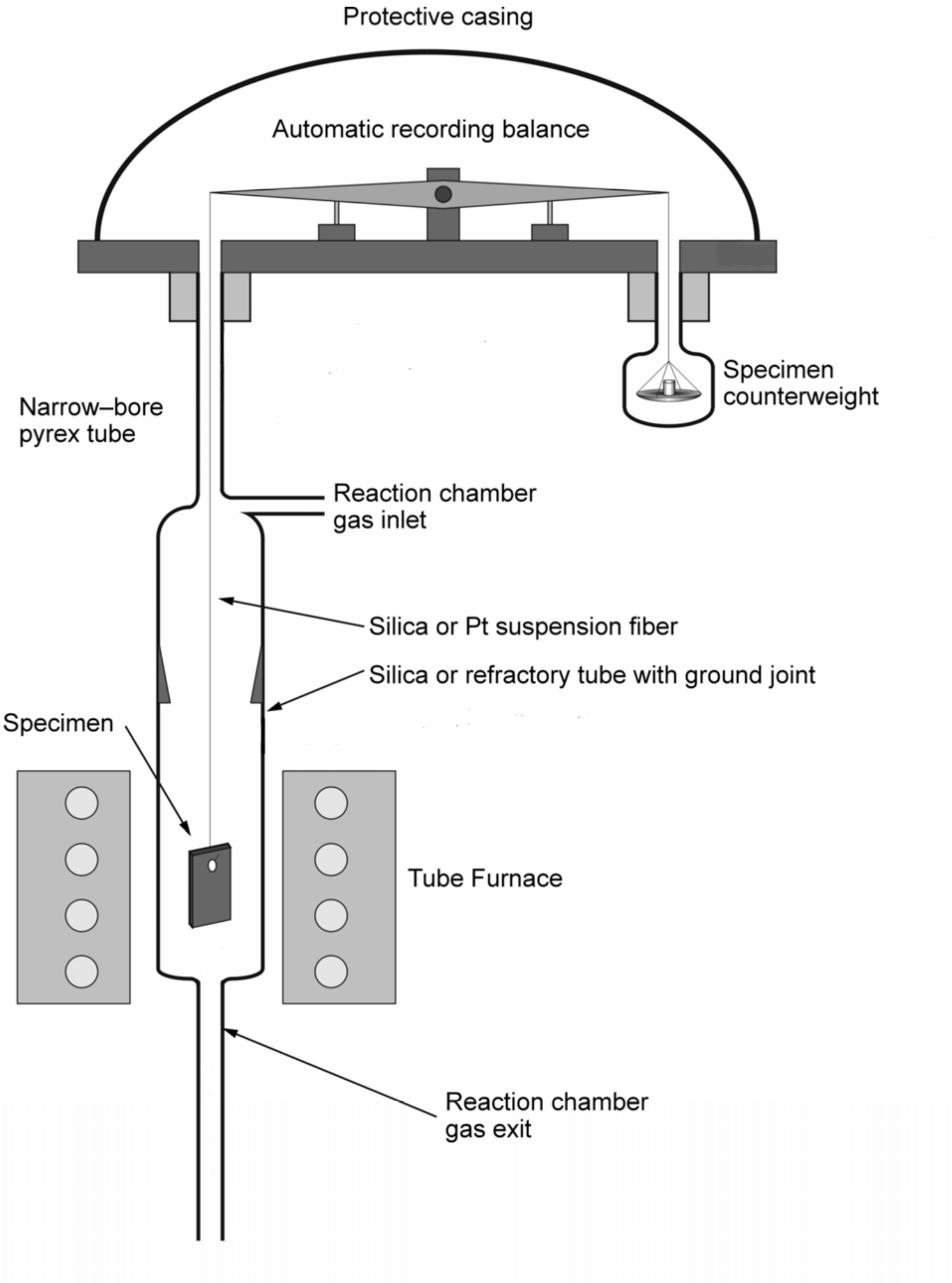

Figure 10. Schematic of TGA apparatus[9]

The microbalance used is the Cahn 1000 which operates as a force-to-current converter. The balance is held level by a torque motor and when a specimen is suspended from the balance the motor applies a force to counter act the weight of the sample. The current necessary to counteract the weight of the specimen is outputted to a computer where it is recorded every second using Omega PersonalDAQ software. The change in current is calibrated to determine the change in mass and an accuracy of 0.1mg was achieved

To start a test, a specimen was suspended from the microbalance on a platinum wire in the reaction chamber. Data was recorded for ten minutes to obtain a zero-point mass measurement and then the furnace was started and allowed to reach the desired test temperature. One hour after the start of recording data, the sample was lowered into the furnace. The specimen was raised from the furnace after the desired time had elapsed.

4.2.2 Dual Atmospheric Exposures

Dual atmospheric tests where performed in two different experimental configurations, with one apparatus being designed to test sheet specimens, and the other being designed to test tube specimens. The dual atmospheric tube apparatus is shown in Figure 11a. In this test, two metallic tubes were fixed in a silica reaction chamber. The SCG was passed through the reaction chamber, while the SAG, Ar-10%H_2O, 4%H_2 was passed through the center of one of the metallic tubes. As a control, dry air was passed through the center of the second tube. A temperature gradient existed across the hot zone of the furnace and this temperature profile was determined. Knowledge of the temperature gradient allowed multiple exposure conditions to be tested in a single run.

A schematic of the second dual atmospheric test configuration is shown is in Figure 11b. Mica seals were used to prevent the mixing of the SCG and SAG.

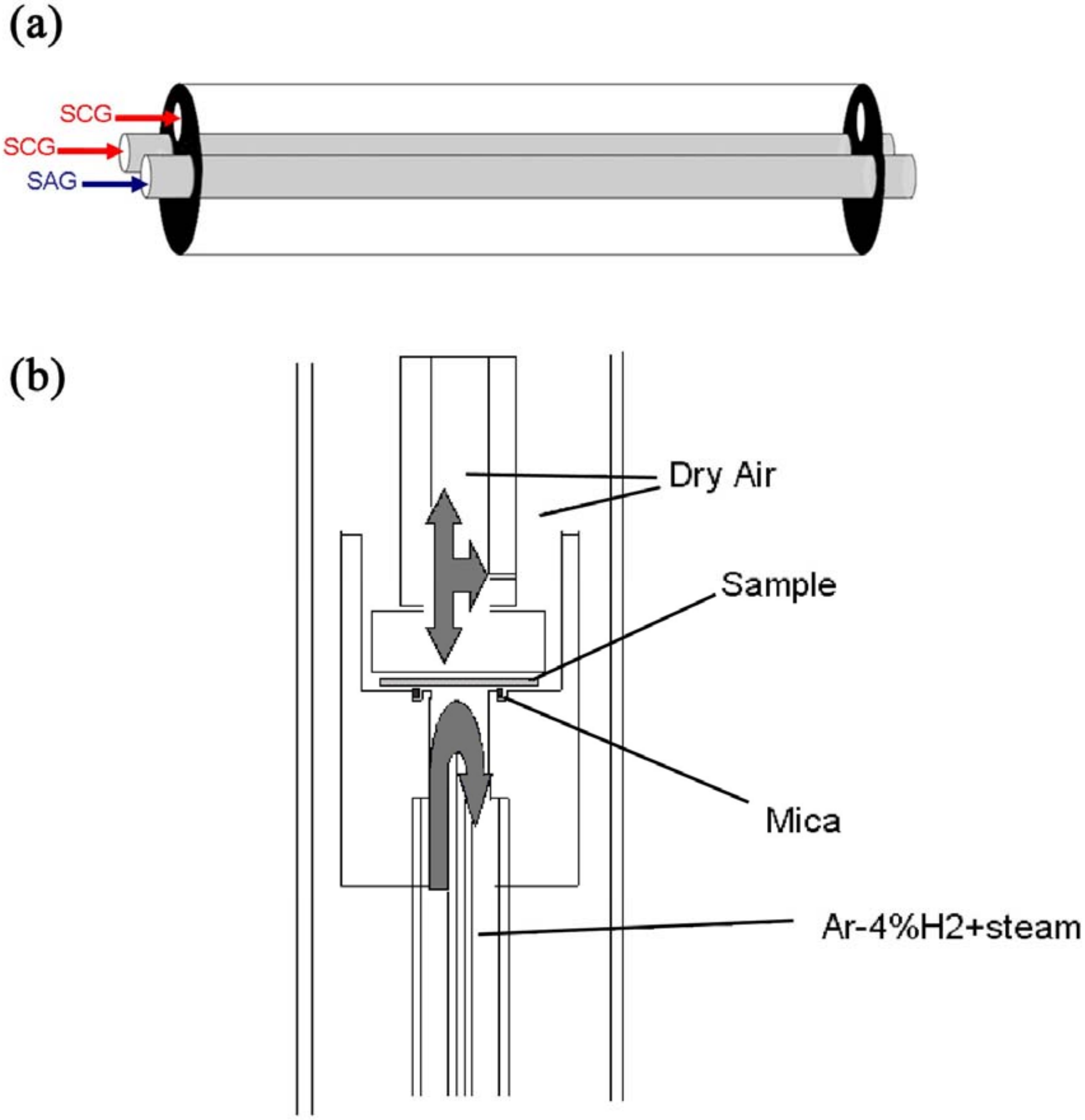

Figure 11. (a) tubular and (b) sheet dual atmospheric apparati[51]

4.3 AREA SPECIFIC RESISTANCE

The ASR was measured using a 4-point probe test. The specimens used for investigation were pre-oxidized coupons. Electrical contact was made with the coupons following oxidation using platinum paste (SPI No.1090120). The paste was painted in 6x6mm squares on both sides of the specimen. Following application of the platinum paste, the specimens were exposed at 600°C for one hour in dry air to drive off the binder in the paste, and to sinter the platinum particles. Platinum paste was then reapplied to the specimen, which was followed by another annealing step at 600°C for one hour. The surfaces of the specimens were then examined using an optical microscope or a scanning electron microscope to insure that the paste covered the desired area.

Platinum sheets of thickness 0.5mm where used to connect to the platinum paste and platinum wires were arc welded to the sheets. The specimen and the platinum sheets where placed in a ceramic holder. Screws were used to apply pressure to ceramic sheets which pressed the platinum foil against the platinum pasted. The experimental set up is shown in Figure 12.

Current was applied using a Jandel Model RM2 current source, at a fixed amperage between 1000-10,000μA. The voltage drop across the specimen was also measured by the Keithely 2001 multimeter. The specimen was placed in a holder and the specimen holder was placed into a furnace and the temperature was raised to the exposure temperature. Once at temperature, voltage measurements were taken at 1000, 5000, and 10,000 μA. Measurements were repeated until the measured voltage remained constant. A schematic of the 4-point probe is shown in Figure 13. It can be seen that the oxide grown on both sides of the coupon contributes to the total resistance. The measured values were divided by two in order to determine the resistive contribution of the oxide scale grown on one side. In operation, a nickel interconnect would oxidize on the cathode side, but not the anode side, and therefore the resistance that is produced by one scale is all that should be taken into account.

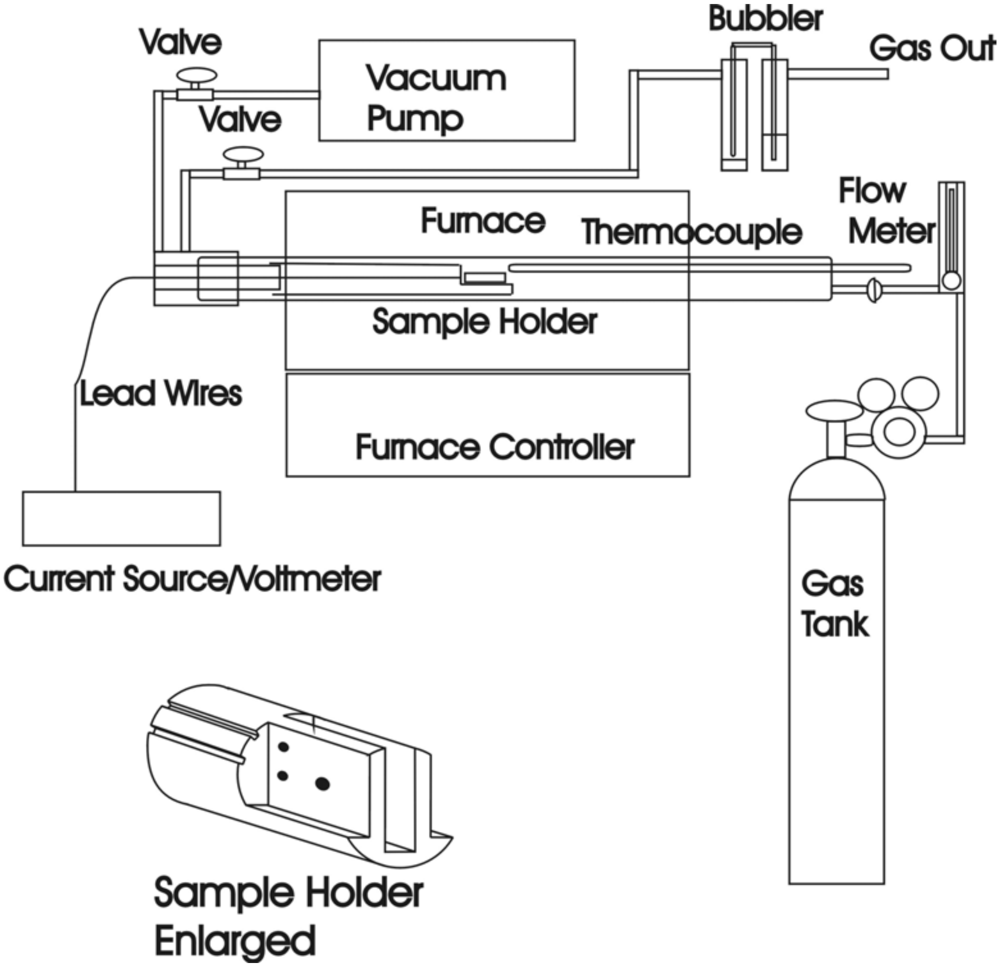

Figure 12. Schematic of ASR experimental setup [52]

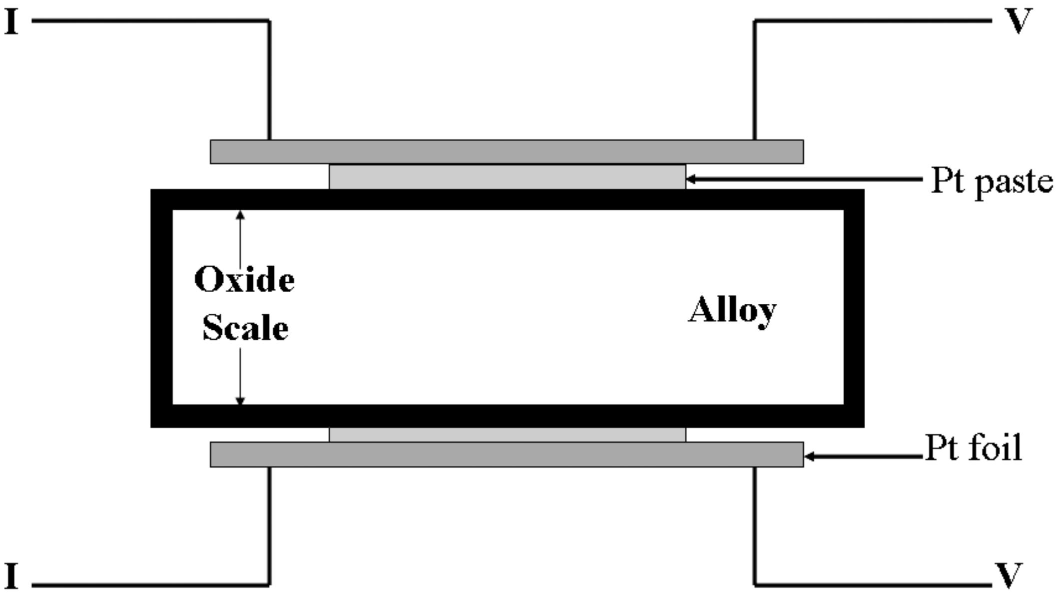

Figure 13. Schematic of the four-point probe conductivity apparatus

4.4 MICROSCOPY AND ANALYTICAL

Qualitative analysis of the surfaces and cross-sections of exposed materials was performed using optical and scanning electron microscopy. Low magnification analysis was performed using reflected light microscopy and high magnification microscopy was performed using a scanning electron microscope (SEM). The SEM was a Phillips XL30 FEG (field emission gun). This SEM was equipped with backscatter and secondary electron detectors for imaging and an X-ray detector used for energy dispersive spectroscopy (EDS).

4.5 FUEL CELL TESTS

Test alloys were used in fuel cell tests performed at the National Energy Technology Laboratory, in Morgantown West Virginia. The schematic of cell used is shown in Figure 14. In these tests the interconnect was part of the circuit of a single fuel cell. The cells used were anode supported cells manufactured at the University of Utah. The anode was a Ni/YSZ cermet approximately 1 mm thick and also containing a Ni/YSZ interlay approximately 50µm thick. The electrolyte was YSZ approximately 20µm thick. The cathode was 50µm thick LSM with a 50 µm thick YSZ/LSM interlayer. Both interlayers were more porous than either the cathode or anode.

The above assembly was placed in a tube furnace and heated from room temperature to 800°C at a rate of 6.5 degrees per minute. The cells were then exposed to a 10% hydrogen in N_2 mixture on the anode side, with a total flow rate of 6.5cm^3/s. Gases on both the anode and cathode side were fed to the cell through a coaxial 0.6cm diameter feed tube, and the exhaust was removed through the outer 2.5cm diameter support tube. The cathode had 17cm^3/s air flow at all times. After two hours under these conditions, the anode gas was changed to 3% H_2O in 97% H_2 at 6.5cm^3/s. The cell was then set to 0.7 volts using an Agilent N3303A load box. The voltage and current signals were then collected as a function of time using Labview.

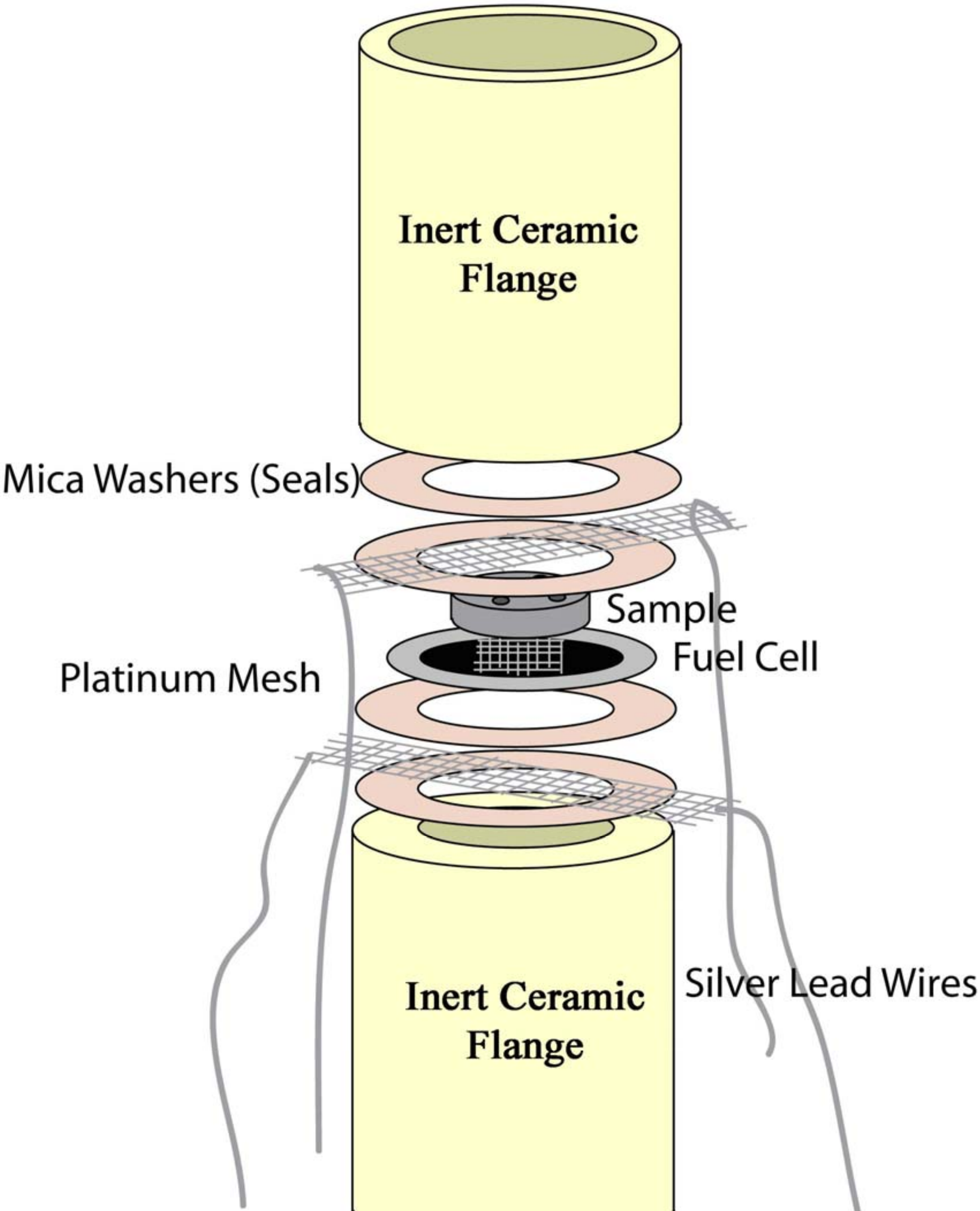

Figure 14. Schematic of test cell [52]

5.0 RESULTS AND DISCUSSION

5.1 KINETIC MEASUREMENTS

5.1.1 ThermoGravometric Analysis

TGA was used to measure the growth rate of NiO on nickel and Ni-5Cu. Isothermal exposures were performed at 700°C, 800°C, and 900°C for 100 hours in dry air. Results are shown in Figure 15a for the oxidation of nickel and in Figure 15b for Ni-5Cu. At all temperatures, an initial rapid oxidation period occurs, lasting between one and five hours, which was followed by parabolic growth. Haugsrud, has pointed out that there are three primary factors governing the growth NiO; lattice diffusion, short circuit diffusion, and grain growth.[53] If grain boundary diffusion makes a significant contributes to the overall growth rate, then the sub-parabolic kinetics can be explained by grain grow decreasing the grain boundary volume.

The calculated parabolic rate constants are presented in an Arrhenius plot in Figure 16. The activation energy for oxidation of nickel was determined to be 131.**7** ± 41.1kJ/mol, in the temperature range 700-900°C. The large degree of uncertainty is most likely the result of a change in the mechanism which controls the growth rate. There is relatively good agreement in the literature for the activation energy for nickel oxidation above 1000°C with values in the range 200-250kJ.[54] This corresponds well to the activation energy for bulk diffusion in NiO calculated by Atkinson and Taylor to 247kJ/mol.[54] At temperatures below 800°C the activation energy for nickel oxidation was found to be in the range 80-160kJ/mol[53], while the activation energy for grain boundary diffusion of Ni in NiO was found to be 172.5 kJ/mol[22]. This correspondence has supported grain boundary diffusion as the mechanism which controls NiO growth at low temperatures[53] but there is still some disagreement[20]. In the intermediate temperature region in which the oxidation kinetics are affected by three competing processes; bulk diffusion, grain boundary diffusion and grain growth and the interpretation of activation energy is not straightforward.

The growth rate of NiO on Ni-5Cu is slightly slower than on pure Ni although the differences in rate constants are within the uncertainty of the measurement. Whittle and Wood[55] found that a Ni-20Cu alloy oxidized faster than pure nickel, while Haugsrud[56] found that the Ni-20Cu alloy oxidized more slowly than pure nickel.

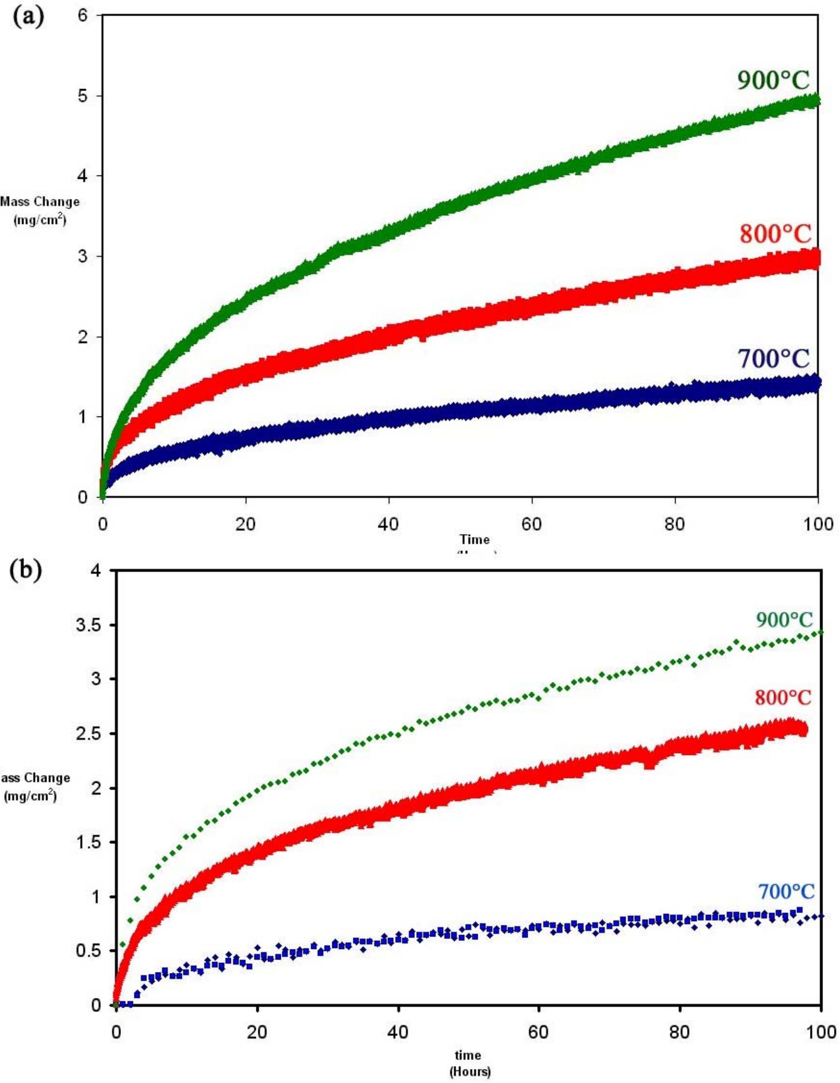

Figure 15. TGA results of (a) nickel and (b) Ni-5Cu exposed in air at 700, 800, and 900°C

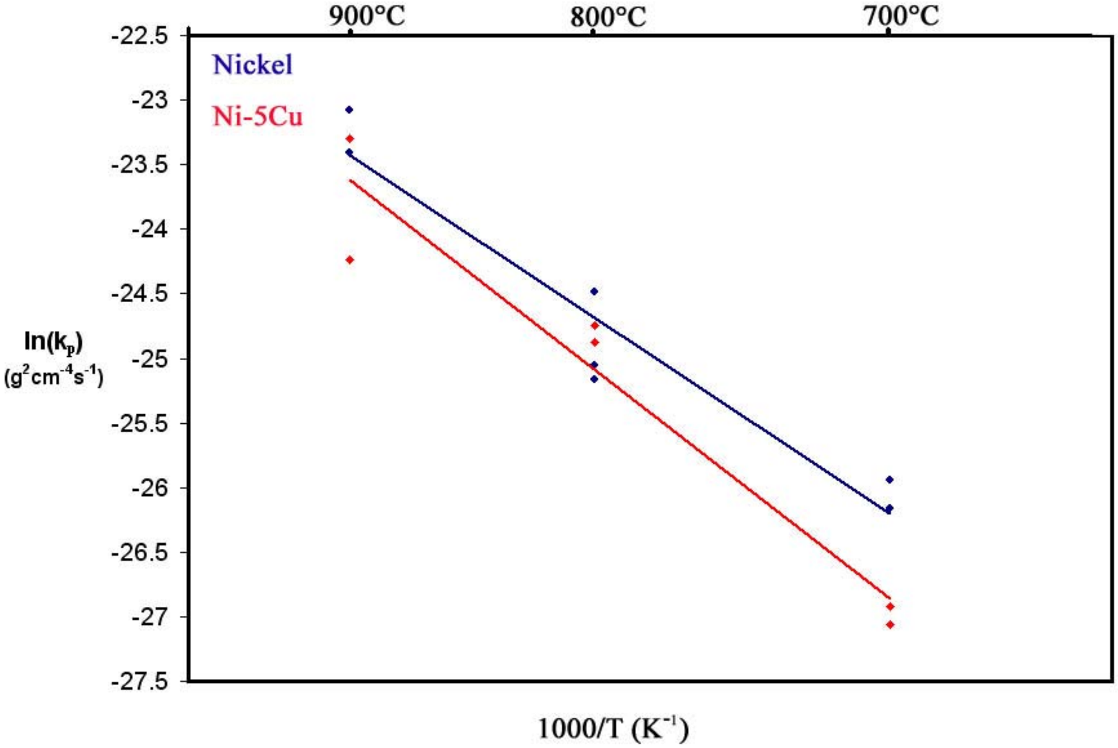

Figure 16. Arrhenius plot for the oxidation of nickel and Ni-5Cu between 700-900°C

5.1.2 Discontinuous mass change measurements

Discontinuous mass change measurements were made for times from 0.25-500 hours. This data is plotted in Figure 17 along with the data from two TGA tests. Each of the data points in the series labeled "individual mass change" comes from a separate specimen and is not the mass change of a single specimen under cyclic exposure. The results of these tests are in general agreement with the continuous mass change data but there is scatter. The scatter is most likely the result of exposure temperature variations. The nickel used for all tests is from the same batch and the same polishing and cleaning technique was used for all of the specimens. The initial microstructure should be similar for all specimen but microstructural variations may exist which may cause variations in the oxide growth rate, resulting scatter in the data.

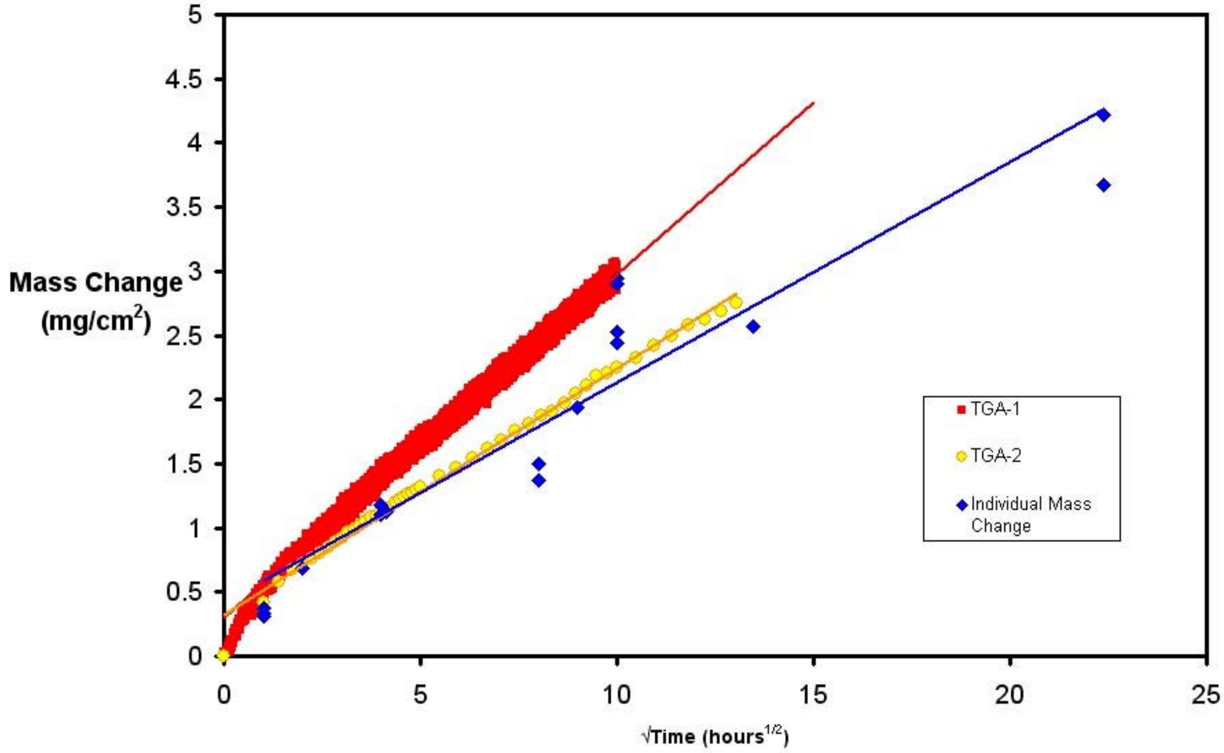

Figure 17. Mass change of Ni at 800°C from TGA tests and discontinuous mass change data

5.2 MICROSTRUCTURE

5.2.1 Oxidized Nickel

The oxide surface has a ridge morphology as shown in Figure 18. This morphology was observed on all specimens exposed for times between 15 minutes and 500 hours. The thickness of the ridges increases with exposure time from 100-250nm at 15 minutes to 400-600nm at 500 hours.

In cross-section, there is some porosity but the scale appears to be a single layer. This is shown in Figure 19.

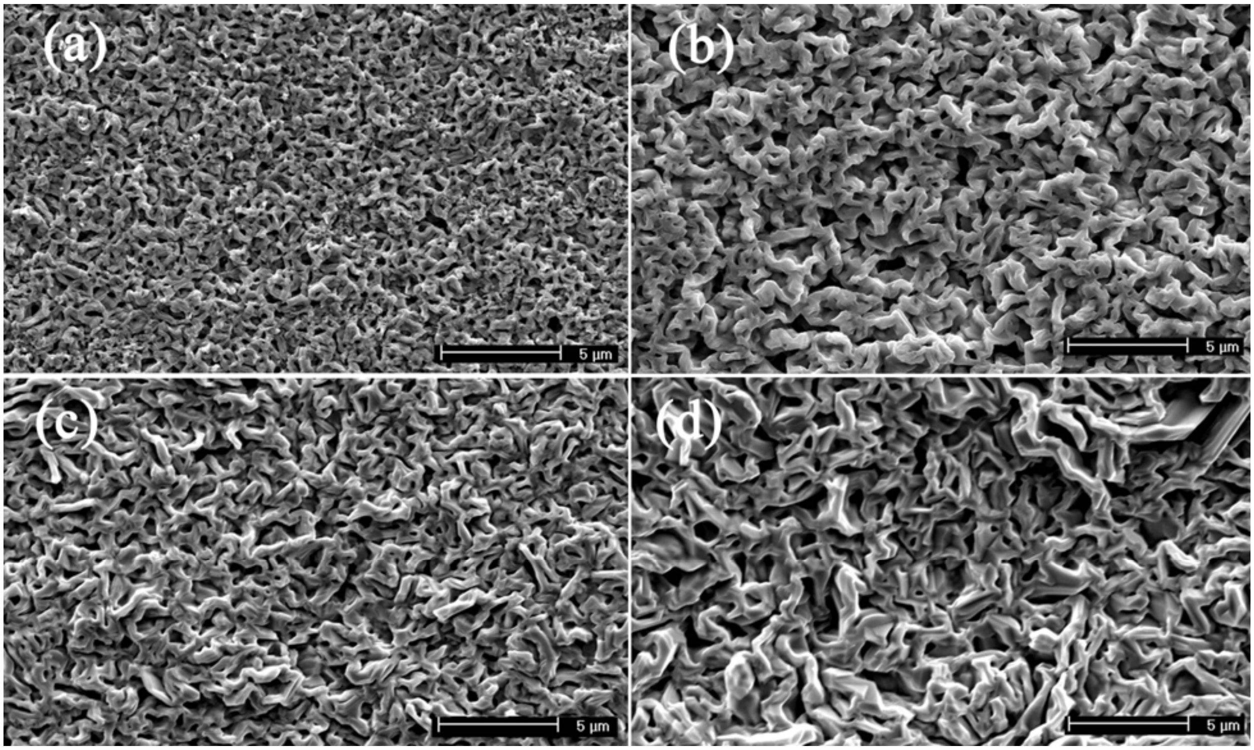

Figure 18. Surface micrographs of NiO formed on Ni at 800°C in dry air after (a) 0.25 (b) 16 (c) 100 and (d) 500 hours

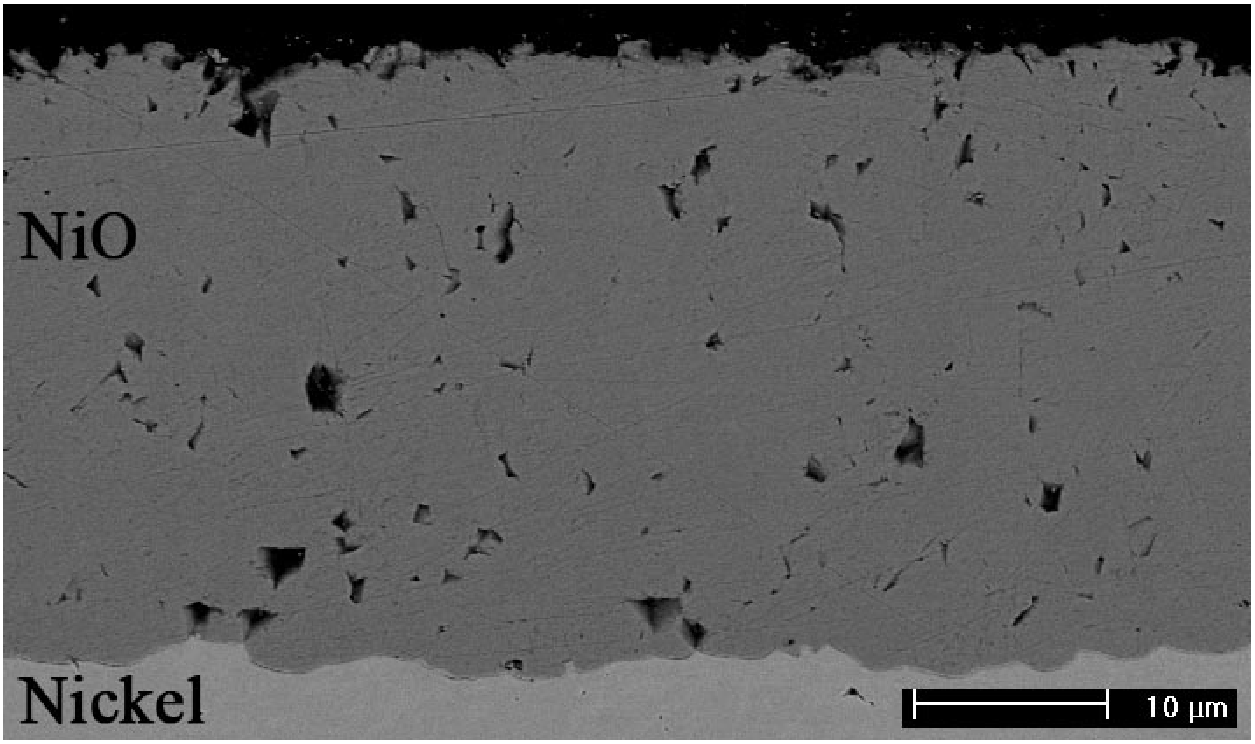

Figure 19. Cross-sectional micrograph of Ni exposed for 500 hours at 800°C

.

5.2.2 Oxidized Ni-5Cu

The surface morphology of the oxide formed on Ni-5Cu consists of two regions. Over the majority of the surface, a facetted grain structure exists with approximately 1µm diameters while cellular oxides grains are observed in regions that appear to follow the grain boundaries in the alloy. This can be seen in Figure 20.

In cross-section, the scale is duplex with an outer region of columnar grains with only a small amount of porosity and an inner region with equiaxed grains with a considerable amount of porosity.

After exposure for 100 hours at 800°C, the scale has an average thickness of 13µm. In certain regions this thickness is decreased to 8µm as shown in Figure 21. The thicknesses of both the outer and inner layers are decreased in this region. These regions may correspond to the cellular morphology observed on the surface.

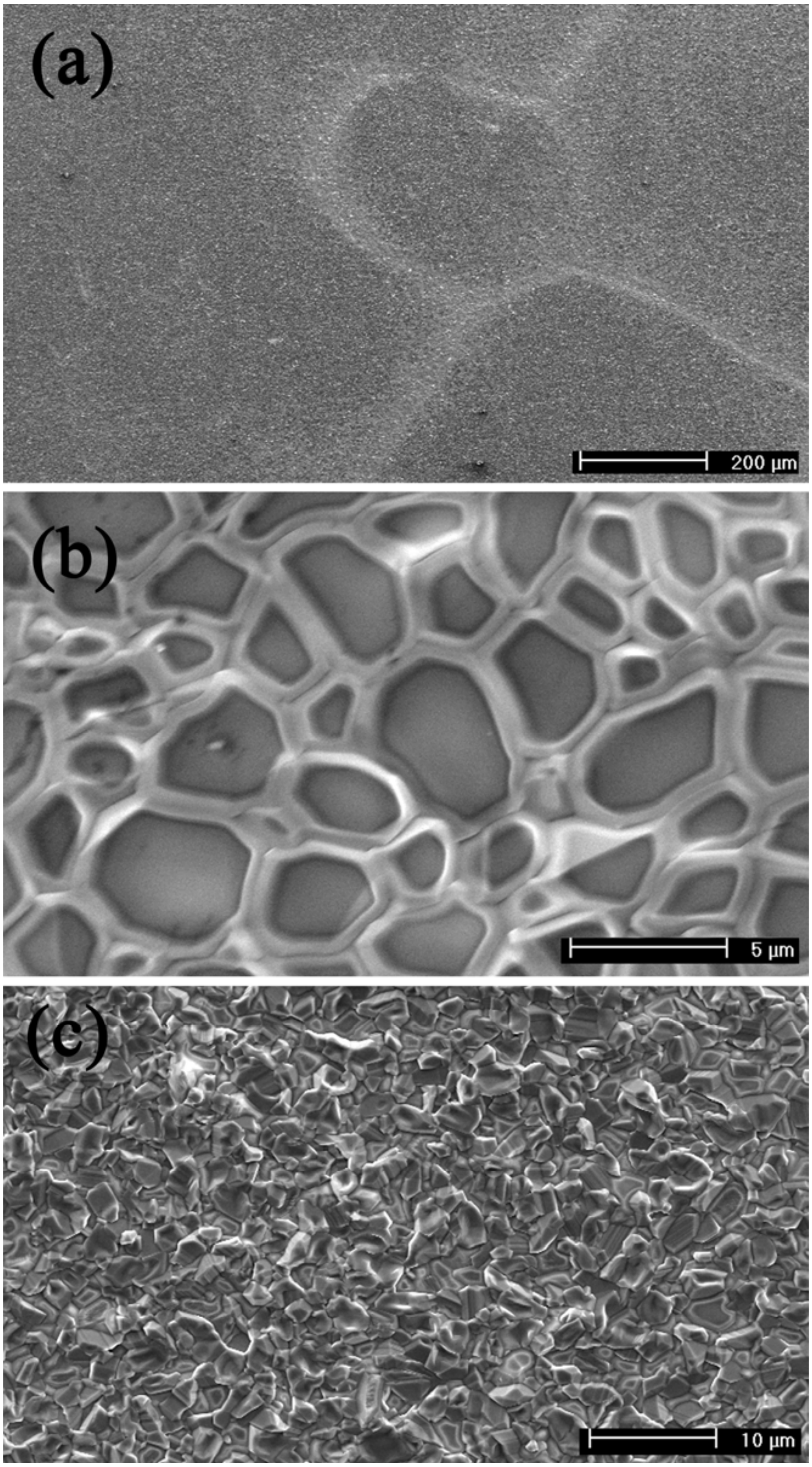

Figure 20. Surface of Ni-5Cu alloy exposed in air at 800°C for 100 hours (a) Low magnification image exhibits two distinct morphologies, a cellular structure (b) and a facetted structure (c).

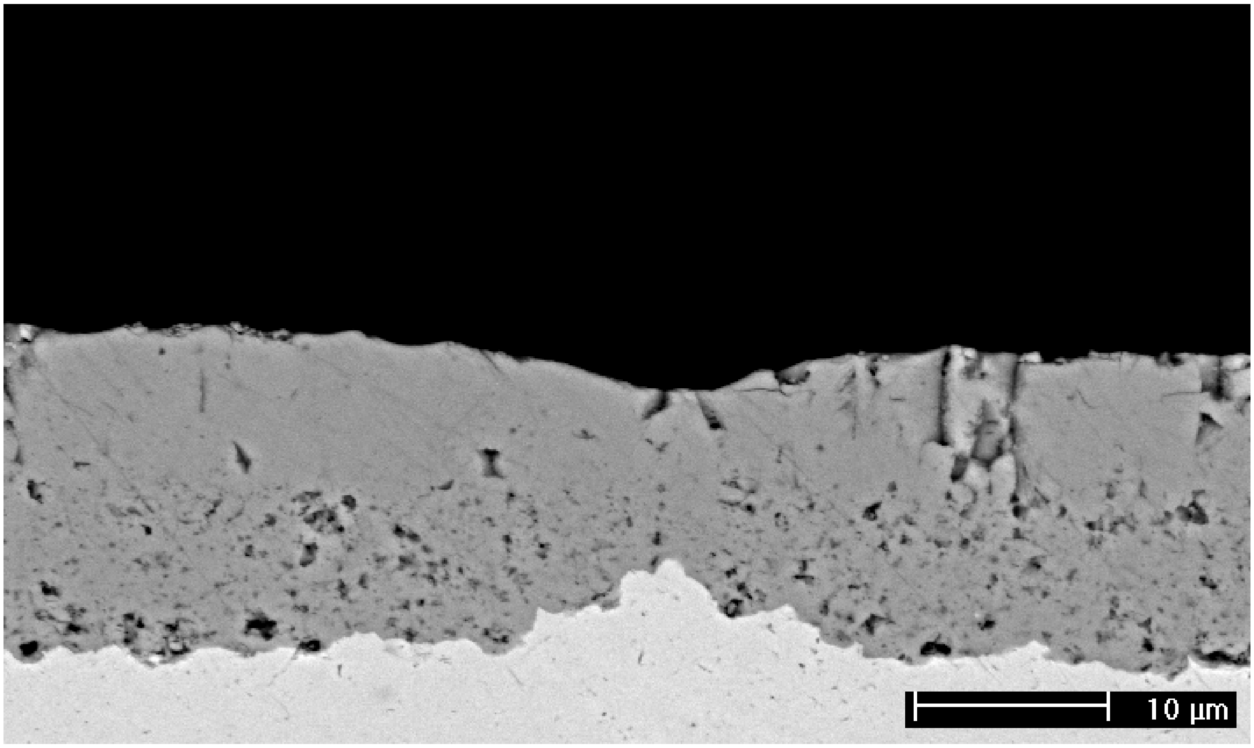

Figure 21. Cross-sectional micrograph of Ni-5Cu oxidized at 800°C exposed for 100 hours

5.2.3 Crystal Structure and Composition of Oxidized Nickel

X-ray diffraction of oxidized nickel shows that the scale is bunsenite, with a rock salt type structure. The diffraction pattern is shown in Figure 22. EDS analysis shows that this scale consists of nickel and oxygen.

5.2.4 Crystal Structure and Composition of Oxidized Ni-5Cu

X-ray diffraction of oxidized Ni-5Cu shows both NiO and CuO phases. Fixed incident scans were performed at an incidence of 2° in order to investigate the surface structure and these results are plotted in Figure 22. Even using the glancing angle scan, the NiO peaks have a greater intensity than do the CuO peaks.

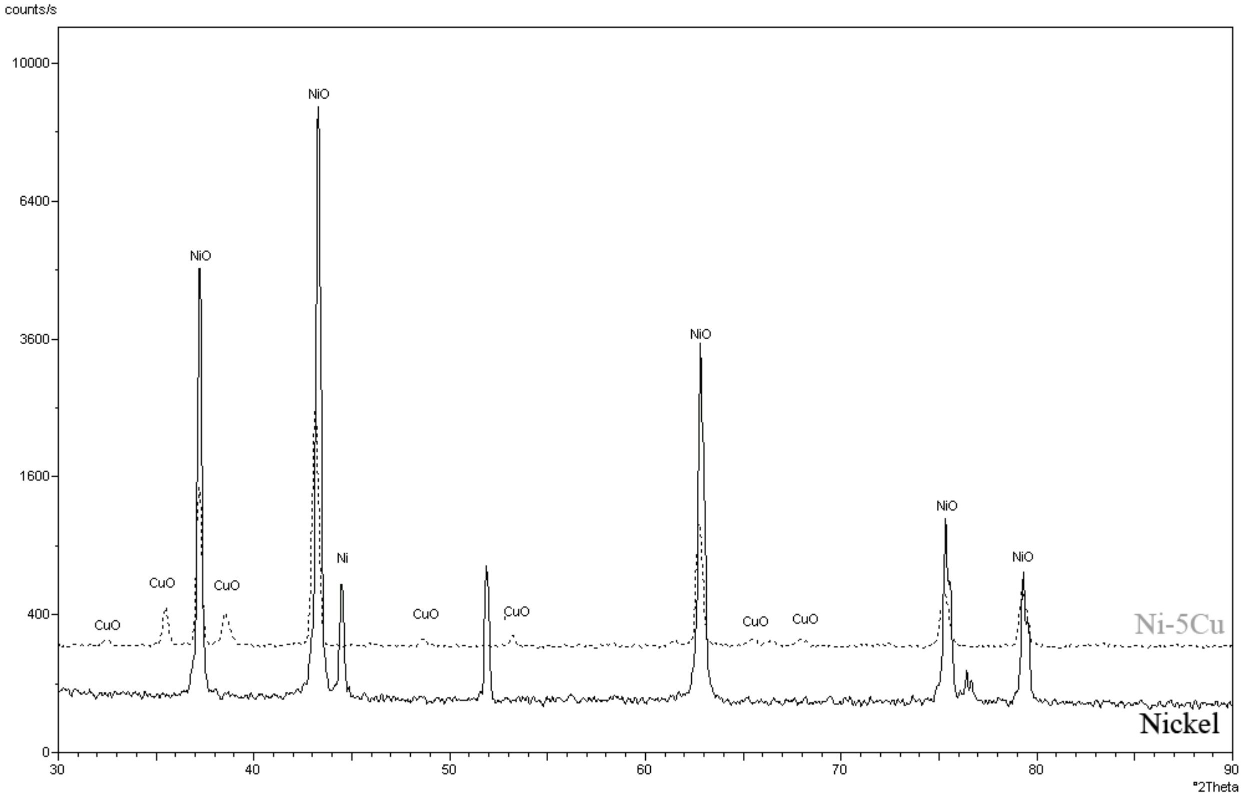

Figure 22. The X-ray diffraction patterns of Ni and Ni-5Cu exposed at 800°C for 100 hours

Energy dispersive spectroscopy was used to perform elemental analysis of the oxide scale. Line scans were conducted through the oxide and the results are plotted in Figure 23. Copper is in its highest concentration at the gas/oxide interface with the nickel/copper ratio is approximately 10:1. The nickel to copper ratio quickly decreases as the distance from the gas/oxide interface increases and after 1μm copper is not detected. The presence of CuO in the diffraction pattern indicates that some of the copper must be located in CuO crystals. However, NiO is known to dissolve between 20-30wt% Cu^{++} ions[57] and, therefore, a substantial amount of copper may be present as dissolved ions in NiO.

The existence of copper in the scale is curious. When a binary alloy is oxidized to form a continuous scale covering the surface of the alloy, it can be assumed that local equilibrium is achieved between oxide and the alloy. This equilibrium will fix the oxygen partial pressure at the alloy surface. In order for the solute element to oxidize, it must be exposed to an oxygen partial pressure greater than the dissociation pressure of the most stable oxide of the solute. Once a continuous NiO scale is formed covering the surface of the alloy, the oxygen partial pressure governed by the Ni/NiO dissociation pressure is lower then Cu/Cu_2O equilibrium and therefore copper cannot oxidize at the oxide alloy interface.

Some oxidation of copper may occur before a continuous NiO layer is formed but it is unlikely that this would produce the high concentration of copper, evenly distributed across the gas/metal interface that is observed. In addition, the concentration of copper in the scale appears to remain constant as exposure time increases indicating that copper is entering the scale at a constant rate and not being diluted by the continuing oxidation of nickel.

Copper has been observed in the oxide scales grown on dilute Ni-Cu[55, 56], Fe-Cu[58], and Co-Cu[59] alloys. In all of these alloy systems the native oxide of the parent element has a lower dissociation pressure. No adequate mechanism has been developed to understand how copper gets into the oxide scale.

Cu^{++} dissolved in NiO should not have any affect on the defect structure of the oxide. On the other hand Cu^{+} dissolved on Ni^{++} sites will decrease the cation vacancy concentration and increasing the electron hole concentration. The oxygen activity in the oxide will be greatest near the gas/oxide interface and lowest near the scale/gas interface. Near the gas/oxide interface the majority of the copper ions will be Cu^{++} and Cu^{+} will have their highest concentration near the oxide scale interface. The line profile shows a very small amount of copper across the bulk of the scale. These results infer that the concentration of Cu^{+} in the scale is small.

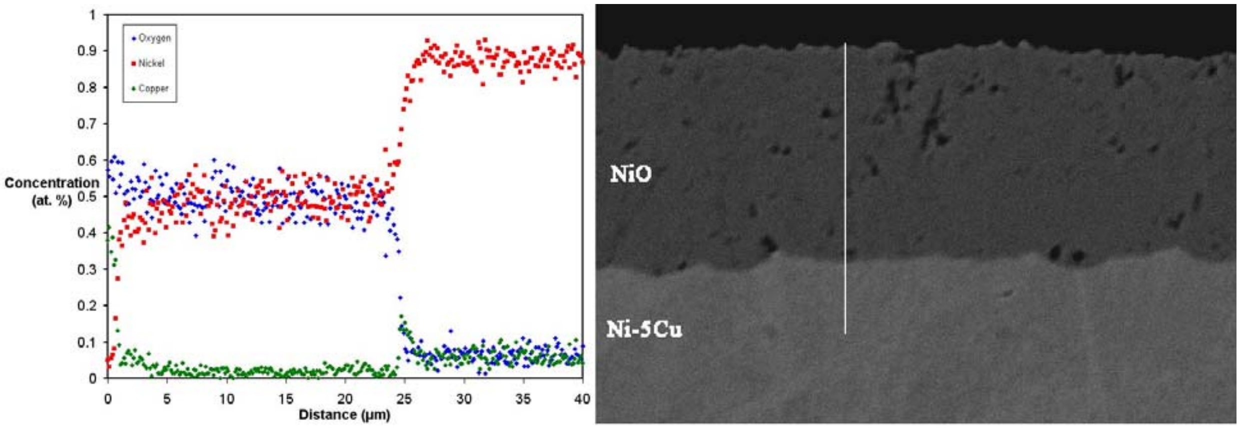

Figure 23. EDS line scan across Ni-5Cu exposed to air at 800°C for 100 hours. The origin of the plot on the left refers to the top of the line, in the micrograph on the right.

5.2.5 CeO_2 Coated Ni and Ni-5Cu

PLD was used to deposit CeO_2 on nickel and Ni-5Cu. The thickness of the coating ranged between approximately 75-200nm from specimen to specimen and the coated thickness had 50nm variation on a given specimen.

The morphology of the oxide surface on nickel coated with CeO_2 is drastically different than that of uncoated nickel. NiO grown on coated nickel is in the form of mounds that are approximately 2μm high. The distinct oxide morphologies are seen in Figure 24. The difference between the two oxide scales is just as noticeable when the scales are viewed in cross-section. The thickness of the uncoated scale is greater than the thickness of the coated scale by roughly a factor of four. The coated scale shows a greater thickness variation as might be expected from the surface micrographs. Following oxidation, there is no distinct CeO_2 layer found across the surface of the exposed specimen. There are ceria particles that can be found at the outside of the scale as can be seen in Figure 25. The presence of these particles near the gas/oxide interface suggests that the scale is growing primarily inward. Pure nickel is known to oxidize outwardly, and the change in growth direction is a common result of the REE.

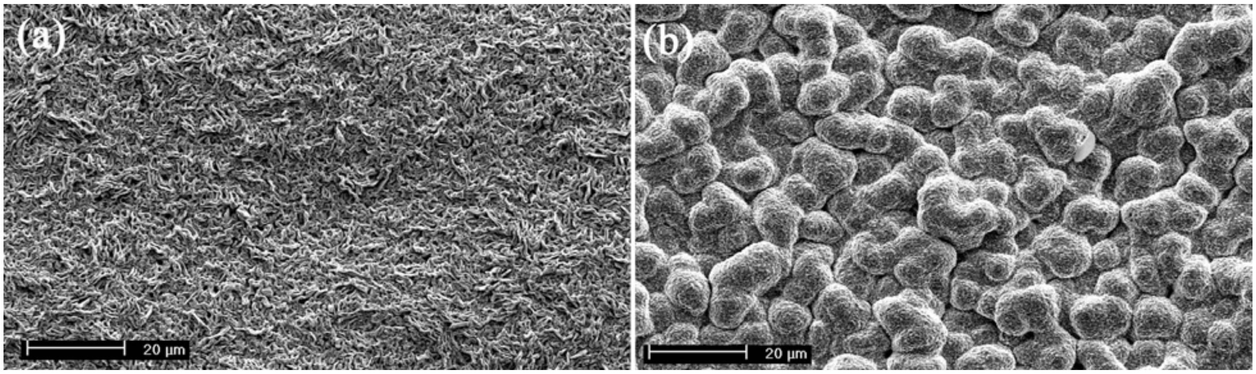

Figure 24. Surface micrographs of (a) uncoated and (b) coated Ni exposed in air for 500 hours at 800°C

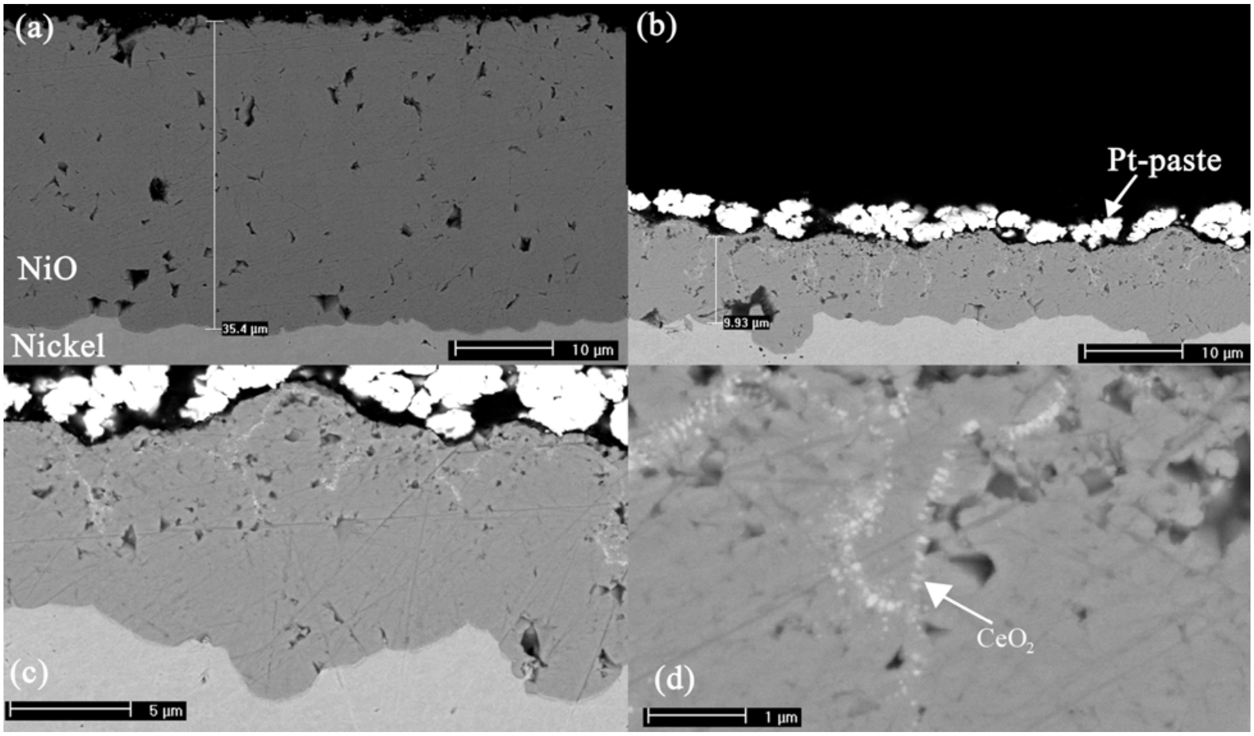

Figure 25. Cross-sectional micrographs of (a) uncoated and (b) coated Ni exposed in air for 500 hours at 800°C. (c) and (d) are high magnification images of coated Ni

These results clearly demonstrate that reactive elements additions can substantially decrease the growth rate of NiO. However, the mechanism that produces this change is unclear. As described in the introduction, the two leading theories are the poisoned interface model (PIM), and the grain boundary segregation model. In an attempt to investigate the feasibility of the PIM, two nickel sheets were pre-oxidized for 15 minutes at 800°C producing an approximately 1μm thick scale. One of these oxidized coupons was then coated with CeO_2 and then both coupons were exposed for an additional 50 hours. A schematic representation of these is shown in Figure 26. Following this treatment, the surface of pre-oxidized and CeO_2 coated specimen looked similar to the surfaces of the coated nickel that had not received the pre-oxidation treatment. Cross-sectional micrographs show that the scale thickness is reduced in the coated nickel with respect to the uncoated nickel. The pre-oxidized and coated nickel has a thicker scale then the non-pre-oxidized nickel, but this difference can be attributed to the initial oxide growth that occurred prior to coating. Cross-sectional micrographs are shown in Figure 27.

The pre-oxidation treatment created a dense, continuous barrier between the metal-oxide interface and the surface of the oxide. This barrier did not allow the deposited ceria to contact unoxidized nickel and the reduction of the growth rate of NiO was still observed. The only possibility of the ceria affecting the metal-oxide interface would occur if ceria could be transported through 1μm of NiO during exposure. EDS measurements only found ceria in the outer portion of scale. These results clearly indicate that other mechanisms apart from the poisoned interface can produce the reactive element effect on nickel.

The concentration of ceria near the gas-oxide interface indicates that the scale is growing predominantly inward. Excluding changes in the injection of Ni ions into the scale resulting from a poisoned interface, a change in the grain boundary diffusivity in NiO is the most probable cause for the change in the oxidation mechanism.

No tests were performed in this study to check the presence of ceria at NiO grain boundaries. However, Moon [35] performed transmission electron microscopy on nickel with a CeO_2 coating applied by sol-gel deposition and found cerium at grain boundaries in NiO after exposure at 900°C.

There is evidence that the presence of misfit ions in NiO grain boundaries suppresses diffusion. Experimentally, Atkinson et al.[60] found that the segregation of Ca and Si in NiO bicrystals has decreased nickel diffusion along boundaries. Duffy and Tasker[61] studied the effect of ceria in NiO grain boundaries using atomistic modeling, finding that the presence of an isolated Ce^{4+} ion in a grain boundary increases the activation energy for the diffusion of vacancies to a value greater than the activation energy of bulk diffusion. The exact mechanism by which solutes inhibit diffusion along oxide grain boundaries is not presently agreed upon. However, the difference in size and electron affinity of solute ions may produce defect clusters in the boundary, limiting the mobility of vacancies or the introduction of misfit ions into a grain boundary may change the vacancy migration path as a result of the physical distortion.

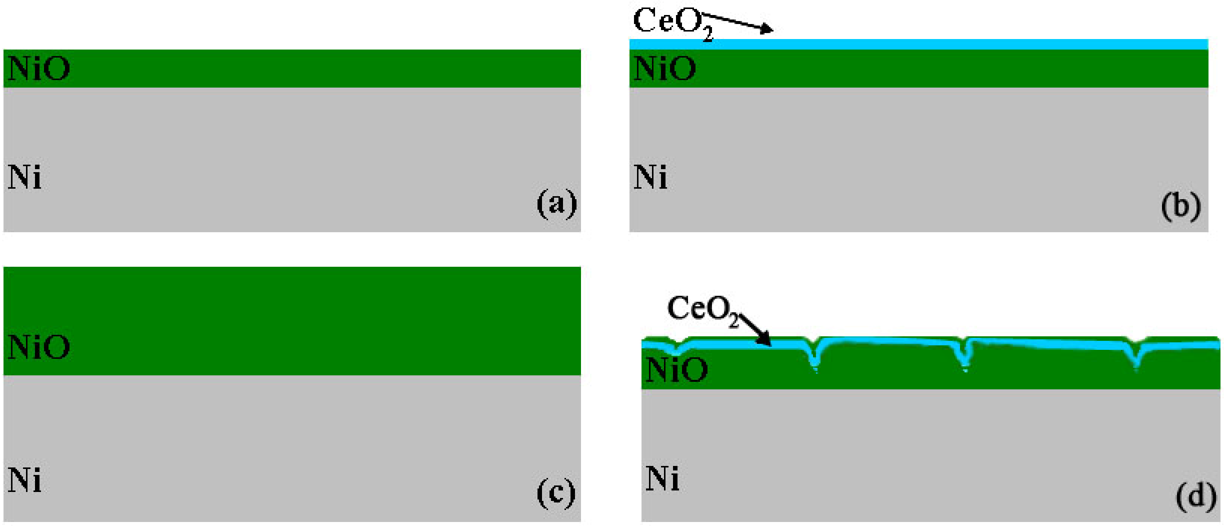

Figure 26. Schematic representation of (a) uncoated nickel oxidized for 15 minutes, (b) nickel pre-oxidized for 15 minutes followed by CeO2 deposition (c) additional 50 hour exposure pre-oxidized nickel, (d) additional 50 hour exposure of the pre-oxidized and coated

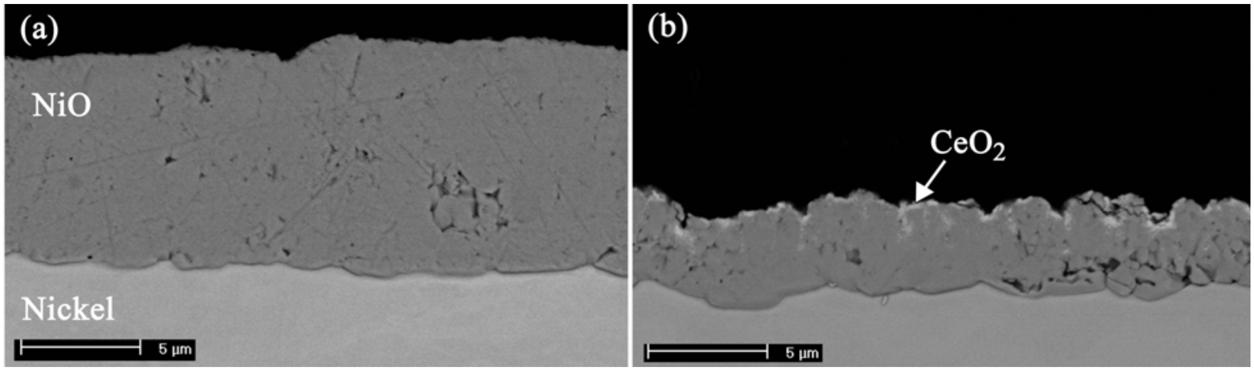

Figure 27. Nickel was oxidized for 15 minutes at 800°C in air and then (a) re-exposed for 50 hours, and (b) a separate specimen coated with CeO2 following pre-oxidation and then re-exposed for 50 hours.

5.3 ASR

ASR measurements were performed to determine the amount of electrical degradation that the interconnect would introduce into a cell after a given exposure time. The ASR tests were preformed on specimens that were pre-oxidized for different times and these results were used to determine a rate of degradation.

5.3.1 Nickel

As stated earlier, ASR is proportional to the thickness and the resistivity of the oxide scale. As a result, the ASR should increase with time proportionally to the growth rate of the oxide. Figure 28 shows the ASR of nickel exposed to air at 800°C plotted against the square root of time. This plot shows an initial rapid increase in ASR lasting approximately 24 hours followed by a nearly parabolic increase. It was previously shown the growth rate of NiO follows the parabolic rate law and therefore the ASR should increase following this dependence. Figure 29 shows that nickel undergoes an initial period of rapid oxidation, which is followed by parabolic growth.

Figures 28 and 29 demonstrate that the growth of NiO along with the ASR of nickel, increase parabolically with exposure time. These results are strong evidence that NiO growth is the predominant factor that controls the increase in ASR of nickel.

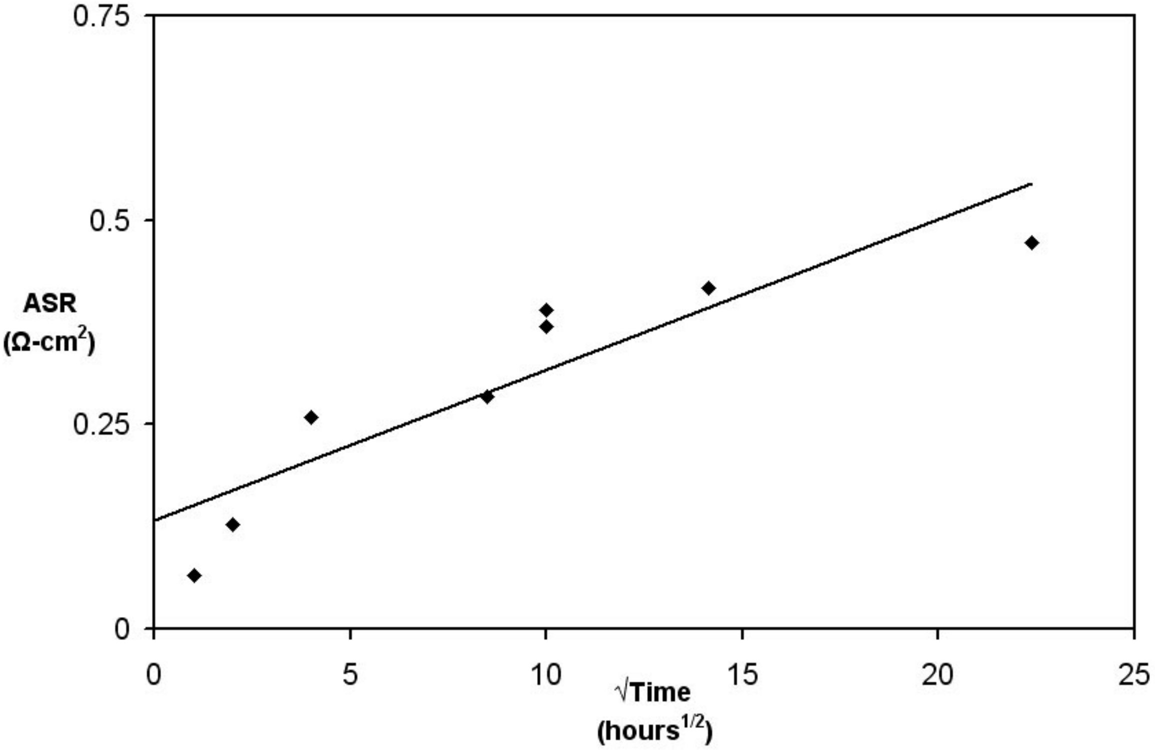

Figure 28. ASR results for Ni at 800°C

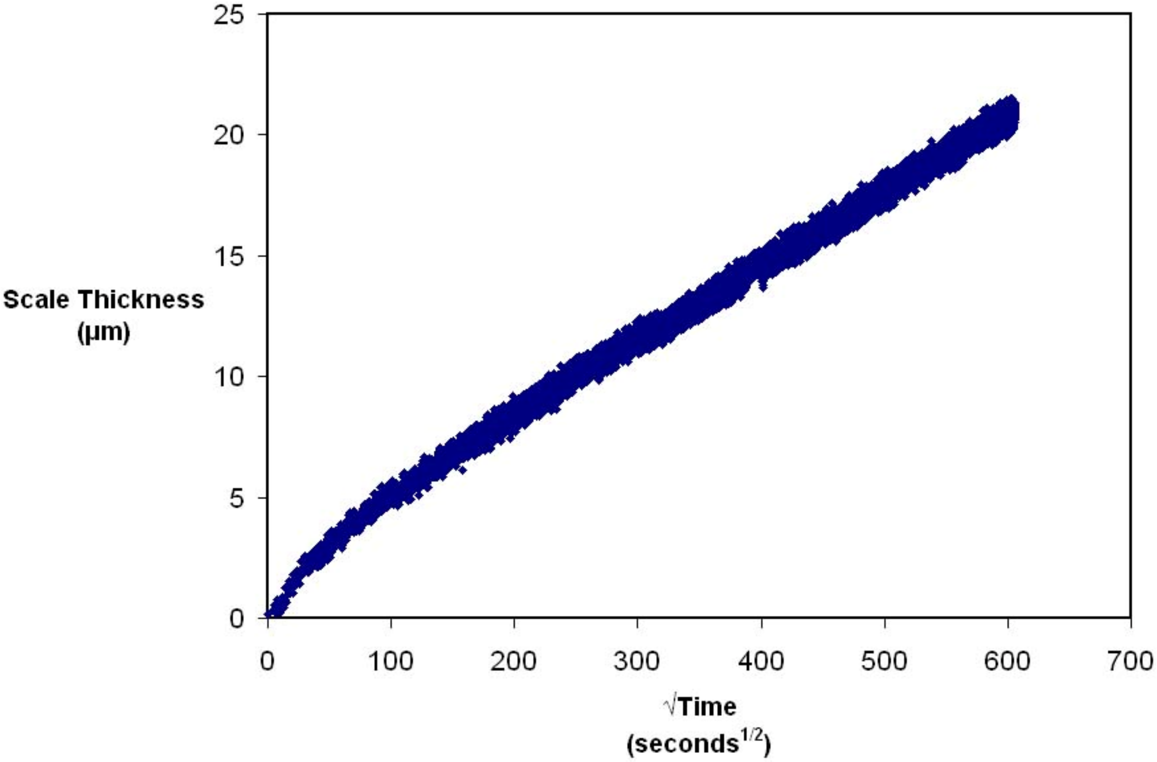

Figure 29. Scale thickness of NiO in nickel exposed at 800°C. Thickness measurements were calculated from TGA data

5.3.2 Ni-5Cu

Ni-5Cu was also oxidized at 700, 800, and 900°C. Coupons where oxidized at different time at 800°C and the ASR results are plotted in Figure 31. These values are similar to that of pure nickel. It was envisioned that copper would dissolve as Cu^{+1} ions, increasing the electron hole concentrations, therefore, reducing the resistivity, and decreasing the cation vacancy concentrations. It does not appear that this occurred. EDS measurements only detect copper in the outer portion of the scale and XRD detected CuO. Also, any copper left at the outer portion of the scale would be exposed to a high enough oxygen partial pressure to be doubly ionized. Differences in the scale morphology, and porosity, are probably the largest sources of the different electrical properties.

5.3.3 CeO_2 additions

Nickel coated with ceria was exposed for times up to 500 hours. The results are shown in Figure 31. The ASR values are decreased by a factor of four with respect to uncoated nickel. This is roughly proportional to the decrease in scale thickness observed in Figure 29. Ceria was also deposited on the Ni-5Cu alloy. Ceria deposited on Ni-5Cu reduced the oxide growth similar to ceria deposited on Ni.

The decrease in ASR of ceria coated specimens is proportional to decrease in thickness and therefore the resistivities of oxides are similar. If Ce^{4+} ions were dissolved in the scale, doping would occur decreasing the electron hole concentration, increasing the resistivity of the oxide.

$$2h^{\cdot} + CeO_2 \xrightarrow{NiO} Ce_{Ni}^{\cdot\cdot} + O_O^x + \frac{1}{2}O_2$$

It has been reported by Atkinson and Taylor [54] that the solubility of Ce^{4+} in NiO is very small. Therefore, ceria doping should not have a large effect on the electrical properties of the NiO.

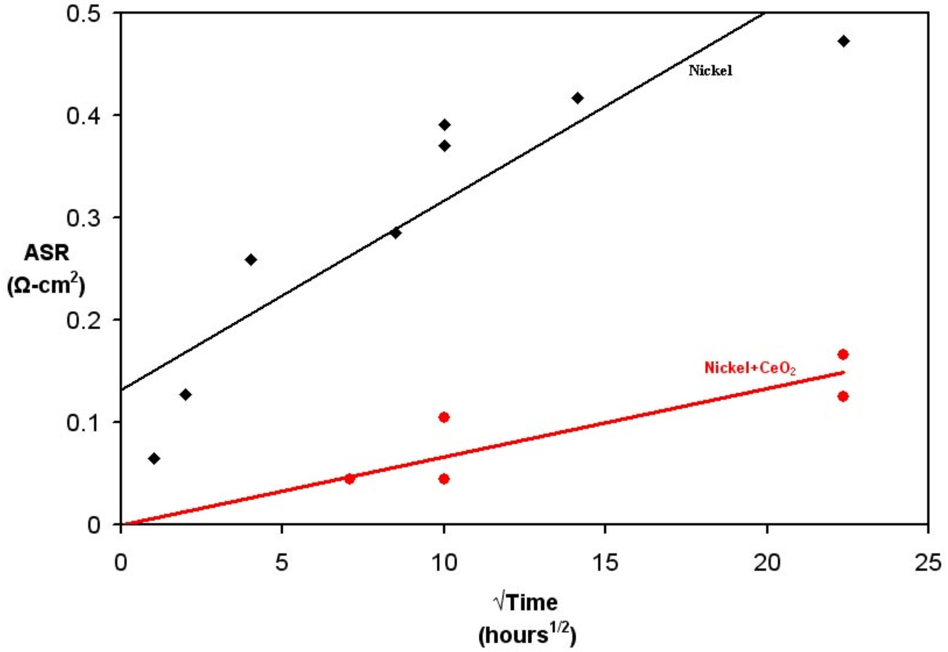

Figure 30. The ASR of Ni, and Ni coated with CeO_2 at 800°C

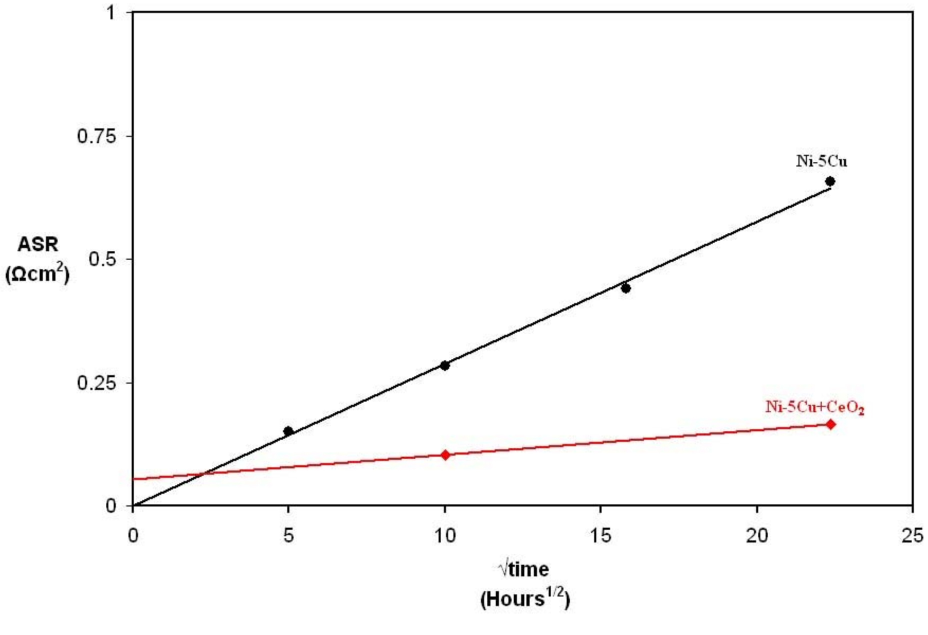

Figure 31. ASR values for Ni-5Cu, and Ni-5Cu coated with CeO_2 at 800°C

The ASR of Ni+CeO_2 after 500 hours is 0.15Ωcm^2. This value is similar to the ASR measured on Ebrite, a ferritic stainless steel which is a popular candidate interconnect material.[62] There is significant scatter in the ASR data in the literature[52, 63-65] and the Ni+CeO_2 results obtained in this work are at the high end of the scatter. The data shown in Figure 30 can be used to make a rough estimate of the ASR of Ni+CeO_2 at the desired SOFC lifetime of 40,000 hours. This extrapolation predicts an ASR of 2.5 Ωcm^2. This estimate assumes that the mechanisms that increase the ASR with time such as oxide growth continue at the same rate and no new factors affect the rate ASR increase. After 500 hours the measured ASR is approaching the desired lifetime ASR of 0.1 Ωcm^2. [42]

5.3.4 Experimental Error

In the literature, the rate of degradation is often determined using a continuous ASR measurement where an electrode is applied to the interconnect and the alloy is subsequently exposed. This method was not employed due to outward growth of NiO. If an electrode was applied prior to oxidation, a number of factors could affect the measured resistivity. If the electrode remained on the surface of the growing oxide, the results should be reasonable. However, if the oxide grew through the electrode, the measured resistivity would be incorrectly low if continuous paths of the high conductivity electrode remained close to the alloy surface, as seen in Figure 32. Also, regions of the oxide might grow around an area of the electrode separating it from the rest of the electrode. This would result in a decrease of the connection area which would increase the resistivity. An additional factor is that the resistivity of the electrode can change during the test. Sintering can increase the conductivity of the electrode and change the electrode/oxide interface behavior. Many reports in the literature have shown ASR versus time plots where the ASR has an initial maximum and continually decreases throughout the test. This result is probably influenced by the sintering of the electrode and the rate of degradation produced by oxide growth is obscured.

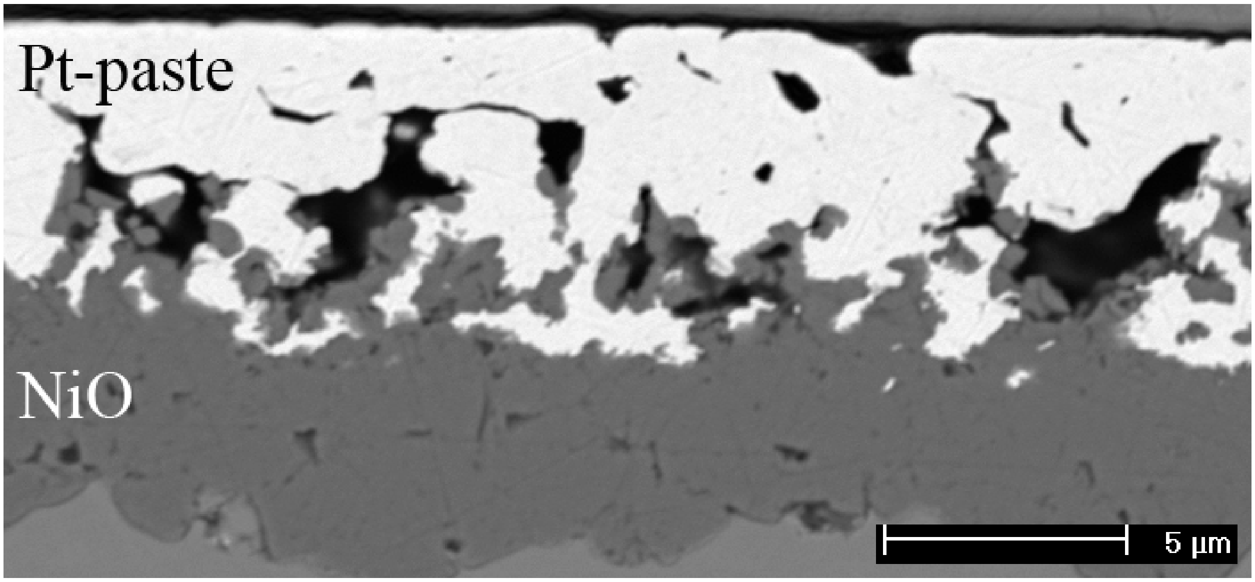

Figure 32. Pt paste applied after 1 hr pre-oxidation treatment, followed by 20 hour exposure

5.4 THEORETICAL DETERMINATION OF THE ASR

The literature contains many investigations where the growth rates of oxides on metals have been measured and many other studies have measured the electrical properties of bulk oxides. However, few studies have determined the resistivity of an oxide grown on a metal or alloy. Therefore the simplest determination of how the ASR will increase with time can be calculated using oxidation rate data along with resistivity measurements made on bulk ceramics.

$$ASR = \rho' x \quad (124)$$

Here ρ*'* is the resistivity of a bulk ceramic and *x* is the thickness of an oxide at a given time.

The simplicity of the above approximation makes it useful; however there are several sources of error that will limit the accuracy. Specifically, the electrical properties of an oxide grown on a metal should be different from the electrical properties of a bulk oxide. In order to model the ASR as a function of time, the electrical properties of the oxide growing on the interconnect must be determined.

Certain assumptions will be made in the creation of this model. These assumptions will follow the assumptions made in Wagner's parabolic oxidation theory.[13]

1. The oxide scale is compact and perfectly adherent.
2. Thermodynamic equilibrium is established at the metal-scale interface and the scale-gas interface.
3. Only small deviations from stoichiometry exist in the oxide scale.
4. Thermodynamic equilibrium is established locally throughout the scale.
5. The scale is thick with respect to the distance at which space charge effects occur.
6. The dependence of point defect concentration on atmospheric composition is known.

5.4.1 Electrical Properties

The electrical properties of oxides are generally controlled by the concentration of mobile charge carriers. At a given temperature, this concentration may be controlled by intrinsic defects; electrons jumping from the valance band to the conduction band, or extrinsic defects, where free electrons or electron holes are created to maintain electrical neutrality in the crystal. When transition metal oxides are at the operating temperatures of SOFCs, the carrier concentration in oxide is controlled by the extrinsic defect concentration. If the impurity concentration is low, then carrier concentration in the oxide will be controlled by the defect concentration that forms as result of equilibration of the oxide with the atmosphere

5.4.2 Oxygen Partial Pressure Gradient

It is assumed that thermodynamic equilibrium is established at the gas/oxide and oxide/metal interfaces. These equilibria will set the oxygen activities at the respective interfaces which will produce a gradient in the oxygen partial pressure across the scale. The exact shape of the gradient has not been measured but estimates can be made.

5.4.3 Resistivity Gradient

Further, thermodynamic equilibrium is established locally through out the scale. If the oxygen partial pressure gradient is known, the local resistivity can be calculated throughout the scale using appropriate charge neutrality conditions, in which the free carrier concentration is related to the oxygen partial pressure.

5.4.4 Calculation of ASR

Once the resistivity profile, $\rho(x)$ has been determined, the ASR can be calculated by integrating $\rho(x)$ the with respect to scale thickness. A normalized reaction coordinate is used to describe the oxide thickness, where $x=0$ at the oxide/metal interface and $x=L$ at the gas/oxide interface.

$$ASR = \int_{o}^{L} \rho(x)dx \, (125)$$

The scale can be viewed as a sequence of infinitesimally small resistive layers connected in series that produce the overall resistivity of the scale.

5.5 ASR OF THERMALLY GROWN NICKEL OXIDE

In this study the ASR of oxidized nickel was measured at various times at 800°C. These results will be used to test the proposed model.

5.5.1 Electrical Properties of NiO

As stated previously, there is some debate over the relative defect concentrations in NiO, but if it is assumed that the predominant defect is a doubly ionized cation vacancy then the defect equilibrium was stated in equation (45).

$$K = \frac{[V''_{Ni}]p^2}{p_{O_2}^{1/2}} \, (45)$$

This equation can be rearranged to show the dependence of the electron hole concentration on oxygen partial pressure.

$$p = 2^{1/3} K^{1/3} p_{O_2}^{1/6} (126)$$

If it is assumed that the concentration of mobile electrons is negligible, then the conductivity and resistivity can be expressed as equations (127), and (128) respectively.

$$\sigma = e\mu_p p \, (127$$

$$\rho = \frac{1}{e\mu_p p} = \frac{1}{e\mu_p 2^{1/3} K^{1/3} p_{O_2}^{1/6}} (128)$$

If the resistivity of NiO equilibrated with oxygen at 1atm is designated ρ°, equation (129, then equation (128) can be simplified.

$$\rho^\circ = \frac{1}{2^{1/3} K^{1/3} e\mu_h} \quad 129)$$

$$\rho = \rho^\circ p_{O_2}^{-1/6} \quad (130)$$

5.5.2 Oxygen Partial Pressure Gradient

The oxygen partial pressure gradient was calculated by Pettit, using parabolic rate constants of NiO on Ni exposed at different oxygen partial pressures.[66] Equation (131) shows the variation in oxygen activity across the normalized reaction coordinate, where unit activity is the oxygen activity at the dissociation pressure of NiO. Here *n* is the dependence of the cation vacancy concentration on oxygen activity with *n/3* for doubly ionized vacancies.

$$a_O^{1/n} = 1 + \left(a_{O(atm)}^{1/n} - 1\right)\frac{x}{L} \quad (132)$$

This equation can be expressed in terms of oxygen partial pressure where 1atm of oxygen is the standard state, equation (133) and if the predominant defect is assumed to be doubly ionized cation vacancies, then equation (134) is produced.

$$p_{O2}^{1/n} = p_{O_2(Ni/NiO)}^{1/n} + \left(p_{O_2(atm)}^{1/n} - p_{O_2(Ni/NiO}^{1/n}\right)\frac{x}{L} \quad (133)$$

$$p_{O_2}^{1/6} = p_{O_2(Ni/NiO)}^{1/6} + \left(p_{O_2(atm)}^{1/6} - p_{O_2(Ni/NiO)}^{1/6}\right)\frac{x}{L} \quad (134)$$

The oxygen partial pressure gradient is plotted in Figure 33 against a normalized reaction coordinate.

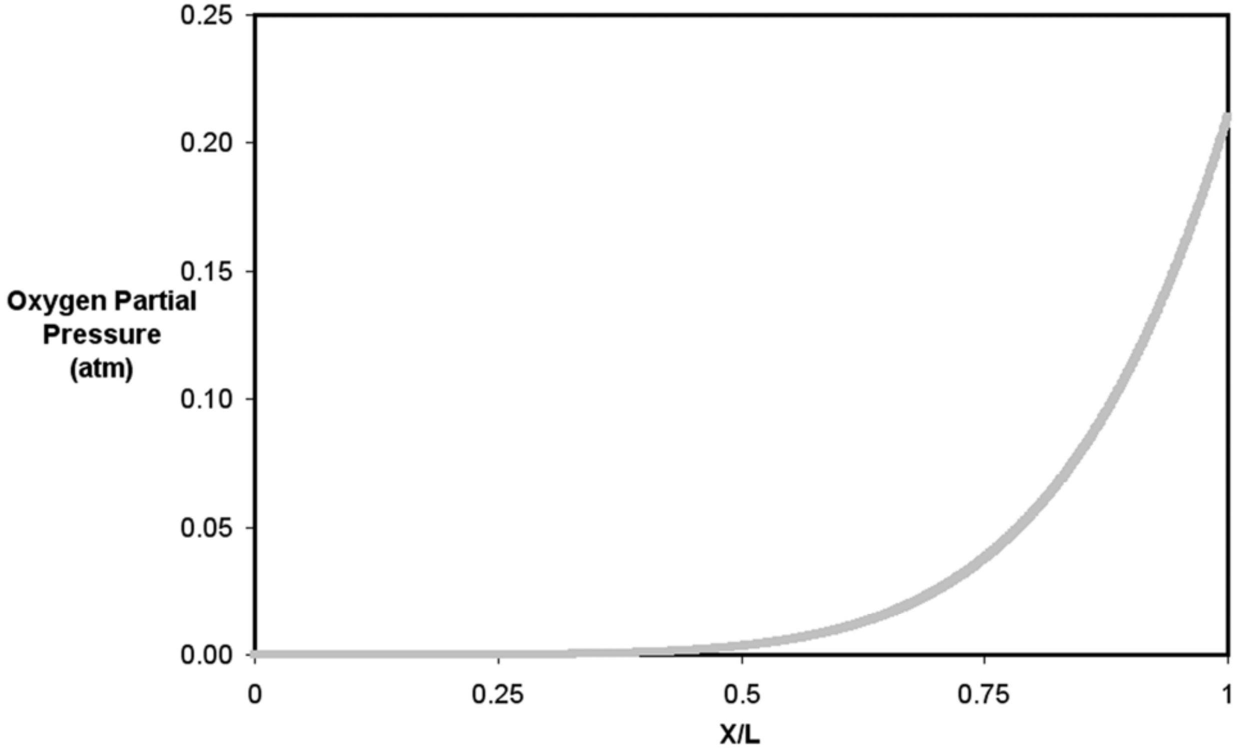

Figure 33. Oxygen partial pressure gradient across thermally grown NiO

5.5.3 Resistivity Gradient and ASR integration

The resistivity gradient across the scale can now be determined with knowledge of oxygen partial pressure gradient and the relationship between the electron hole concentration and the oxygen partial pressure. Combining equations (130) and (134) produces equation (135).

$$\rho(x) = \rho^{\circ}\left\{ p_{O2(Ni/NiO)}^{1/6} + \left[p_{O2(atm)}^{1/6} - p_{O2(Ni/NiO)}^{1/6} \right] \left(\frac{x}{L} \right) \right\}^{-1} \quad (135)$$

The resistivity gradient across the scale is plotted in Figure 34.

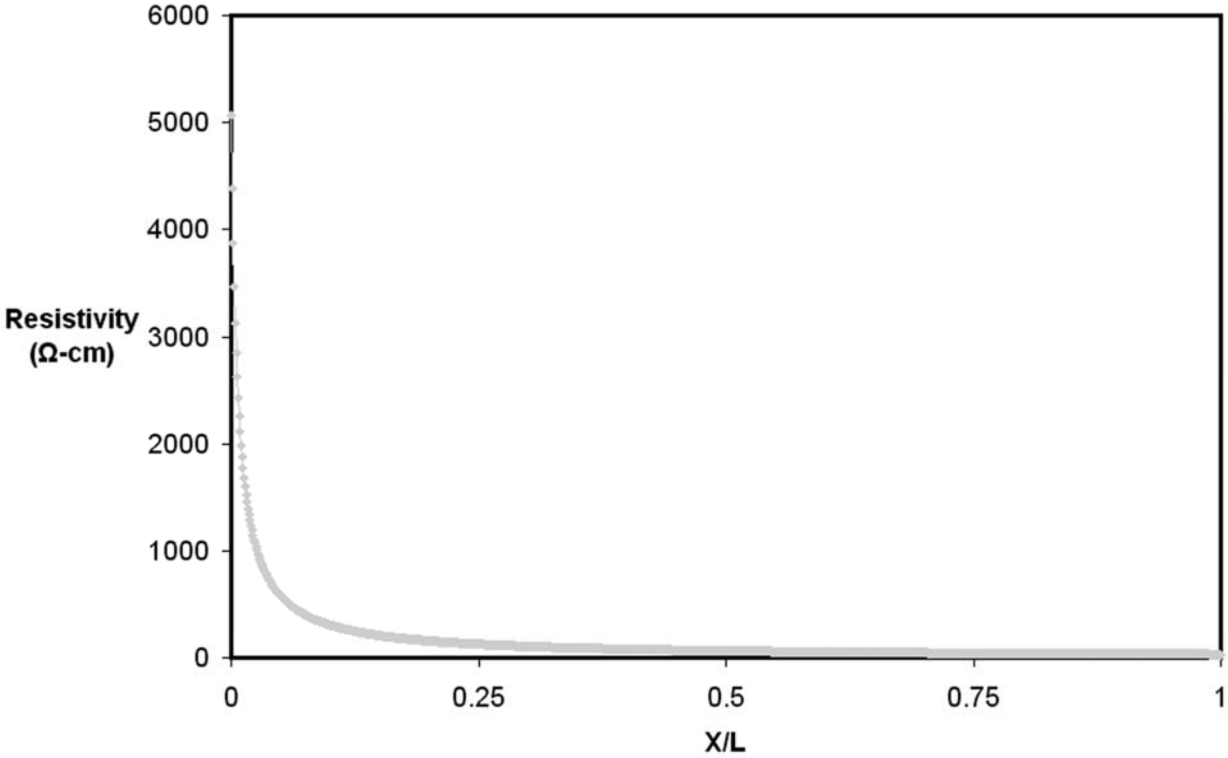

Figure 34. Resistivity gradient across thermally grown NiO

The ASR can now be calculated as by integrating the resistivity profile.

$$ASR = \int_0^L \rho(x)dx \quad (124)$$

$$ASR = \frac{\rho^\circ L}{\left(p_{O2(atm)}^{1/6} - p_{O2(Ni/NiO)}^{1/6}\right)} \ln\left(\left|\frac{p_{O2(atm)}^{1/6}}{\left(p_{O2(Ni/NiO)}^{1/6}\right)}\right|\right) \quad (136)$$

The ASR expressed in equation (136) is directly proportional to the scale thickness *L*, and a function of the materials properties ρ°, and the oxide dissociation pressure, along the oxygen partial pressure of the atmosphere to which it is exposed. The value of ρ° $=25\Omega cm^2$ for NiO at 800°C was taken by interpolating the data of Meier and Rapp.[67]

The ASR expressions can be simplified to the form

$$ASR = \tilde{\rho}(x)L \quad (137)$$

Where $\tilde{\rho}(x)$ is the resultant resistivity of the oxide scale. This value takes account of the variation in properties across the scale and is only a function of the atmospheric oxygen partial pressure at a given temperature.

$$\tilde{\rho}(x) = \frac{\rho^\circ}{\left(p_{O2(atm)}^{1/6} - p_{O2(Ni/NiO)}^{1/6}\right)} \ln\left(\left|\frac{p_{O2(atm)}^{1/6}}{\left(p_{O2(Ni/NiO)}^{1/6}\right)}\right|\right) \quad (137)$$

5.5.4 Comparison of Measured Predicted Values and Results

Figure 35 shows the comparison of theoretical ASR and measured ASR values plotted against the square root of time. The theoretical ASR is calculated using the value of $\tilde{\rho}(x)$ determined in the previous sections along with the thickness of the oxide scale calculated using mass changes measurements along with literature values of NiO density. There is good agreement between the measured and calculated ASR values.

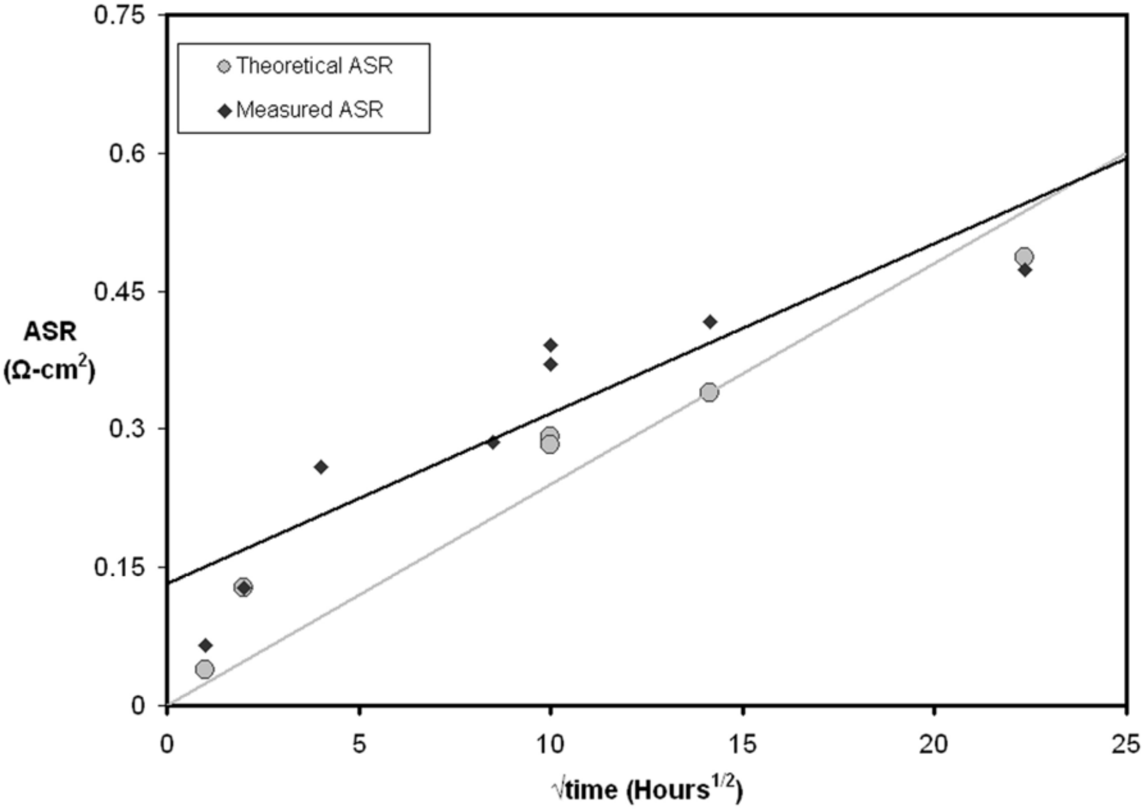

Figure 35. Experimental and theoretical ASR results for Ni oxidized at 800°C in air

A projection of the ASR as a function of time was then developed. The value $\tilde{\rho}(x)$ was used as the resistivity of the scale, and the scale thickness was calculated using the parabolic rate constant. This expression is obtained by combining equations (41), (47) and (137) and given in equation (138) and is plotted in Figure 36.

$$ASR(t) = \tilde{\rho}(x)\sqrt{\frac{V_{NiO}^2 y^2}{M_O} k_p'' t} \quad (138)$$

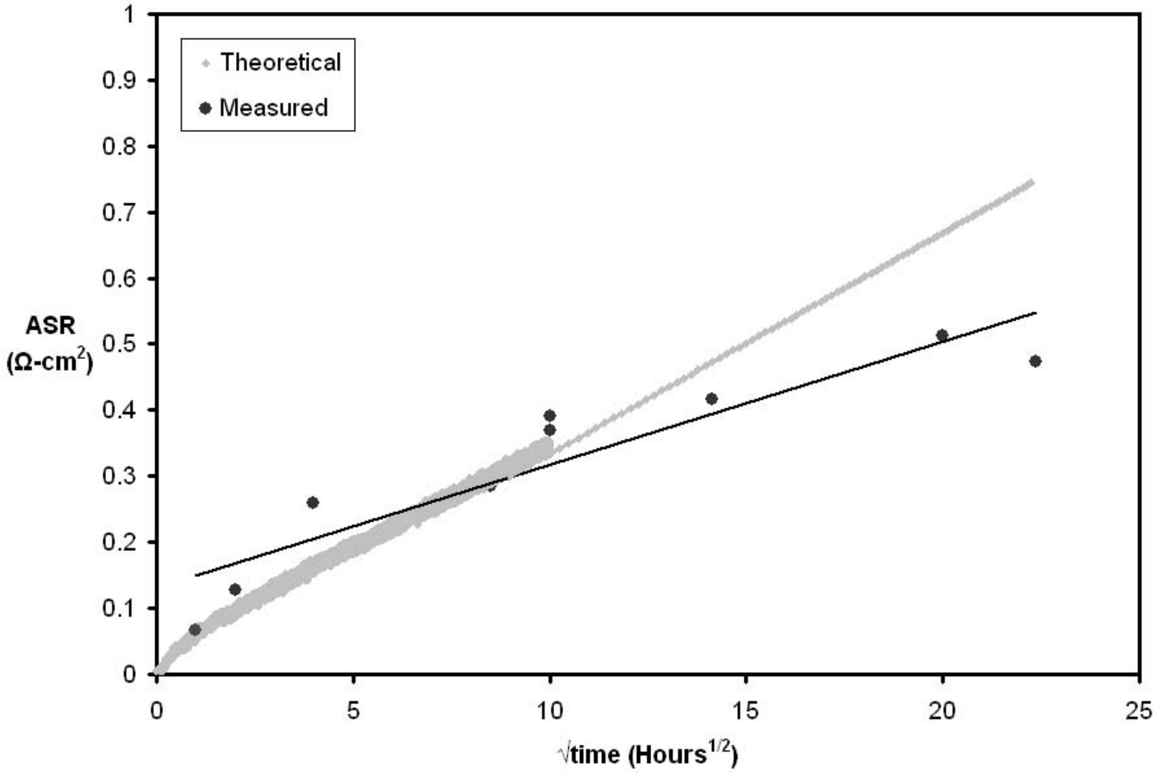

Figure 36. Theoretical ASR as function of time

5.5.5 Assumptions and Sources of Error

The Wagner theory of oxidation has been supported by many studies which gives credence to the assumptions made. The largest source of error may result from the first assumption, that the scale is perfectly compact and adherent. Some porosity is observed in cross-sectional micrographs of the oxide scale. These pores will produce infinite electrical resistivity. The oxygen partial pressure is nearly constant in a pore and existence of pores will alter the oxygen partial pressure gradient in a region surrounding the pore. The oxide structure adjacent to grain boundaries may be quiet different from the bulk and as a result the local oxygen partial pressure, hole concentration, along with the hole mobility may vary widely from the bulk oxide.

It is also assumed that resistivity of NiO is proportional to $p_{O_2}^{-1/6}$. Studies have found the proportionality of the exponential to vary between *n=4* where singly ionized cation vacancies are the predominant defect and *n=6* where doubly ionized cation vacancies are the predominant defect.

5.5.6 Application of Theoretical ASR Calculation

The ability to predict the magnitude of the ASR of an untested candidate interconnect alloy is valuable. Because the ASR of an interconnect is proportional to the thickness and the resistivity of the oxide scale, these two quantities must be known. A great deal of research has been conducted over the years determining the rate of alloy oxidation at elevated temperatures. This literature allows one to determine or at least estimate how thick an oxide scale will be after a given exposure time. This knowledge along with the electrical properties of the oxide scale will allow the calculation of the ASR of a given alloy. However, the electrical properties of oxide scales have not been extensively measured. On the other hand, the properties of bulk oxides have been extensively studied. With knowledge of the oxygen partial pressure dependence of the defect structure of oxides along with resistivity data, the quantity $\tilde{\rho}(x)$ can be calculated. This value along with the oxide growth rate can be used to calculate the ASR as a function of time.

Alternatively, the value $\tilde{\rho}(x)$ can be determined by taking a number of ASR measurements and along with growth rate calculations, the ASR as a function of time can be experimentally determined. The experimental results are more informative with regard to the predication of an interconnects long term performance, because the results are not subject to the many assumptions that went into producing the model.

That being said, this model will be helpful in predicting what materials to study. In the case of nickel, if the ASR is estimated just using NiO growth kinetics along with bulk NiO resistivity data, the ASR is estimated as being 50% lower. Errors of this manner may make a candidate material appear better than it really is and another look worse than it really is.

In addition, the model could be used to predict how the addition of overlay coatings to an interconnect would affect the ASR of the scale. The overlay coating would affect the oxygen partial pressure in equilibrium with the external scale surface. The model could be used to predict how these changes would affect the electrical properties of the scale.

5.6 DUAL ATMOSPHERIC EXPOSURES

5.6.1 Nickel

Nickel 200 tubes were exposed in the tubular dual atmospheric apparatus shown in Figure 11a at 800°C for 400, and 600 hours. The cross-sectional images of the 600 hour exposure are shown in Figure 37. The nickel tube in Figure 37a was exposed to the SCG on the inside and the outside of the tube and NiO grows on both sides. The nickel tube in Figure 37b was exposed to the SAG on the inside and the SCG on outside of the tube. NiO grows on the outside of the tube, but no oxidation occurs on the inner wall. The growth of NiO on the tube exposed to the dual atmosphere is identical to the NiO formed on the tube exposed to air on both sides. No porosity is observed in the nickel tube. In fact, there is probably less porosity at the Ni/NiO interface for the dual atmosphere specimen then in the specimen exposed to air on both sides.

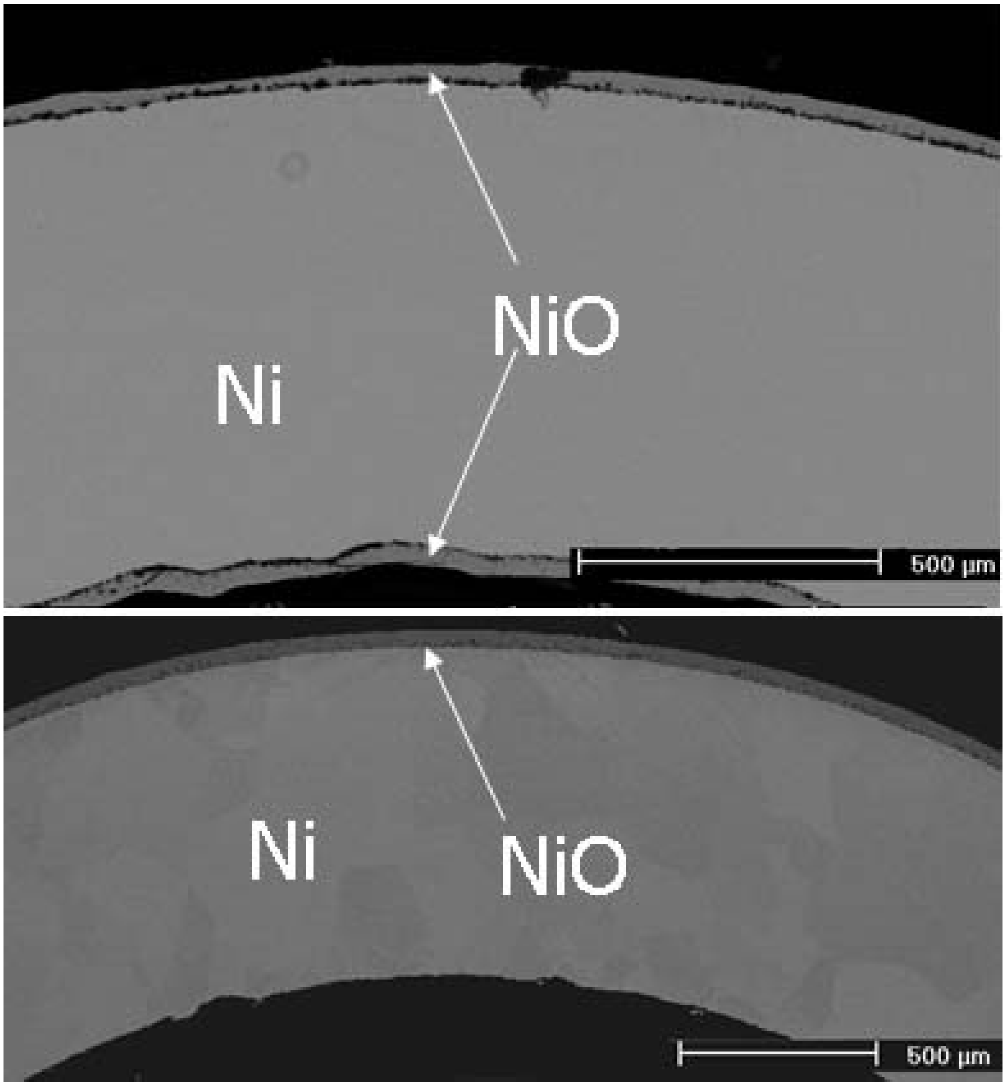

Figure 37. Nickel exposed at 800°C for 600 hours (Top) to dry air on the inside and the outside of the tube and (Bottom) exposed to dry air on the outside of the tube and Ar-4%H_2-10%H_2O on the inside.

Sievert’s law was used to calculate the oxygen and hydrogen concentration on the surfaces of the nickel tube. The oxygen pressure on the cathode side of the tube is fixed by the Ni/NiO equilibrium. The concentration profiles across the tube were calculated using the finite slab solution to Fick’s second law.[68] It is assumed that the oxygen partial pressure goes to zero at the inner tube wall and that hydrogen partial pressure goes to zero at the outer tube wall. The profiles are shown in Figure 38.

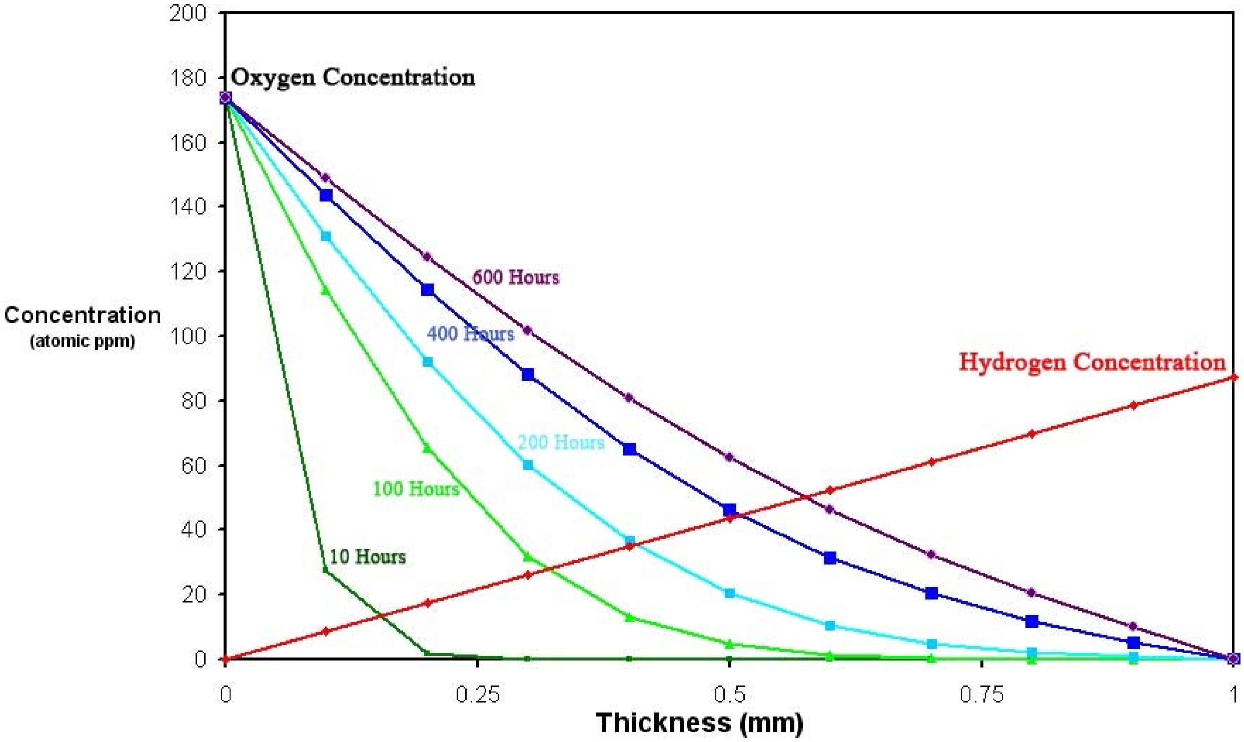

Figure 38. Calculated oxygen and hydrogen concentration profiles across a 1mm Ni sheet at 800°C

Sievert's law was then used to calculate the equivalent partial pressure of oxygen and hydrogen in equilibrium with the respective dissolved concentrations. The free energy of formation of water vapor was then used to determine the water vapor fugacity in equilibrium with the respective oxygen and hydrogen concentrations.

$$H_2 + \tfrac{1}{2} O_2 = H_2O \quad (139)$$

$$K = \frac{f_{H_2O}}{p_{H_2} p_{O_2}^{1/2}} \quad (140)$$

This data was used to determine the water vapor fugacity across the thickness of the nickel. The maximum fugacity is a little more than 1 atmosphere and therefore the approximation that the fugacity is equal to the pressure is adequate.

The assumption that the hydrogen partial pressure goes to zero at the outer tube surface is not necessarily correct. The diffusivity of hydrogen through nickel oxide is not known. The limiting case of infinitely rapid diffusion was taken above. The other limiting case is to assume that hydrogen is blocked by the oxide scale. In this case the hydrogen concentration would be constant across the tube. In this case, the water vapor fugacity is a maximum at the Ni/NiO interface with a fugacity of 7 atm. The surface free energy of nickel is 1.8J/m^2, and with this data, the critical radius for water vapor nucleation can be calculated. This value listed in Table 4 is a little greater than 5μm. This is a rather large volume of nickel which must spontaneously move; allowing nucleation and it is therefore not surprising that no cavities were observed in nickel.

If the hydrogen pressure in the anode gas was one atmosphere, then there would be more dissolved hydrogen in nickel and therefore a greater driving force for water vapor formation and cavitation. The critical radius of cavity nucleation is listed in Table 4. Again, the two limiting cases are analyzed. If hydrogen escapes at the Ni/NiO interface, the hydrogen partial pressure will be zero and this is referred to as the steady state profile in table 4. The critical radius is now 0.83μm. On the other hand, if it is assumed that hydrogen is blocked by NiO, and that the hydrogen pressure is constant, then the critical radius is 0.21 μm. This represents the maximum driving force for cavity nucleation in a non-pressurized fuel cell (P_{max}=1atm) because the maximum hydrogen activity is present at a point were the maximum oxygen activity (defined by the Ni/NiO equilibrium) occurs.

A critical radius of *r*=0.21 μm is still rather large, but at defects such as grain boundary intersections it is possible that nucleation could occur. If nucleation can occur, it is of interest to determine the rate at which such a cavity would grow. Using the analysis derived in section 2.5, equation (120) can be used to predict the growth of the cavity.

$$\frac{dV}{dt}=\frac{2\pi D_b\delta\Omega}{kT}\left(P-\frac{2\gamma}{r}\right)\frac{\left(1-X^2\right)^2}{X^2\left(1-\frac{X^2}{4}\right)-\frac{3}{4}+\ln\frac{1}{X}} \qquad (120)$$

The rate of cavity growth is plotted for different internucleation site distances in Figure 40. Figure 40 shows that the cavities will grow to a point of coalescence, at *r=L*, in less than 150 hours, even for large internucleation site distances. Figure 39 shows that it takes over 600 hours in order for the steady state diffusion profile to be established. This is the condition at which a maximum pressure is developed. Therefore the total time until void coalescence could be on the order of 700 hours.

Table 4. H_2O pressure data for nickel at 800°C

Hydrogen Profile	Hydrogen Pressure (atm)	Critical Radius (μm)	Fugacity (MPa)
Constant H_2 Conc.	0.04	5.208818631	0.691135602
Steady State Profile	1	0.833410981	4.319597512
Constant H_2 Conc.	1	0.208352745	17.27839005

Table 5. Diffusion data for nickel at 800°C

Species	Diffusivity (cm^2/s)
Nickel Grain Boundary	$1.76\text{x}10^{-7}$
Hydrogen	$6.88\text{x}10^{-5}$
Oxygen	$7.07\text{x}10^{-10}$

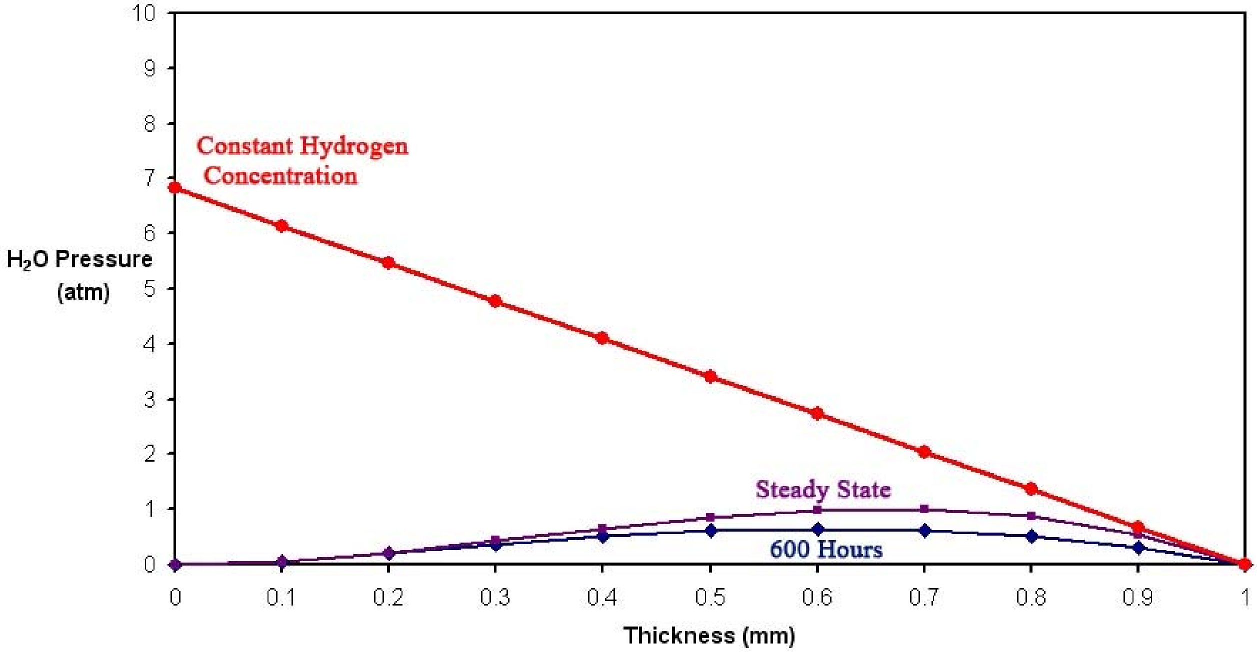

Figure 39. Calculated water vapor pressures across a 1mm nickel sheet.

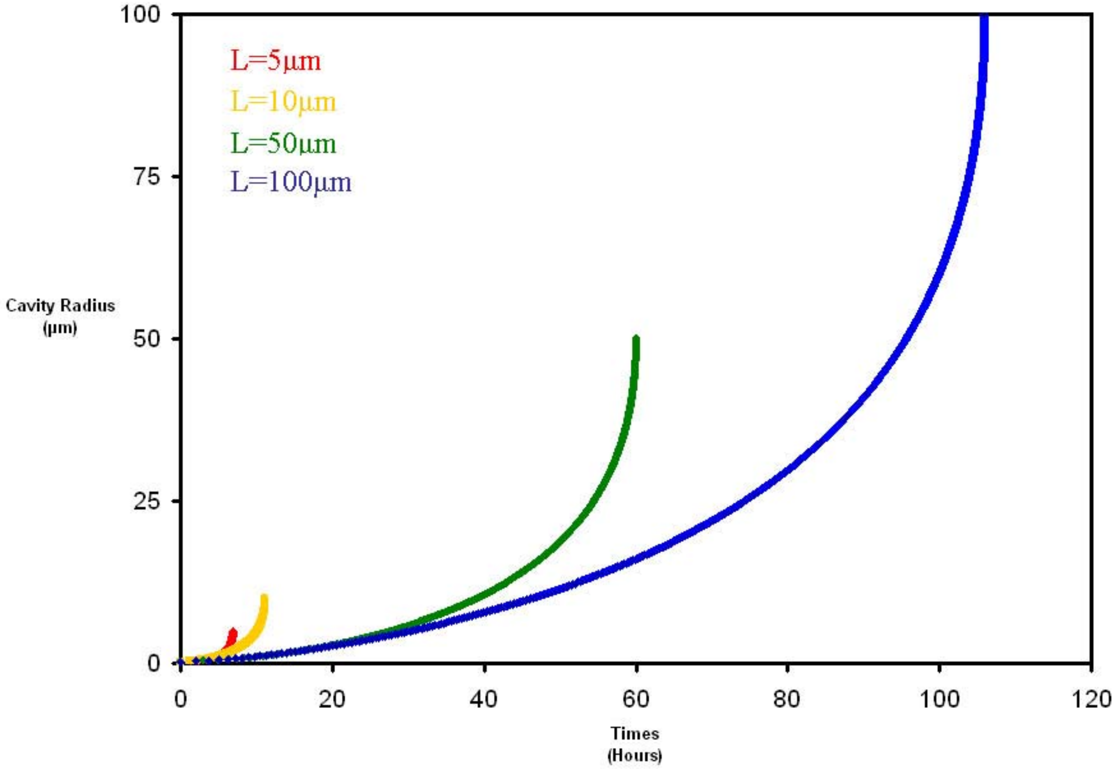

Figure 40. Predicted rate of cavity radius as a function of time in nickel at 800°C exposed to 1 atm H_2. It is assumed that the hydrogen pressure is constant throughout nickel specimen

5.6.2 Silver

Silver was first tested under single atmospheres. The purpose of these experiments was to determine if there was a significant amount of oxygen or hydrogen dissolved in the as-received silver. A sheet of silver was exposed to dry air at 800°C for 24 hours. A separate silver sheet was exposed to the simulated anode atmosphere. No microstructural changes were observed.

Dual atmospheric exposures were performed at 800°C for 1, 4, 16, and 24 hours. Porosity was observed in the cross-section after the one hour exposure and the extent of the porosity increased with the longer exposure time. These micrographs are shown in Figure 41.

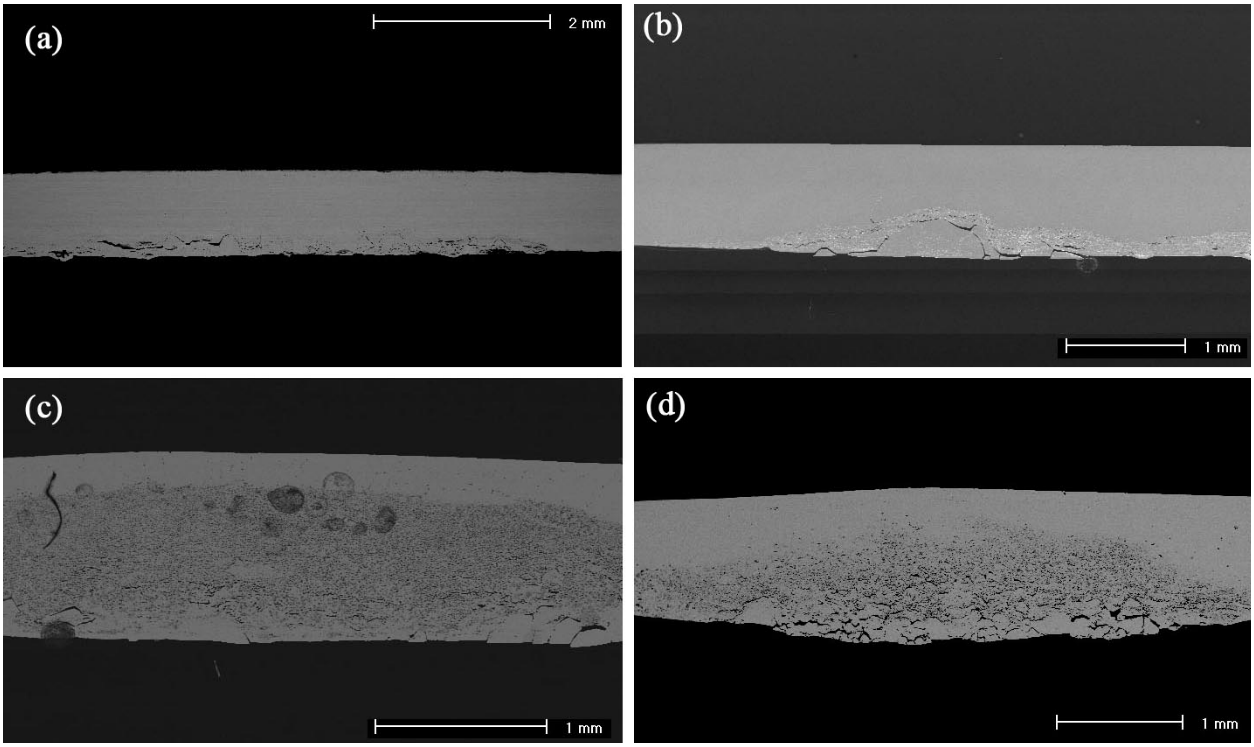

Figure 41. Silver exposed for (a)1 hours (lower magnification)(b) 4 hours (c) 16 hours and (d) 24 hours to dry air on the upper surface and Ar-4%H_2-10%H_2O at 800°C

The surface concentrations of oxygen and hydrogen were calculated using their respective Sievert's Law constants. Using diffusion coefficients, the concentration profiles of oxygen and hydrogen were calculated. Steady state was achieved in approximately 10 minutes. The water vapor fugacity in equilibrium with these concentrations was calculated and the results are shown in Figure 42. The highest water fugacity was on the order of 350 GPa.

Figure 42 shows that the maximum water vapor fugacity occurs between 0.6 and 0.7mm from the surface of the silver sheet exposed to the SCG. The highest pore density appears in this region in Figure 41d. The porosity appears to initiate near the Ag-SAG interface as seen in Figure 41a but grows the fastest near the calculated water vapor fugacity maximum. The initiation of pores at the Ag-SAG interface could also be influenced by the presence of oxygen dissolved in the silver sheet prior to exposure. The single atmosphere exposure to the SAG did not produce water vapor bubbles indicating that there is a limited amount of oxygen dissolved in the silver sheet. However, there could be enough oxygen to add in the nucleation of water vapor near the highest concentration of hydrogen. It is also possible that oxygen permeated more rapidly along grain boundaries pushing the water vapor nucleation sites toward the Ag-SAG interface.

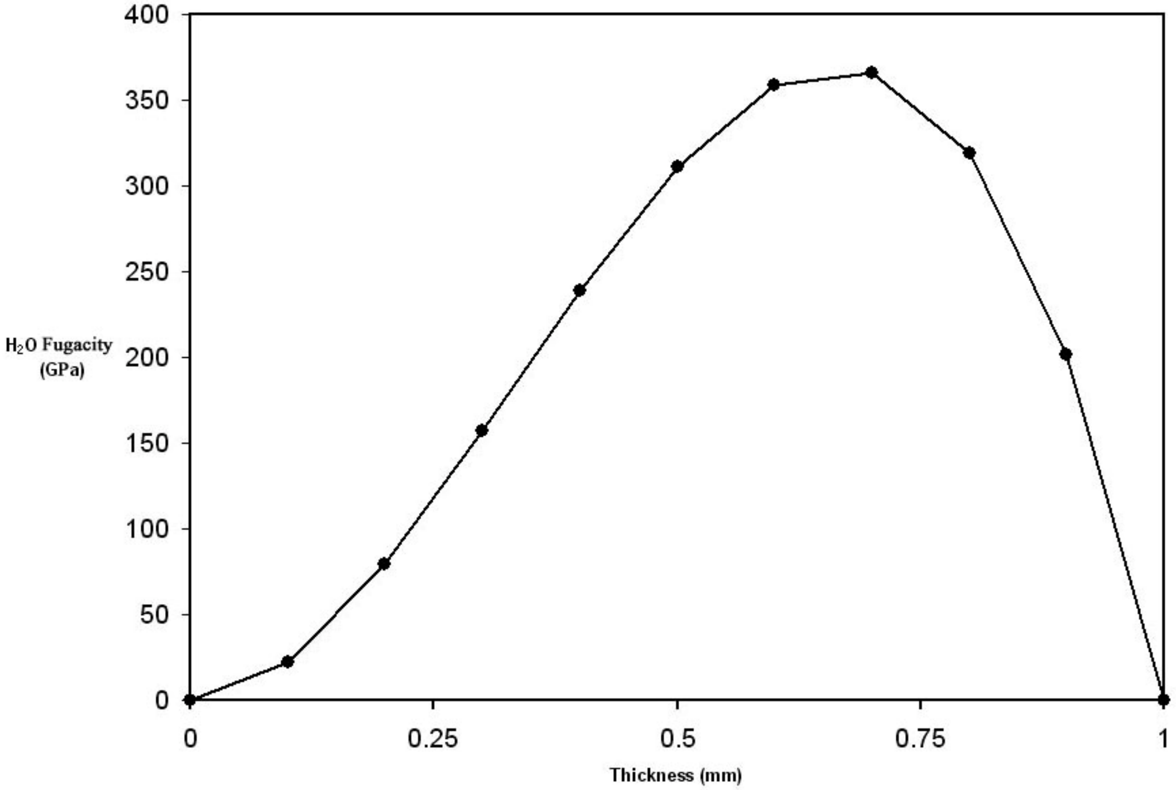

Figure 42. Calculated H_2O pressure across a 1mm Ag sheet where x=0 corresponds to the surface of the sheet exposed to the SCG and x=1 corresponds to the sheet exposed to the SAG.

Table 6. Diffusion data for silver at 800°C

Species	Diffusivity (cm^2/s)
Silver Lattice	2.04×10^{-10}
Silver Grain Boundary	2.18×10^{-6}
Hydrogen	2.93×10^{-4}
Oxygen	1.06×10^{-5}

5.6.3 Water Vapor Nucleation in Ag under Dual Atmospheric Conditions

The calculation used to determine the rate of cavity growth applied to nickel can also be applied to silver. The water vapor fugacity is high due to the high solubility of oxygen and hydrogen, and therefore the approximation of fugacity, pressure equality is not good. However, the driving force for cavity nucleation and growth is still much larger in silver than in nickel. This couples with a higher grain boundary self diffusivity of silver and as a result, the rate of cavity growth in silver is very rapid. The analysis that was performed on nickel reveals that cavity coalescence will occur is silver in less than one hour. Figure 43 shows the presence of cavities through silver and it appears the cavity coalescence has occurred along grain boundaries after one hour. The calculated cavity growth rate predicts more rapid cavity growth than was experimentally determined. However, it is clear that a pure silver interconnect could not survive in an interconnect environment for any substantial fraction of the desired 40,000 hour lifetime.

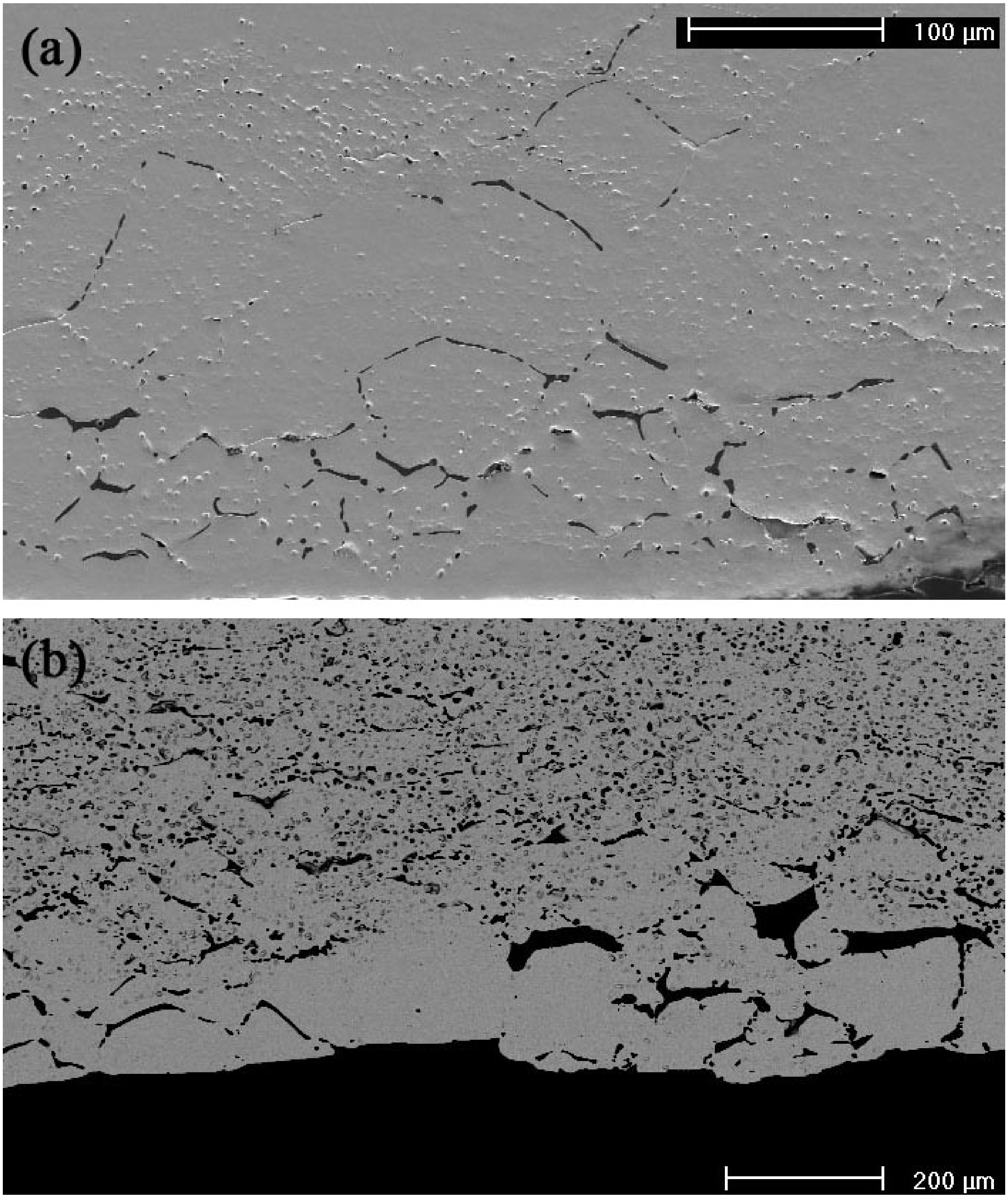

Figure 43. Cross-sectional micrographs of silver following dual atmospheric exposure for (top) 1 hour and (bottom) 24 hours.

5.6.4 Ni-Ag Systems

To avoid the mechanical pitfalls that occur in silver when it is exposed to dual atmospheric conditions, Ni-Ag systems were studied. The premise is to use a nickel matrix that contains silver pathways that will serve as electrical connections. Meulenberg et al.[8] used silver wires that passed though an alloy. However, these silver wires will be faced with the same mechanical problems as a silver sheet, and if a continuous pathway of cavities is developed though the thickness of the wire, then the anode and cathode gases will mix, greatly decreasing the efficiency of the cell.

A 1mm thick nickel sheet had holes drill of diameter 0.5mm. Silver powder was placed in the hole and heated to 975°C for 15 minutes in an atmosphere of Ar-4%H_2. This nickel-silver component was exposed to dual atmospheric conditions for 100 hours at 800°C. Cross-sectional micrographs are shown in Figures 44 and 45. In Figure 44 a large pore is located in the middle of the silver. The silver was melted in one step and it is believed that this pore formed as the result of trapped gas. In a second specimen, a small amount of silver powder was added and then melted. The process was repeated three times to fill the hole. This process was used in order to minimize the amount of gas entrapment and the cross-section is shown in Figure 45.

Figure 46 shows the cross section at higher magnification. It can be seen that oxidation occurs at the nickel-silver interface. This can be attributed to the high flux of oxygen through silver. However, conductivity measurements taken at room temperature show that good conductivity remained through the sample. This result can be attributed to an electrical short circuit path remaining at the silver nickel interface at which oxidation did not occur.

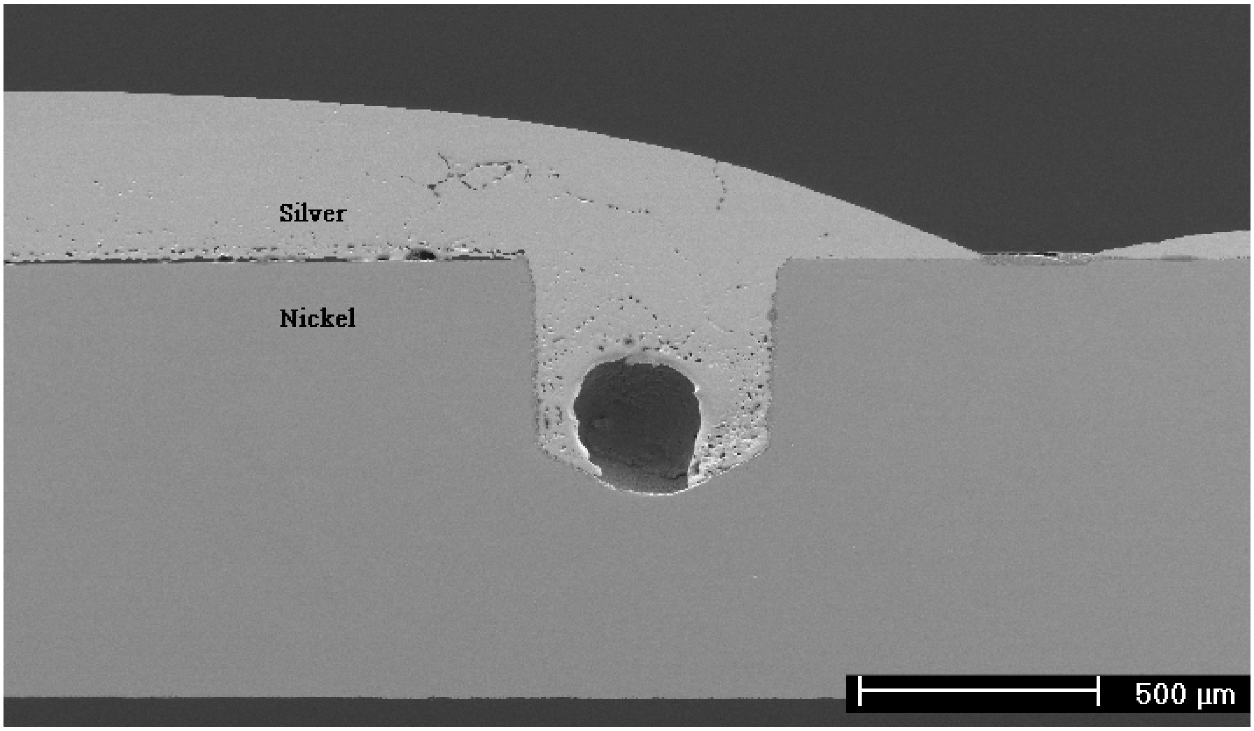

Figure 44. High conductivity Ni-Ag composite exposed to dual atmospheric conditions, SCG on the top of the figure and SAG at the bottom, for 100 hours at 800°C.

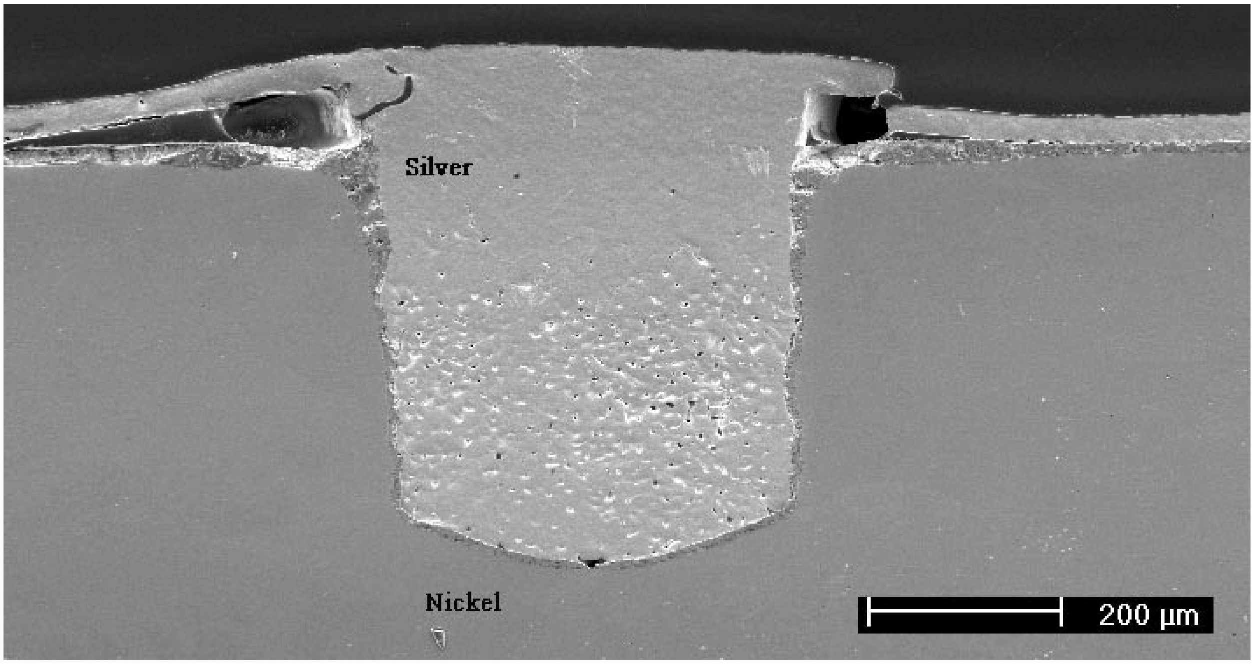

Figure 45. High conductivity Ni-Ag composite exposed to dual atmospheric conditions, SCG on the top of the figure and SAG at the bottom, for 100 hours at 800°C.

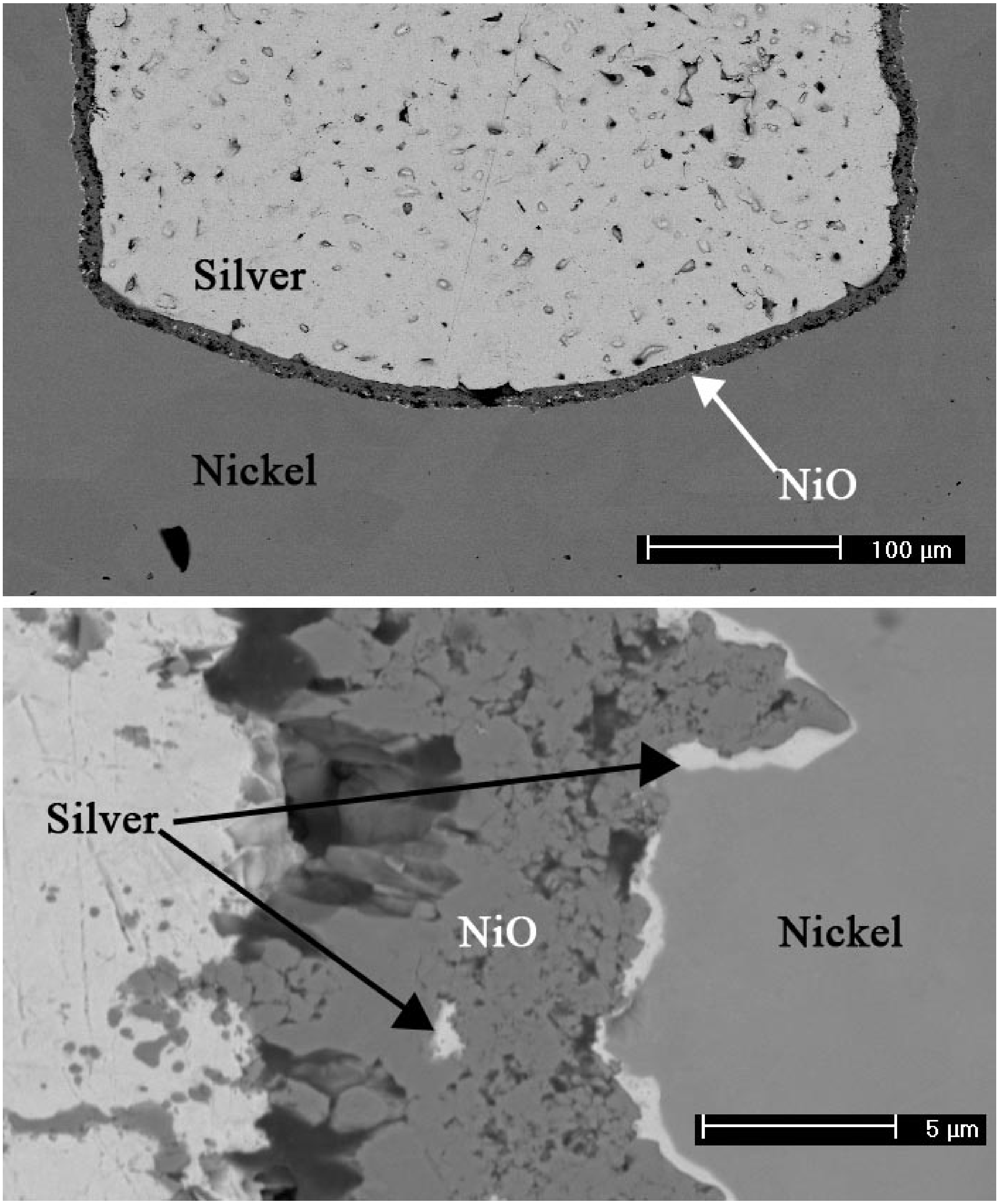

Figure 46. Ni-Ag composite exposed to dual atmospheric conditions for 100 hours at 800°C

The oxygen permeability data through silver can be used to determine under what conditions the oxidation of nickel will be limited by the transport of oxygen through silver. The flux of oxygen through silver can be expressed using Fick's first law in equation (141), where P_O ($gcm^{-1}s^{-1}$) is the permeability which is the product of the solubility and the concentration.

$$J_O = -D_O \frac{\partial c}{\partial x} = D_o \frac{C_O^{surf}}{x} = \frac{P_O}{x} \quad (141)$$

This equation describes the mass of oxygen that passes through silver per unit time.

In the presence of a sufficient amount of oxygen, the rate limiting step in the growth of NiO is diffusion through the oxide scale. Figure 47 shows the mass change of nickel that would result from diffusion in the oxide scale controlled oxidation which is described by equation (142).

$$\left(\frac{\Delta m(grams - O)}{area(cm^2)} \right)^2 = k_p'' t \quad (142)$$

The graph also shows the mass change that would result if all the oxygen permeating through the silver layer would absorb to make NiO. Initially, the flux of oxygen through the silver will limit the oxidation, and the mass will increase linearly. This linear increase will not continue indefinitely and after approximately 1500 hours, diffusion through the NiO scale will limit the oxide growth. This shows that the high conductivity silver pathway will increase the performance of the cell for a period of time, but this is substantially less than the 40,000 hour lifetime that is targeted.

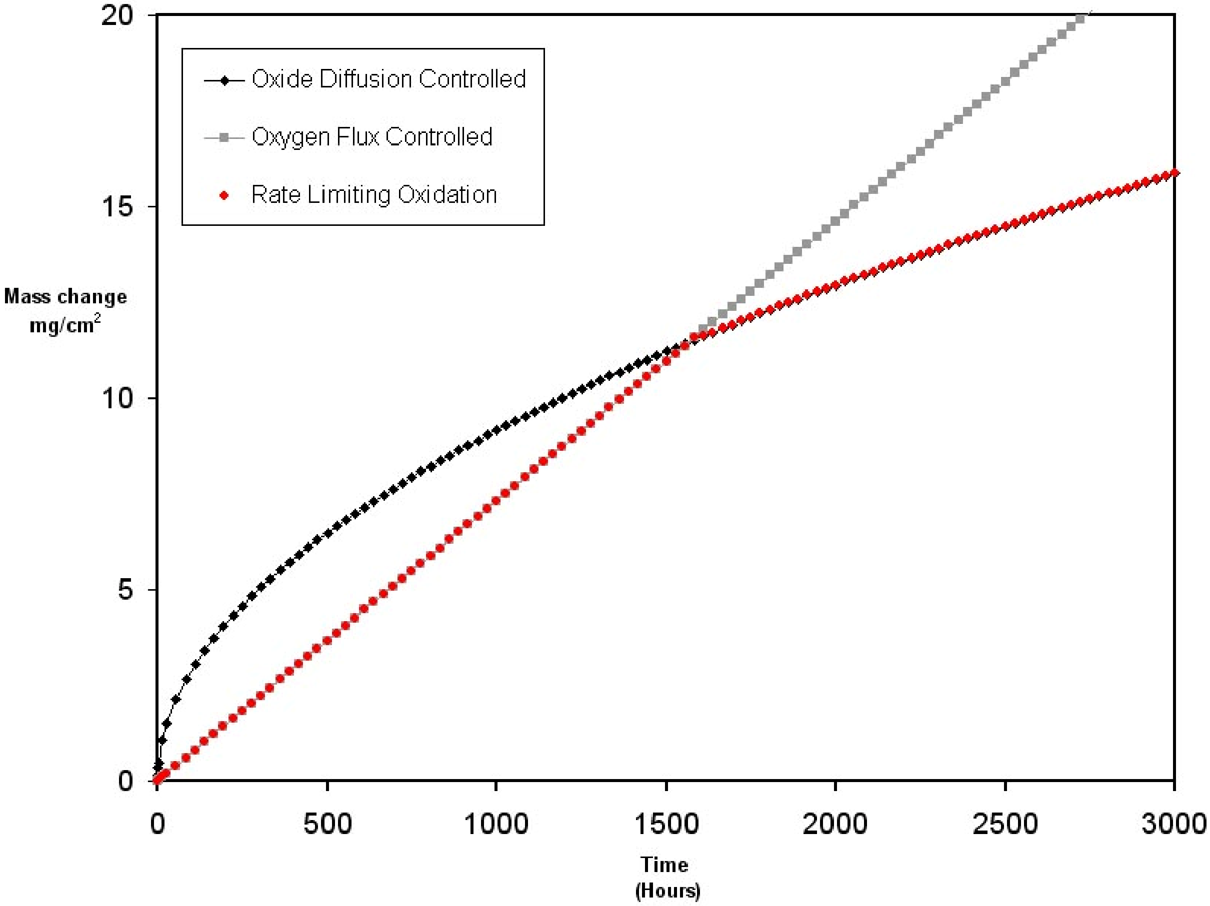

Figure 47. Calculated NiO growth at 800°C when Ni is coated by 600µm thick Ag layer.

5.7 FUEL CELL TESTS

Nickel, and two ferritic stainless steels, Ebrite, and Crofer were tested in prototype cells at NETL Morgantown and the results of these tests are given in Figure 48. The initial voltage of the cells reflects the open circuit voltage of a single cell. Platinum connects are used to collect the current from the fuel cell and the test interconnects are added to this circuit. The initial resistance is a result of the voltage loss at the platinum electrode junction in the fuel cell, and the electrical resistance of the interconnect. Once the operating temperature is reached there are several factors that will affect the total resistance. First, because the platinum connection is made using a platinum paste, the connection will improve as a result of sintering decreasing the total resistance. At the same time, the interconnect is oxidizing, which is increasing the resistance. These two competing processes cause the performance of the nickel interconnect to decrease initially due to rapid oxidation and then increase as the electrode sinters. However, in the case of the two chromia forming stainless steels, a third process is occurring. Chromium oxide species are volatizing and depositing on the cathode, degrading its performance. This process plays the greatest role in the performance of the ferritic alloys and causes the rapid degradation. This is not the case with nickel.

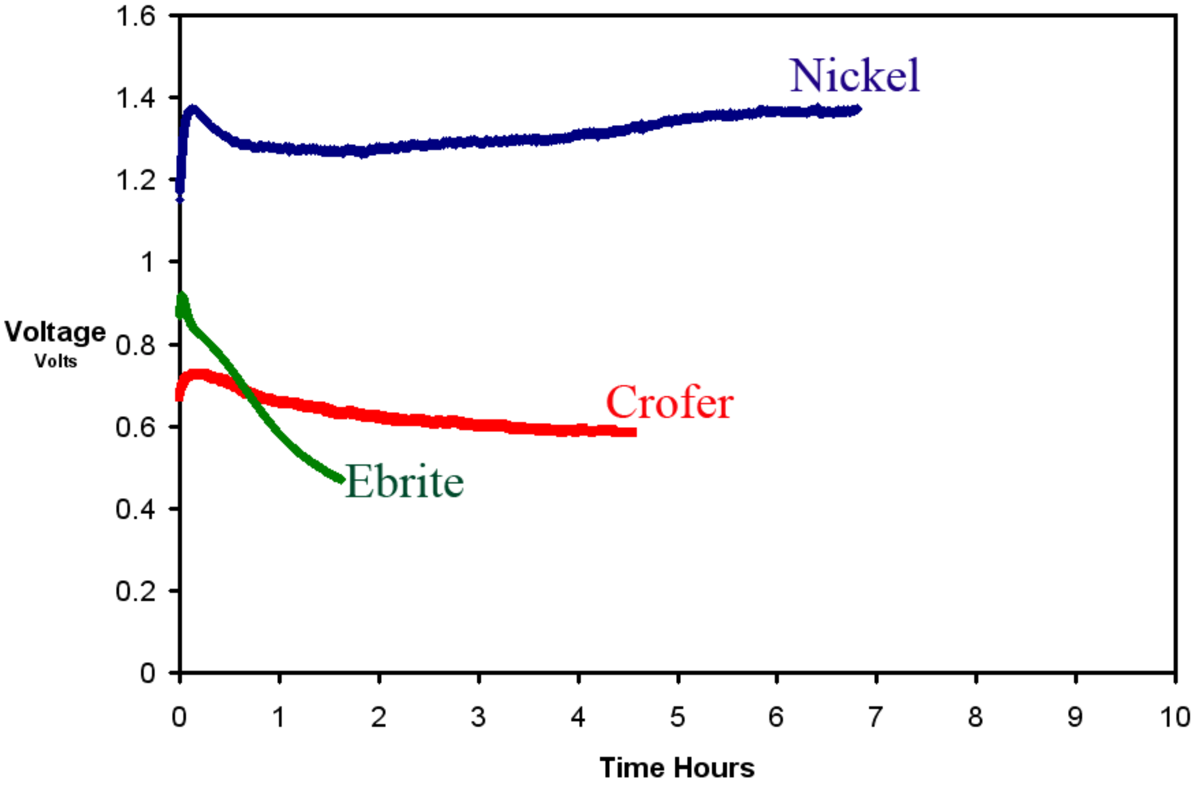

Figure 48. SOFC tests performed at 800°C with a SCG of air, and a SAG gas of H_2-3%H_2O

6.0 CONCLUSION

The goal of this study was to investigate the feasibility of nickel and nickel based systems as interconnect materials. Several materials were investigated including pure nickel, nickel-copper alloys, ceria coated nickel and Ni-5Cu, along with pure silver, and nickel-silver composites. In order to test their performance, these materials were exposed in simulated fuel cell environments for times up to 600 hours. Two aspects of the interconnect behavior were studied in depth; the electrical degradation that occurs as a result of high temperature oxidation, and the mechanical stability which can be compromised under dual atmospheric conditions due to chemically driven cavity growth.

The rate of electrical degradation was evaluated by determining the rate of oxidation using TGA, in conjunction with conductivity measurements that were performed using a direct current four-point probe. These experiments demonstrated that the increase in ASR was proportional to the increase in oxide scale thickness. The ASRs of nickel and Ni-5Cu were substantially higher than the leading candidate interconnect materials. However, when these materials were coated with CeO_2 prior to oxidation, their growth rate and ASR decreased by a factor of four and their ASR was within an order of magnitude of ferritic stainless steels exposed under similar conditions. In terms of ASR, the NiO forming interconnects are not superior to chromia forming stainless steels. However, in contrast to ferritic stainless steels, the materials tested in this study poise no risk of cell poisoning because there is no chromium in any of the alloys. In the cell tests, nickel behaved much better than Crofer and Ebrite indicating the deleterious nature of chromia bearing vapor species.

A model was developed to predict the ASR as a function of time for interconnect that required knowledge of the growth rate of the oxide on the interconnect, the bulk electrical resistivity of the oxide formed on the alloy and the defect structure of the oxide. This model showed a good agreement with the experimental results from nickel exposed at 800°C.

The mechanical stability of nickel was tested under simulated dual atmospheric conditions for 600 hours. No mechanical breakdown was observed and no cavities were detected. However, following a model previously derived to determine the rate of cavity growth in carbon steels, it was calculated that if cavities could be heterogeneously nucleated, their growth would be rapid. In light of this result, further testing of the dual atmospheric stability of nickel is recommended.

In addition to nickel and nickel alloys, silver was tested to see if a nickel-silver system could be developed that would have minimal electrical resistivity because silver does not oxidize at high temperatures. As a baseline test, pure silver was tested under simulated dual atmospheric conditions, and cavities were observed after a one hour exposure. This confirms that silver alone, cannot be used as an interconnect.

A nickel-silver composite in which silver via extended from the surface that was exposed to the cathode gas half way through an nickel interconnect. Following a 100 hour exposure under simulated dual atmospheric conditions, a good electrical connection remained. However, cross-sectional microscopy showed that a nearly continuous NiO layer had been formed at the silver-nickel interface. This result demonstrates that the long term stability of the nickel-silver composite is doubtful.

The best material studied in this investigation was nickel coated with CeO_2. This material produces an ASR that is comparable to many ferritic stainless steels; it is stable under dual atmospheric conditions and does not contain any volatile species. However, ceria coated nickel is not without draw backs. Nickel is more expensive than many other popular interconnect materials, and has a higher coefficient of thermal expansion that may limit its compatibility with certain fuel cell components. In light of these considerations $Ni+CeO_2$ should be considered for further investigation because it has the potential to be viable interconnect.

BIBLIOGRAPHY

1. Cooper, M.L., Hall, V.M.D., Annals of Science, 1982. **39**: p. 229-254.

2. Touloukian, Y.S., Kirby, R.K., Taylor, R.E., Desai, P.D, ed. *Thermal Expansion, Metallic Elements and Alloys*. Vol. Series 12. 1976, Plenum: New York.

3. Everhardt, J.L., *Engineering Properties of Nickel and Nickel Alloys*. 1971, New York: Plenum Press.

4. Weast, R.C., ed. *Handbook of Chemistry and Physics*. Vol. 66th Edition. 1965, CRC Press Inc: Boca Raton, Fl.

5. Massalski, T.B., ed. *Binary Alloy Phase Diagrams*. Vol. 1. 1986, American Society of Metals: Metals Park, OH.

6. Yang, Z., Walker, M.S., Singh, P., Stevenson, J.W., Norby, T., *Oxidation Behavior of Ferritic Stainless Steels under SOFC Interconnect Exposure Conditions.* J. Electrochem. Soc., 2004. **151**(12): p. B669-B678.

7. Singh, P.Y., Z., Viswanathan, V., Stevenson, J., Journal of Materials Engineering and Performance, 2004. **13**(3): p. 287-294.

8. Meulenberg, W.A., Teller, O., Flesch U., Buchkremer, P. Stover, D., *Improved contacting by the use of silver in solid oxide fuel cells up to an operating temperature of 800°C.* Journal of Materials Science, 2001. **36**: p. 3189-3195.

9. Birks, N., Meier, G.H., Pettit, F.S, *Introduction to the High Temperature Oxidation of Metals*. 2006, London: Oxford University Press.

10. Chiang, Y.M., Birnie, D, Kingery W.D, *Physical Ceramics*. 1997, Boston: John Wiley and Sons Inc.

11. Kroger, F.A., *The Chemistry of Imperfect Crystals*. 1964, Amsterdam: North Holland Publishing.

12. Wagner, C., *Theoretical Analysis of the Diffusion Processes Determining the Oxidation Rate of Alloys.* J. Electrochem. Soc., 1952. **99**: p. 369-380.

13. Wagner, C., Z. Phys. Chem., 1933. **21**: p. 25-41.

14. Fueki, K., Wagner, J. B. , J. Electrochem. Soc., 1965. **112**: p. 384.

15. Rapp, R.A., *High Temperature Oxidation of Metals Forming Cation-Diffusion Scales.* Metallurgical Transaction A, 1984. **15A**: p. 765-781.

16. Tretyakov, Y.D., Rapp, R.A., *Nonstoichiometries and Defect Structures in Pure Nickel Oxide and Lithium Ferrite.* Transactions of the Metallurgical Society of AIME, 1969. **245**: p. 1235-1241.

17. Osburn, C.M., Vest, R.W., J. Phys. Solids, 1971. **32**: p. 1331.

18. Farhi, R., Petot-Ervas, G., *Thermodynamic Study of Point Defects in Single Crystalline Nickel Oxide: Analysis of Experimental Results.* J. Phys. Chem. Solids, 1978. **39**: p. 1175-1179.

19. Birks, N., Rickert, H., J. Inst. Metals, 1961. **91**: p. 308.

20. Peraldi, R., Monceau, D., Pieraggi, B., *Correlations between Growth Kinetics and Microstucture for Scales Formed by High Temperature Oxidation of Pure Nickel. II Growth Kinetics.* Oxidation of Metals, 2002. **58**(3/4): p. 275-295.

21. Atkinson, A., Taylor, R.I., Goode, P.D., *Transport Process in the Oxidation of Ni Studied Using Tracers in Growing NiO Scales.* Oxidation of Metals, 1979. **13**(6): p. 519-543.

22. Atkinson, A., Taylor, R.I., *The Diffusion of Ni63 along Grain Boundaries in Nickel Oxide.* Philosophical Magazine A, 1981. **43**(4): p. 979-998.

23. Volpe, M.L., Reddy, J., *Cation Self-Diffusion and Semiconductivity of NiO.* The Journal of Chemical Physics, 1970. **53**(3): p. 1117-1125.

24. Atkinson, A., Taylor, R.I., *The diffusion of Ni in the Bulk and along Dislocations in NiO Single Crystals.* Philosophical Magazine A, 1979. **39**(5): p. 581-595.
25. Pfeil, *#459848*. 1937: U.K.

26. Whittle, D.P., Stringer, J., *Improvements in high temperature oxidation resistance by additions of reactive elements or oxide dispersions.* Phil. Trans. R. Soc. Lond., 1980. **295**: p. 309-329.

27. Strawbridge, A., Rapp, R.A, *The Role of Reactive Elements on the Scale Growth in High Temperature Oxidation of Pure Nickel, Iron, Cobalt, and Copper.* J. Electrochem. Soc., 1994. **141**(7): p. 1905-1914.

28. Atkinson, H.V., *A review of the Role of Short-Circuit Diffusion in the Oxidation of Nickel, Chromium, and Nickel-Chromium Alloys.* Oxidation of Metals, 1985. **24**(3/4): p. 177-197.

29. Ecer, G.M., Meier, G.H., *The Effect of Cerium on the Oxidation of Ni-50Cr Alloys.* Oxidation of Metals, 1979. **13**(2): p. 159-180.

30. Shewmon, *Diffusion in Solid*. 2nd ed. 1989, Warrendale, Pa: TMS.

31. Pieraggi, B., Rapp, R.A, *Chromia Scale Growth in Alloy Oxidation and the Reactive Element Effect.* J. Electrochem. Soc., 1993. **140**(10): p. 2844-2850.

32. Moosa, A.A., Rothman, S.J., *Effects of Yttrium Additions on the Oxidation of Nickel.* Oxidation of Metals, 1985. **24**(3/4): p. 133-148.

33. Pevin, J.C., Proceedings of the Ninth International Congress on Metallic Corrosion, 1984. **3**.

34. Haugsrud, R., Gunnaes, A.E., Simon, C.R., *Effect of Sol-Gel Derived Silica Coatings On High-Temperature Oxidation of Ni.* Oxidation of Metals, 2001. **56**(5/6): p. 453-465.

35. Moon, D.P., *The Reactive Element Effect on the Growth Rate of Nickel Oxide Scales at High Temperature.* Oxidation of Metals, 1989. **32**(1/2): p. 47-66.

36. Park, J.H., Altstetter, C.J., *The Diffusion and Solubility of Oxygen in Solid Nickel.* Metallurgical Transaction A, 1987. **18A**: p. 43-50.

37. Jones, F.G., Pehlke, R.D., *Solubility of Hydrogen in Solid Ni-Co and Ni-Cu Alloys.* Metallurgical Transaction A, 1971. **2**: p. 2655-2663.

38. Ramanarayanan, T.A., Rapp, R.A., *The Diffusivity and Solubility of Oxygen in Liquid Tin and Solid Silver and the Diffusivity of Oxygen in Solid Nickel.* Metallurgical Transaction A, 1972. **3**: p. 3239-3245.

39. Kittel, C.A., *Introduction to Solid State Physics 8th Edition*. 2005, Boston: John Wiley and Son.

40. Moulson, A.J., Herbert, J.M., *Electroceramics*. 1990: Chapman and Hall.

41. Tsuda, N., Nasu, K., Yanase, A., Siratori, K., *Electrical Conduction in Oxides*, Berlin: Spring-Verlag.

42. *Fuel Cell Handbook, 6th Edition*. 2002, EG&G Technical Services Inc.: Morgantown WV.

43. Shewmon, P.G., Lopez, H., Parthasarathy, T.A., *Chemically Driven Cavity Growth.* Scripta Metallurgica, 1983. **17**: p. 39-43.

44. Shewmon, P.G., *Hydrogen Attack of Carbon Steel.* Metallurgical Transaction A, 1976. **7A**: p. 279-286.

45. Vagarali, S.S., Odette, G.R., *A Model for the Growth of Hydrogen Attack Cavities in Carbon Steels.* Metallurgical Transaction A, 1981. **12A**: p. 2071-2082.

46. Harper. S., C., V.A., Townsend, D.W., Eborali, R, J. Inst. Metals, 1961-1962. **90**: p. 414-423.

47. Brickenell, R.H., Woodfard, D.A., Acta Metallurgica, 1982. **30**: p. 257-264.

48. Odette, G.R., Vararali, S.S., *An Equation-of-State for Methane for Modeling Hydrogen Attack in Ferritic Steels.* Metallurigical Transaction A, 1982. **13A**: p. 299-303.

49. Raj, R., Ashby, M.F., *Intergranular Fracture at Elevated Temperature.* Acta Metallurgica, 1975. **23**: p. 653-666.

50. Raj, R., Shih, H.M., Johnson, H.H., *Correction To:"Intergranular Fracture at Elevated Temperature".* Scripta Metallurgica, 1977. **11**: p. 839-842.

51. Park, J.H., Natesan, K., *Electronic Transport of Thermally Grown Chromia.* Oxidation of Metals, 1990. **33**(1/2): p. 31-54.

52. Laney, S.J., *Investigation of Methods for Reducing Chromia Vaporization and Growth on Ferritic Stainless Steels for Use in Solid Oxide Fuel Cell as Interconnect Materials*, in *Materials Science and Engineering*. 2006, University of Pittsburgh: Pittsburgh.

53. Haugsrud, R., *On the High Temperature Oxidation of Nickel.* Corrosion Science, 2003. **45**: p. 211-235.

54. Atkinson, A., Taylor, R.I., J. Phys. Chem. Solids, 1986. **47**.

55. Whittle, D.P., Wood, G.C., *Two-Phase Scale Formation on Cu-Ni Alloys.* Corrosion Science, 1968. **8**: p. 295-308.

56. Haugsrud, R., *High-Temperature Oxidation of Ni-20wt% Cu from 700-1100C.* Oxidation of Metals, 2001. **55**(5/6): p. 571-583.

57. Schmahl, N.G., Barthel, J., Eikerling, G., Z. Anorg. Allgem. Chem, 1964. **332**.

58. Nanni, P., Gesmundo, F., *Scaling Behavior of an Fe-4.54wt% Cu Alloy in the Range 700 to 1000 C Under 1 Atm Oxygen.* Corrosion 1980. **36**(3): p. 119-125.

59. Viani, F., Gesmundo, F., *Oxidation of Monophase Co-8.03 Wt% Cu Alloy at 700-1000 C.* Corrosion, 1981. **37**(11): p. 638-644.

60. Atkinson, A., Moon, D.P., Smart, D.W., Taylor, R.I., *Tracer Diffusion Studies in NiO Bicrystals and Polycrystal.* J. Mater. Sci., 1986. **21**: p. 1747-1757.

61. Duffy, D.M., Tasker, P.W., *Theoretical studies of diffusion processes down coicident tilt boundaries in NiO.* Phil. Mag., 1986. **A54**: p. 759-771.

62. Brady, M.P., Pint, B.A., Lu, Z.G., Zhu, J.H., Milliken, C.E., Kreidler, E.D.,Miller, L., Armstrong, T.R., Walker, L.R., *Comparision of Oxidation Behavior and Electrical Properties of Doped NiO and Chromia Forming Alloys of Solid Oxide Fuel Cell Metallic Interconnect.* Oxidation of Metals, 2006. **65**(3-4): p. 237-261.

63. Geng, S.J., Zhu, J.H., Lu, Z.G., *Evaluation of Haynes 242 alloy as SOFC interconnect material.* Solid State Ionics, 2006. **177**: p. 559-568.

64. Huang, K., Hou, P.Y., Goodenough, J.B., *Reduced Area Specific Resistance for Iron-based Metallic Interconnects by Surface Oxide Coatings.* Materials Research Bulletin, 2001. **36**: p. 81-95.

65. Huang, K., Hou, P.Y., Goodenough, J.B., *Characterization of iron-based alloy interconnects for reduced temperature solid oxide fuel cells.* Solid State Ionics, 2000. **129**: p. 237-250.

66. Pettit, F.S., *Diffusion Coefficients, Oxygen Activities, and Defect Concentrations Across a p-Type Oxide Layer on a Metal.* J. Electrochem. Soc., 1966. **113**(12): p. 1249-1254.

67. Meier, G.H., Rapp, R.A., *Electrical Conductivity and Defect Structures of Pure NiO and Chromium Doped NiO.* Zeitschrift fur Physikalische Chemie Neue Folge, 1971. **74**: p. 168-189.

68. Crank, J., *The Mathematics of Diffusion*. 1956, London: Oxford University Press.